POLITECNICO DI TORINO

Master of Science Degree in Aerospace Engineering
Academic Year 2023/2024

Master's Degree Thesis

Methodologies and tools for the analysis of the descent and re-entry phase of a reusable access to space vehicle

Supervisors:

Prof.ssa Roberta Fusaro

Prof.ssa Nicole Viola

Ing. Valeria Borio

Candidate:

Santi Dipollina

July 2024

A mio padre e a mia madre,
il propellente del mio futuro.
A mia sorella,
l'altra faccia della mia Luna.

Abstract

In recent years, the space sector has experienced significant growth, both economically and culturally. Investments in space technologies have surged with the emergence of new players and start-ups, marking the beginning of the New Space Economy. This development has led to increased demand for access to space. However, the high cost and relatively low reusability of current launch vehicles remain the main obstacles to further evolution of space exploration. The future of space exploration also depends on the development of reusable and sustainable spacecrafts. Therefore, the creation of a methodology for the design of Reusable Launch Vehicles (RLVs) is essential.

In this context, this thesis is part of a research project at the Polytechnic of Turin aimed at developing a software tool for the conceptual design of space missions involving reusable vehicles. This tool aims to support researchers and engineers during the initial design phases. The present work was conducted in parallel with two other colleagues, whose theses focus on the conceptual design of the ascent phase and the creation of a sizing methodology for a reusable SSTO vehicle with Horizontal Takeoff and Horizontal Landing (HTOL) capabilities.

This thesis investigates the conceptual study of atmospheric re-entry dynamics of a reusable Single-Stage-to-Orbit (SSTO) vehicle. The main focus is on understanding the complex interaction between aerodynamic forces, thermal loads, and stresses during re-entry.

After introducing the typical classes of re-entry vehicles and the atmospheric entry problem, an extensive study of re-entry aerodynamics was conducted. This included an analysis of the aerodynamic coefficients of the main re-entry vehicles built to date. Aerodynamic databases correlating lift and drag coefficients and lift-to-drag ratio with Mach number and angle of attack have been studied.

The dynamic of re-entry was then studied by formulating equations of motion with simplifying assumptions. In particular, the planar equations of motion were analyzed, which are sufficient at this level of detail to study the main quantities involved during re-entry. The vehicle was modeled as a point mass with aerodynamic properties and these equations were solved using the fourth-order Runge-Kutta method to obtain trends for key variables such as velocity, Mach number, dynamic pressure, and heat rate.

Subsequently, the re-entry corridor for the SSTO was developed, establishing aerothermodynamic constraints (heating rate, acceleration, dynamic pressure) that the vehicle must satisfy during descent. Furthermore, the design of the Thermal Protection System (TPS) was investigated, starting with the description of possible concepts of reusable TPSs. The vehicle wall temperature trend was then calculated to ensure adequate thermal protection during re-entry by balancing the incoming heat flux with the radiant heat flux emitted to the outside environment.

The developed methodology was applied to the case study of the Skylon SSTO, which is under development by the British company Reaction Engines Limited (REL). Skylon uses the Synergetic Air-Breathing Rocket Engine (SABRE), a promising type of engine for missions involving SSTO vehicles. Finally, a mission simulation was performed using ASTOS software to validate the results of the design methodology used in this work.

Contents

List of Tables

List of Figures

We are not here to tolerate our differences, but to accept them.
We are not here to celebrate our being identical, but to honor what distinguishes us.
We are not born in equal conditions, or with identical abilities, but we should have equal opportunities.
As individuals, we are united by our values.
Let's celebrate.

MATTHEW MCCONAUGHEY, Greenlights

Acronyms

CFD Computational Fluid Dynamics. 17, 67

ELV Expendable Launch Vehicle. 2
ESA European Space Agency. 10

FDM Finite Differences Method. 58

GUI Graphical User Interface. 10

HTOL Horizonatal Take-Off Landing. 3, 6

L/D Lift to Drag ratio. 41, 70
LEO Low Earth Orbit. 7, 13, 19

MECO Main Engine Cut-Off. 15

RCS Reaction Control System. 19, 21
RLV Reusable Launch Vehicle. 2, 3, 24
RV Re-entry Vehicle. 31
RV-NW Re-entry Vehicle Non-Winged. 4
RV-W Re-entry Vehicle Winged. 4

SABRE Synergetic Air Breathing Rocket Engine. 13
SSTO Single Stage To Orbit. 2, 3, 10

TPS Thermal Protection System. 9

Chapter 1

Introduction

In this chapter, the context in which the study of this thesis takes place will be described. Special attention is given to the reusable Single Stage To Orbit (SSTO) vehicles. The re-entry problem will also be introduced and the research context and subdivision of this thesis will be described.

1.1 Research Context

In the contemporary era, the space industry is undergoing rapid development and significant growth, driven by an increase in financial investment. The increased attractiveness and expected profitability of the industry has led to the emergence of numerous private companies and start-ups, as well as a growing venture capital market. This development has led to the emergence of the so-called New Space Economy. The OECD[1] defines it as "the full range of activities and uses of resources that create value and benefits for humanity through the exploration, understanding, management and use of space".

Today's space infrastructures are enabling the development of new services, which in turn are enabling new applications, leading to additional economic and societal benefits. This has led to the emergence of numerous players such as SpaceX, Virgin Galactic, Blue Origin who are revolutionizing the industry. The global space economy is estimated at a total value of $370 billion in 2021 and is expected to grow by 74% by 2030 to reach $642B (Fig. 1.1). Staying with the New Space Economy, the number of satellites launched in 2022 was 2057, an increase of 36% from the previous year. One of the main drivers of the New Space Economy is the market for small satellites. These being smaller, require lower launch and operating costs than traditional satellites.

At this moment, space launchers are still considered expensive and many types of launch vehicles are 'expendable' (ELV), i.e. they can only be used once. The next generation of launch vehicles must be reusable to reduce the cost of access to space and improve reliability.

The primary advantage of a Reusable Launch Vehicle (RLV) is its ability to be reused multiple times to reduces the costs associated with each launch, making space exploration and utilization more economically viable. Though the concept of RLV originated in the 1950s, low technological development at the time made this idea impractical. Later due to the advancement in the technology the existence of the Reusable launch vehicle has become more real. [12]. The term RLV is used for fully reusable vehicles that provide access to space, deployment of payloads on orbit, and controlled return to Earth [13]. In this context, the study of the re-entry phase of any body plays an essential

---

[1]Organization for Economic Co-operation and Development
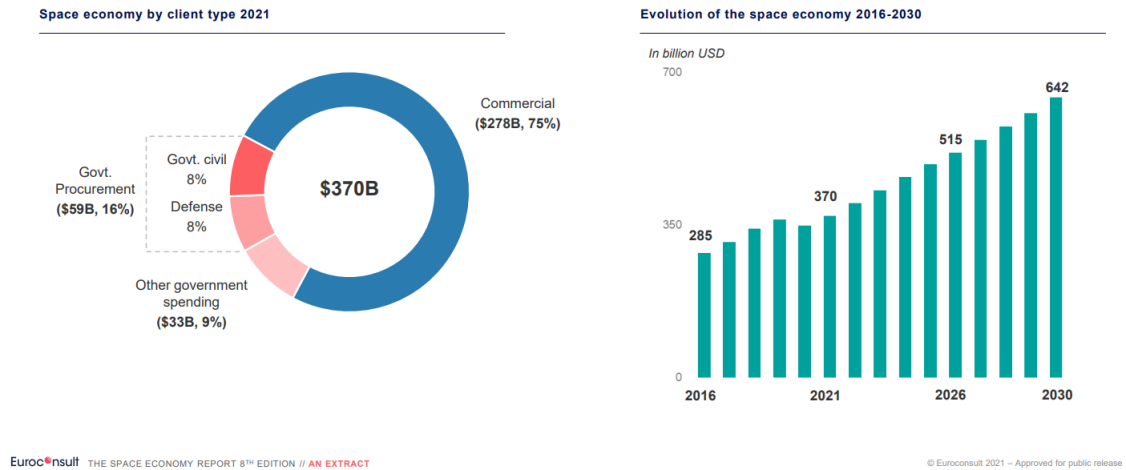
Figure 1.1: The Space Economy (source: Euroconsult, 2021)

role. If we look at the Earth's orbit, any satellite at the end of its operational life has to be disposed of in a safe manner. If it is decided to deorbit it in the atmosphere, the study of the re-entry phase is critical to ensure a safe terrestrial landing without damage to buildings or civilian infrastructure. Looking further out, the discipline of re-entry applies to all scientific missions with the goal of landing landers or rovers on the surface of other planets, such as Mars, or with the goal of taking samples of extraterrestrial material and returning them to Earth. On the other hand, for manned missions such as the Shuttle Orbiter, re-entry is much more critical because the aerothermodynamic constraints to be met are more stringent than for a capsule like, for example, the Apollo capsule.

1.2 Reusable Single Stage To Orbit vehicle

A reusable launch vehicle (RLV) is a vehicle that can be used for multiple missions. Once a mission is completed, an RLV returns to the ground and can be used again, while ELVs can only be used once. This is the main advantage of a RLV, which can be manufactured at very low cost [12]. Over the years, numerous RLV concepts have been suggested. The Space Shuttle project was launched in 1960, and during the 1990s, additional ideas were presented. However, many of these, including the X-33 and X-34 aircraft, were eventually abandoned due to excessive costs. The Space Shuttle program was also terminated for similar financial reasons and for operational accidents, in which two of the five orbiters (Columbia and Challenger) were destroyed.

When the decision was made to replace the Shuttle, there was renewed interest and excitement in developing a low-cost reusable launch vehicle. The appeal of a Single Stage To Orbit (SSTO) vehicle that could operate like a conventional winged aircraft, eliminating the need for a vertical launch complex, is evident. However, the feasibility of building and operating such a vehicle remains to be established [14]. Unlike conventional launchers, a SSTO aircraft is able to reach orbit without the need to lose any stage for weight reduction. It must be able to take off and land horizontally, like an HTOL aircraft. In addition, it must be able to perform multiple launches considering a given turnaround time. Fully reusable SSTO vehicles are part of a broader category of RLVs, characterized by the fact that all parts of the launcher can be recovered and reused.

The development of a reusable SSTO aircraft is a very complex challenge, involving various aspects and disciplines. For example, the choice of propulsion system is critical; for an SSTO aircraft, this means choosing airbreathing engines during the early stages of ascent, when the atmosphere is denser,

and then switching to rocket propulsion. Also, takeoff and landing can be either vertical or horizontal, depending on the type of propulsion system being adopted.

Finally, the study of the re-entry phase also plays a central role. The objective of this thesis is precisely the study of this phase for a reusable SSTO vehicle. A reusable Single-Stage-To-Orbit spacecraft is categorized under the "Ascent and Re-entry Vehicles" classification within the Space Access hypersonic vehicles framework [15]. The other three classes of hypersonic vehicles are:
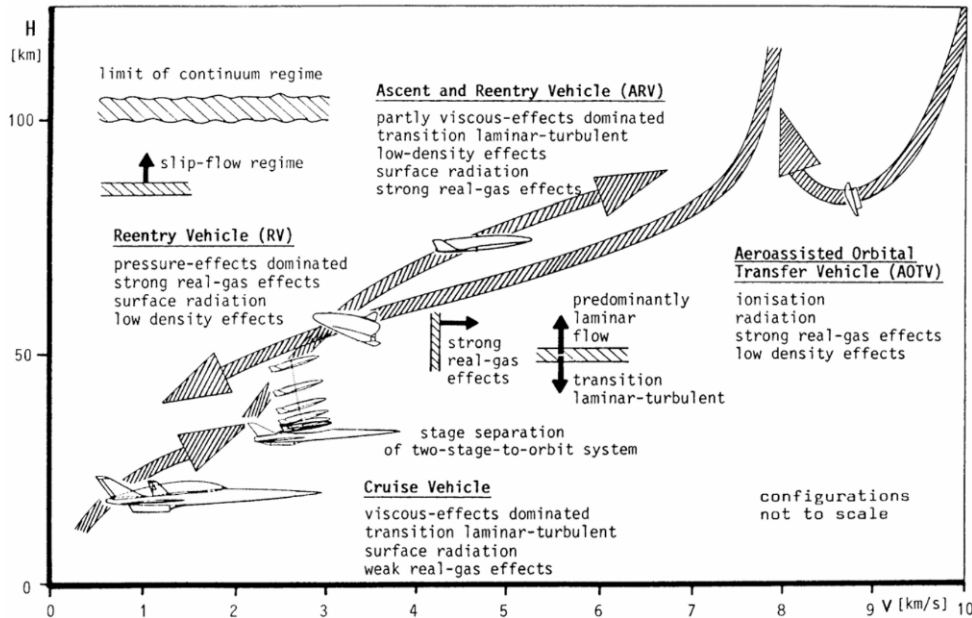
Figure 1.2: The four main classes of hypersonic aircraft

- Re-entry Vehicle (RV), divided into:
    1. Re-entry Vehicle Winged (RV-W): these vehicles re-enter Earth's atmosphere with controlled gliding maneuvers; they are designed to withstand high temperatures during re-entry while offering aircraft-like maneuverability. Its relatively high lift-to-drag ratio allows for a large cross-range capability. RV-W's are either launched vertically with the help of rockets or, in the case of TSTO systems, horizontally from a carrier vehicle, the lower stage of the system. Other launch modes have been considered, like horizontal launch. Of these vehicles, the Space Shuttle Orbiter so far was the only operational vehicle (Fig.1.3a).
    2. Re-entry Vehicle Non-Winged (RV-NW): capsules and probes (APOLLO capsule, Soyuz capsule) are the most important types of non-winged re-entry vehicles (RV-NW). They perform ballistic re-entry with limited controllability. Along their trajectory they are able to withstand a very severe thermal and dynamic field (Fig 1.3b).
- Cruise and Acceleration Vehicles (CAV): these aircraft-like vehicles operate at high altitudes and hypersonic speeds, with high aerodynamic efficiency during the cruise; they are not intended for reaching space but for point-to-point travel as an airplanes or as the first stage in a TSTO launch system. They are drag sensitive in contrast to RV-W's and RV-NW's (Fig. 1.4).
- Aeroassisted Orbital Transfer Vehicle (AOTV): these vehicles typically incorporate fixed, deployable, or inflatable heat shields for upper-atmosphere deceleration using atmospheric drag as a braking mechanism during re-entry from planetary or geosynchronous orbits.

(a) RV-W: STS Space Shuttle

(b) Apollo Command module

Figure 1.3: Re-entry vehicles

Figure 1.4: SANGER configuration with HORUS Orbiter

1.2.1   SSTO Overview

This section provides a historical background of SSTO aircrafts that have been proposed over time in concept form and those that are under development. One of the earliest reusable vehicle concepts was that of the spaceplane. They can operate like conventional aircraft, taking off and landing independently on conventional runways. One of the first spaceplane concepts was that proposed by Robert Goddard. He described a spaceplane ("stratosphere plane") with elliptically shaped wings and propelled with an airbreathing jet and a rocket engine [16]. The design of an SSTO aircraft began to be real when in 1957 the Air Force launched the Aerospaceplane program. In 1959, the program develops the Recoverable Orbital Launch System (ROLS), a SSTO design with horizontal takeoff and air-breathing engines that collect oxygen from the atmosphere during flight. However, this was eliminated due to the high costs. Below are some of the SSTO vehicles that have been proposed throughout history.

1. **NASP X30:** the National Aerospace Plane (NASP) X-30 was a United States project to create a SSTO spacecraft and passenger spaceliner. This collaborative effort between NASA, the Department of Defense, and five major contractors explored technology development for a new generation of hypersonic, single-stage atmospheric cruise or orbital spacecraft with air-breathing

primary propulsion and horizontal takeoff and landing. The X-30 would employ a multicycle engine that transitioned during the ascent from jet to ramjet and scramjet operative modes, burning liquid hydrogen fuel with oxygen captured from the atmosphere. The X-30 program was terminated for budget constraints and technical concerns in 1993 [17].

2. **Tupolev Tu-2000:** the Tupolev Tu-2000 project was initiated in 1986 by the Soviet Union as a response to the X30 aircraft by the U.S. The project consisted of 3 versions: a Mach 6 test vehicle, which was under construction at the cancellation of the program, a Mach 6 intercontinental bomber, and a SSTO launch vehicle. The SSTO aircraft was developed to have a takeoff mass of 260 tons, with a payload of about 10 tons for a 200km orbit in LEO. The propulsion system consisted of 8 turboramjets for the airbreathing phase, supported by a rocket engine to achieve the orbit. After the dissolution of the USSR, the project was cancelled in 1992 for funding reasons.

3. **Boeing/Langley SSTO:** in 1977, Boeing developed an SSTO concept, to assess the feasibility of a reusable SSTO aircraft that would use airbreathing propulsion. The design was for a 30'000 kg payload to a specific LEO orbit with a payload similar in size to the Space Shuttle, with an estimated gross take-off weight (GTOW) of 1250 tons. The propulsion system was probably based on the modified main engines of the Space Shuttle.

4. **Star Raker:** it was an SSTO HTOL aircraft proposed by Rockwell International to create a network of solar power satellites that would require frequent deliveries of heavy payloads (35,000 metric tons per year) to low earth orbit (LEO). The Star-Raker's propulsion system was a hybrid of air-breathing engines and rocket engines. It featured ten turbofan/turbo-air exchanger/Ramjet engines powered by hydrogen, for atmospheric flight, and three liquid oxygen/hydrogen rocket engines, similar to those used on the Space Shuttle, for final thrust into orbit. Despite its promising potential, the Star Raker faced significant technical challenges that ultimately prevented it from being developed beyond the concept stage.

(a) Star Raker artist's concept

(b) Boeing/Langley SSTO artist's concept

(c) Nasa X-30 artist's concept

(d) Tupolev Tu-2000 artist's concept

Figure 1.5: SSTO historical concepts vehicles

The following are the SSTO aircrafts that are currently in the research and development phase.

Avatar

AVATAR, or Avtar, stands for 'Aerobic Vehicle for Advanced Trans-Atmospheric Research'. It was first announced in May 1998 as a reusable launch vehicle with military applications. This is a concept study for a single-stage reusable spaceplane capable of horizontal takeoff and landing. AVATAR's takeoff weight is around 25 tons. For a reusable SSTO spacecraft capable of delivering a 1-ton payload to orbit, this is said to be the smallest feasible weight. The propulsion system is designed as a combination of different engines: a turbofan for initial takeoff, a ramjet for sustained hypersonic flight, a scramjet for even higher speeds, and a cryogenic rocket engine for final push into orbit. About 60% of takeoff weight is liquid hydrogen. Oxygen needed by the vehicle for combustion in space would be captured from the atmosphere during launch, reducing the need to carry oxygen during launch. Avatar is still in a conceptual design phase [16].

Radian One

The Radian One is a SSTO spaceplane operating in LEO, under development by Radian Aerospace. With a crew of two to five, Radian One will launch using an innovative rocket sled that eliminates the need for a vertical launch system. The ascent will be more similar to an airplane than to a rocket to

maintain crew safety and comfort during the flight. Radian One is able to deliver a payload of 2270 kg in low orbit and an expected return cargo capacity of 4,536 kg with a 48-hour turnaround period between flights. The Radian One's design ensures a smooth and controlled return to earth, meeting stringent thermal and acceleration requirements while decelerating [18].

Figure 1.6: Radian One spaceplane (credits: Radian Aerospace)

1.3 Re-Entry Problem

The atmospheric re-entry phase is incredibly complex for all vehicles. Throughout this phase, the aircraft encounters an aggressive dynamic environment, facing intense thermal and structural pressures, with temperatures reaching thousands of Kelvins. The re-entry phase begins when the vehicle reaches the Entry Interface Point (EIP), which is typically located at an altitude of approximately 120 km, marks the boundary at which the atmosphere becomes dense enough for aerodynamic maneuvers to be initiated.

Another parameter is the initial velocity. Higher re-entry velocity means greater maximum deceleration and the thermal loads would be unbearable for a wing aircraft intended for manned missions. Another parameter is the initial flight path angle. If it is too high, the aircraft will reach a relatively high speed and generate excessive drag, and the body will be destroyed due to the high heat flux and aerodynamic load. Moreover, a vehicle with a steeper re-entry angle will dive deeper into the atmosphere before reaching maximum deceleration [8]. If the angle is small, the drag will not be sufficient to decelerate the vehicle, which will not be able to follow a direct trajectory to the planet's surface, and it will bounce out of the atmosphere and back into space. In our discussion, however, we will assume a gliding re-entry, like the Space Shuttle. In this case, the trajectory angle is assumed to be small. This is done to have a closed-form solution.

The vehicle can reach the Earth following three different scenarios:

- **Ballistic entry**: it occurs when the lift-to-drag ratio L/D is low, typically lower then 0.5, like in the case of meteoroids, missiles or capsule, like the Apollo Command Module. These vehicles are not controllable with lift, and their re-entry trajectory is only a function of initial velocity and flight path angle and ballistic coefficient $\beta = \frac{m}{C_D S}$. The control authority is zero and the trajectory is characterized by an elevated heat flux and g-load.

- **Skip entry**: it consists of impacting the planet's atmosphere at an angle such that the entry body rebounds out of the atmosphere but is kept in a trajectory that will enable it to enter the atmosphere sometime later, with reduced entry velocity.

- **Lifting re-entry**: this type of re-entry occurs for those aircraft with values of $L/D \geq 0.5$. The lift modulation happens with a bank angle control by moving the lift vector. This way it is possible to obtain a much lower heat flux and g-load which is convenient for human re-entry. This is the case of the Space Shuttle Orbiter. A controlled re-entry also means higher accuracy on the landing position.
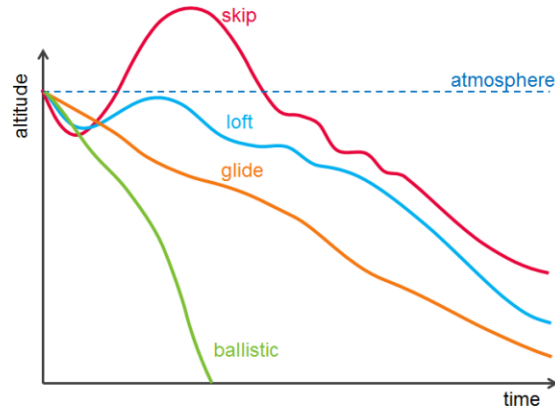
Figure 1.7: Schematic representation of trajectories for different types of re-entry [5]

When the vehicle flying lower speeds, the flowfield mainly imposes distributed pressure loads on the vehicle, affecting it through shear and normal pressure forces. Control is achieved by locally modifying this pressure field, often by adjusting configurations like flap deflections. However, during high-speed atmospheric entry, managing both the distributed loads and thermal loads from the surrounding flowfield becomes a significant engineering challenge. The technical challenge of managing thermal load is even greater than managing pressure loads[7]. For example, a satellite in a circular orbit at 320 km above the Earth's surface has a specific kinetic energy of $3.11 \cdot 10^7 \text{J/kg}$. Carbon, with one of the highest specific heats of vaporization, will vaporize at a specific energy of $6.03 \cdot 10^7$ J/kg [7]. Clearly, if all of the body's kinetic energy were to be converted into thermal energy, the object would vaporize unless made almost entirely of carbon. In reality, a significant fraction of the mechanical energy associated with entry must be dissipated by phenomena other than thermal absorption. The energy fraction absorbed by a re-entry body, as thermal energy, depends upon both the design of the vehicle and operation (trajectory).

So, reusable Thermal Protection System (TPS) is one of the main aspects to be concentrated as it is one of the most expensive systems of RLV. TPS should be lightweight, durable, operable and cost effective. Metallic TPS, super alloy honeycomb TPS concepts are used to get good results[12]. The design of the TPS is based on the evaluation of the parameters that influence the motion of the aircraft. The main variables involved in sizing a TPS are heat rate and the heat load. The former is used to chose the type of material to be used, while the latter is used to select the thickness of the TPS. In addition, dynamic pressure and acceleration cannot reach very high values either, especially if the aircraft is designed for a manned mission, where the acceleration must be between 3-4g.

These constraints are used to define the re-entry corridor, which represents the aerothermodynamic limits that the aircraft must meet to safely complete the mission. This can be represented in either an acceleration-velocity or an altitude-velocity graph. Prior to these considerations, the equations of motion must be solved to obtain the main variables involved in atmospheric re-entry. At a conceptual design stage, some assumptions can be made that simplify the problem but still provide sufficient

results for the mission feasibility study. In our case, we will consider a gliding re-entry to a non-rotating planet. The equations of planar motion are solved by the fourth-order Runge-Kutta method, and the trajectories of the main variables involved in atmospheric re-entry are obtained.

1.4 Thesis Objective: Conceptual Design of Re-entry Phase

The design of any type of aircraft goes through three stages. These stages define the maturity of the process, starting with the high-level requirements: Conceptual Design phase, Preliminary Design phase and Detailed Design phase. The work of this thesis falls under the Conceptual Design phase, where configurations are defined and supported by an initial estimate of dimensions and performance to determine which spacecraft concepts are technically feasible for the chosen mission. Decisions made at this stage of the design can determine the success or failure of the project. In parallel with this, space agencies, including European Space Agency (ESA), are particularly interested in developing new tools for new aircraft design, such as a reusable SSTO. In this sense, this thesis falls within the framework of a research project of the Polytechnic of Turin with the aim of developing a tool that can help researchers, engineers or students in the early stages of the design of reusable aircraft. This project consists of three main phases: the development of a methodology for the conceptual design of a reusable SSTO aircraft with HTOL capabilities and the characterization of the ascent and atmospheric re-entry phases. The methodology and the ascent phase have been covered in two other theses, also at Polytechnic of Turin [11][3].

Throught a GUI the user can select the aircraft configuration to be developed by defining the mission requirements, performance, propulsion system. At this point, the software is capable of sizing the vehicle using a dedicated sizing methodology. The sizing code employs an iterative process that converges the hypothetical variables to convergence values in the case of a feasible mission. In this analysis, the aircraft is treated as a unified system, given the interdependence of structural configuration, aerodynamics, and propulsion. The sizing methodology provides convergent mass and volume values for the system. The Figure 1.8 shows the organization chart of this project, i.e. how the development work of the conceptual design tool is coordinated. In particular, the work of this thesis
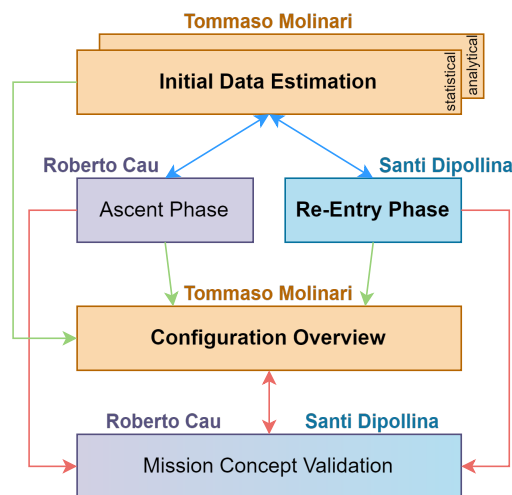
Figure 1.8: Project Organization Chart

focuses on the conceptual design of the re-entry phase of a reusable aircraft. In the re-entry phase it is very important to understand what is the trajectory that the aircraft will follow. To understand this,

the equations of motion were solved making some simplifying hypotheses. In particular, the equations of planar motion have been used considering a glide re-entry, in which the value of the flight path angle is very small, to have a solution in closed form obtained through the fourth order method of Runge Kutta. Then the re-entry corridor was obtained considering the constraints (aerodynamic, thermal) within which the aircraft must stand. Finally, the TPS was developed considering the values of heat rate and thermal load obtained through the equations of motion. These were used to evaluate the wall temperature reached by the walls during re-entry using the FDM method. All the methodology developed in this thesis work was applied to the Skylon, under study by the British company Reaction Engine. Finally, to go to validate the study of this thesis, a mission analysis was carried out on ASTOS, a software for optimization and simulation of trajectories for various missions: launchers, reentry vehicles, orbital transfers, general vehicle design, and for risk assessments from re-entry of objects.

1.5   Thesis organization

The contents of this thesis are outlined below:
- In *Chapter 2*, the case study of this thesis was described, the SKYLON spaceplane. A brief description of the configuration and a typical mission profile was made.
- In *Chapter 3*, a statistical analysis was conducted on the most important atmospheric re-entry vehicles built to date.
- In *Chapter 4*, the dynamics of atmospheric re-entry was studied. In particular, the equations of motion, later integrated in MATLAB, were reported.
- In *Chapter 5*, the atmospheric re-entry corridor was constructed. The constraints that the vehicle must meet during the descent trajectory were described. Specifically, the re-entry corridor was constructed in the Deceleration-Velocity map and the Altitude-Velocity map.
- In *Chapter 6*, an analysis was performed to design the Thermal Protection System. The wall temperature was obtained by performing a heat balance between the radiated and absorbed flux. In addition, different types of reusable TPSs found in the literature were described.
- In *Chapter 7* a mission analysis was conducted using the commercial software ASTOS aimed to verify the developed conceptual design methodology presented. In this context, the re-entry phase of the sized SKYLON was simulated.
- Finally, In *Chapter 8* conclusions, limitations and possible future works are analyzed.

Chapter 2

Case Study: Skylon

The case study vehicle of this thesis, SKYLON, developed by the British company Reaction Engines, is described in this section. SKYLON represents a fully reusable SSTO launch system that functions like an aircraft, taking off and landing on a convetional runway after completing its orbital missions [1]. This innovative approach not only significantly reduces costs, but also increases reliability, availability and overall capability for space access customers. It has as its primary purpose to achieve the lowest cost access to space possible with both current technology and commercial feasibility.

To increase the achievable mass ratio for an SSTO, SKYLON exploits the Synergetic Air Breathing Rocket Engine (SABRE) engine technology, based on a combined-cycle LOX/LH_2 engine able to cover the entire mission of the vehicle by working both in airbreathing mode and rocket mode. The SABRE engine employs a unique approach by pre-cooling air before compressing it to a high enough pressure for utilization as the oxidizer in a high-performance rocket engine. Furthermore, the heat extracted from the pre-cooled air is utilized to power the compressor and fuel delivery pumps. As a result of this technology, SSTO vehicles utilizing the SABRE propulsion system can achieve an impressive mass ratio of approximately 23%, almost double that of a pure rocket system. During launch, the engine operates in air-breathing mode until the vehicle reaches Mach 5.14 at an altitude of 28.5 km [1]. At this point, the engine will switch to a pure rocket mode for the remainder of the ascent to Low Earth Orbit (LEO). Once ascent and orbital insertion are achieved, the payload is deployed and orbital operations begin. Once the orbital operations are completed, the vehicle begins its return to Earth.

Re-entry into the atmosphere takes place at an altitude of 120 km, where the vehicle performs maneuvers to adjust temperatures and aerothermodynamic loads to ensure compliance with predetermined re-entry criteria. The vehicle will use a glide approach similar to that of the Space Shuttle. The vehicle will then reach the landing runway.

As it can be seen in Figure 2.1, the airframe consists of a slender fuselage containing the propellant tanks and the payload bay. The payload bay of this vehicle is positioned at the wing attachment point. The axial symmetric nacelles, on which the SABRE engines are mounted, are positioned on the wingtips. Unlike other SSTO designs, SKYLON has a unique separation between its thin fuselage and its delta wing, which is positioned about halfway up the fuselage. This configuration has proven to be optimal for weight, lift and volume but poses challenges in the management of heat flows, as it gives rise to localized high heat fluxes that necessitate an active cooling system [1].

The dimensional and mass characteristics of the SKYLON are reported in table 2.1. Most of the fuselage is designed for cryogenic hydrogen tanks, with a smaller portion reserved for liquid oxygen

tanks. This arrangement is feasible because the oxidizer comes from the outside air during the initial ascent phase and the low density of hydrogen requires larger tanks. The placement of these tanks presents balance issues that affect the stability of the vehicle. These challenges have been overcome by a careful aerodynamic design and by a differentiated combustion of the fuel in the two tanks.

SKYLON reference values	
Fuselage length	83.1 m
Wing Span	26.8 m
Heigth	13.5 m
Max Payload Weight	15 tons
Dry Weight	53.4 tons
Gross Weight	325.0 tons

Table 2.1: Dimensional and weight characteristics of the SKYLON spaceplane [1]

The SKYLON is equipped with control surfaces for atmospheric flight, including canard foreplanes for pitch control, ailerons for roll control, and an aft fin for yaw control. During the pure rocket phase, control is achieved through differential engine thrust. In addition to the main propulsion system tanks, there are a set of secondary cryogenic tanks which feed the orbital manoeuvring engines, the reaction control thrusters and the fuel cell power supply. Indeed, it features a SOMA (SKYLON Orbital Maneuvering Assembly) module with engines designed for orbital maneuvers.
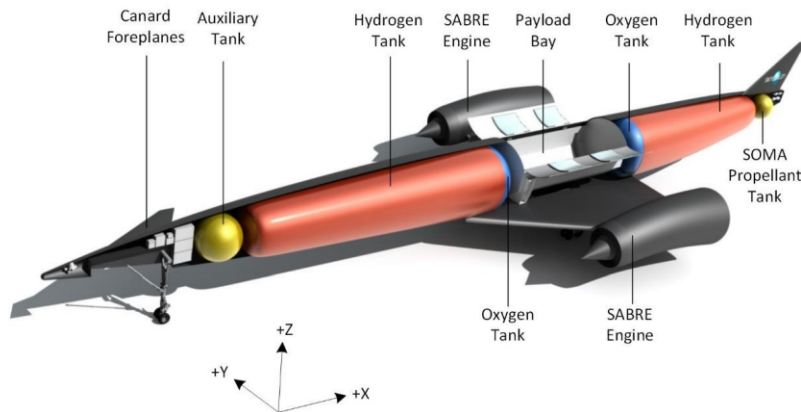
Figure 2.1: Skylon layout

2.1   Typical Mission Profile

SKYLON is designed to operate like an aircraft. Payloads would be integrated into the payload bay from the top through payload bay doors. This process is very similar to the NASA's Space Shuttle Orbiter. Once the payload is installed, the vehicle is towed to a refueling ramp located at the end of the runway. The hydrogen, oxygen and helium propellants are then loaded and the vehicle is moved to the start of the runway. Once all pre-flight checks have been completed, the vehicle starts its engines to verify full thrust and ensure nominal operation. After receiving the launch command from Mission Control, the vehicle releases the brakes and accelerates down the runway. Upon reaching 155m/s launch speed, the vehicle rotates and commits to flight. If a malfunction occurs during takeoff, the vehicle will shut down all remaining propulsion systems and brake to a stop on the runway. If a malfunction occurs after the decision point that forces the vehicle to take off, it will dump fuel during

powered flight and then return to the runway for a glide landing.

The vehicle follows a climbing, lifting and accelerating trajectory with its engines in air-breathing mode until it reaches a speed slightly above Mach 5 and an altitude of 28 km. At this point the engines transition to pure rocket mode, allowing the vehicle to continue climbing and accelerating to orbital velocity. As powered flight concludes, the engines throttle back to ensure the axial acceleration is limited to 3g. After MECO, the vehicle performs a small ullage burn using the SOMA orbital maneuvering engines and dumps all residual propellants from its main tanks. At MECO, SKYLON is in a transfer orbit with an apogee equal to the altitude of the required circular orbit. After reaching the apogee, the SOMA engines fire again to circularize the orbit [1].

Orbital operations would begin with the opening of the payload bay doors. For missions involving delivery to LEO, the orbital phase of the mission would be completed with payload deployment. After orbital operations have been completed the vehicle would close its payload bay doors and prepare for re-entry. At a pre-calculated time, the vehicle performs a retro-burn with its SOMA engines and begins its descent. It passes the re-entry interface at an altitude of 120 km, maneuvering through banking and adjusting its angle of attack to control temperatures and heat loads, as well as to meet the pre-calculated downrange and cross-range requirements necessary for the return to the spaceport. The vehicle would finally enter a gliding approach and landing schedule that would be almost identical to that of the Space Shuttle. All flight hardware would then be inspected, serviced and prepared for the subsequent flight. A typical descent trajectory is shown in Figure 2.2.
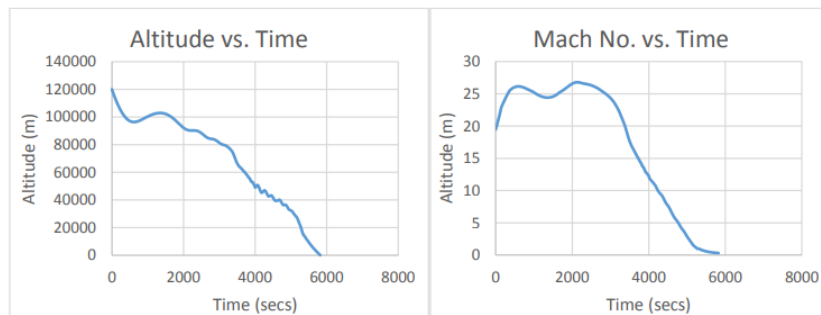
Figure 2.2: A Typical Descent Trajectory[1]

Chapter 3

Aerodynamic Background

A typical re-entry vehicle, both ballistic and lifting body, experiences a very aggressive and yet not fully known environment, called hypersonic regime. The hypersonic regime occurs when the flow velocities have very high values compared to those of the supersonic regime. There is a conventional rule that defines hypersonic aerodynamics as that flow where the Mach number is greater than 5. However, hypersonic flow is best defined as that regime where certain physical flow phenomena become progressively more important as the Mach number is increased to higher values. In some cases, one or more of these phenomena may become important above Mach 3, whereas in other cases they may not be compelling until Mach 7 or higher [6]. Various types of phenomena that can be established are, for example, strong bow shocks, thin shock layer and high-temperature effects and aerodynamic heating become more important. Moreover, engine–airframe integration may be critical. The aim of aerodynamics, in general, is the creation of aerodynamic models that report variations in aerodynamic coefficients as a function of independent variables. There are a lot of independent variables which influence the aerodynamic coefficients [6]. In the following we specify the most important ones:

$$C_i = f(M, Re, \alpha, \dot{\alpha}, \beta, \delta_e, \delta_a, \delta_{bf}, \delta_r, p, q, r)$$

where:

M: flight Mach number

Re: Reynolds number,

α: angle of attack

$\dot{\alpha}$: time derivative of α,

β: angle of side slip, yaw angle,

δ_e: elevon deflection

δ_a: aileron setting,

δ_{bf}: body flap deflection

δ_r: rudder deflection,

q, p, r: angular velocities.

Of course, not all of the independent variables are appropriate or important for the various space vehicles. For example, CAV's do not have body flaps or RV-NW's have no aerodynamic controls[6]. The creation of the aerodynamic data base, which is largely driven by wind tunnel tests and numerical simulations, takes place with fixed aerodynamic control surfaces and a constant flight Mach number, while changing either the angle of attack α (with constant β) or the angle of side slip β (with constant α). There are several methods to follow for creating an aerodynamic database. During the early design phase (e.g., phase-A design), low-order methods are typically suitable being able to improve computational speed even if at the expense of fidelity. For example, panel methods can be used in conjunction with Newtonian flow theory to obtain the hypersonic aerodynamic characteristics of a vehicle with orders of magnitude reduction in computational requirement compared to Computational

Fluid Dynamics (CFD) [6]. In Newtonian flow, Newton considered the flow as a uniform rectilinear stream of particles. Newton assumed that upon striking a surface inclined at an angle θ to the stream, the particles would transfer their normal momentum to the surface (thus exerting a force on it), but their tangential momentum would be preserved. Hence, the particles would move along the surface after colliding with it [19] (Fig 3.1) . From this mind, through appropriate consideration and simplex
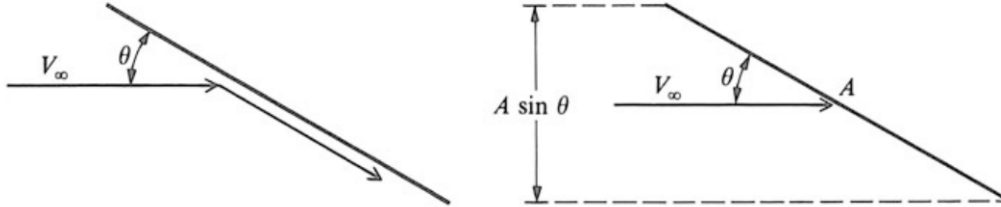
Figure 3.1: Newton impact theory [6]

analytical calculations, he obtained the so-called Newtonian sine-squared law for pressure coefficient:

$$C_p = 2sin^2\theta \tag{3.1}$$

where '2' represents the pressure coefficient at the stagnation point. It allows us to calculate the pressure coefficient at a point on a surface where the angle between a tangent to the surface at that point and the free-stream direction is θ. In estimates of hypersonic pressure distributions, it is best to replace the pure number 2 in Eq.3.1 with the value of the maximum pressure coefficient $C_{p,max}$, which occurs at the stagnation point. This leads to the modified Newtonian law [19]:

$$C_p = C_{p,max}sin^2\theta \tag{3.2}$$

where

$$C_{p,max} = \frac{p_{0,2} - p_\infty}{\frac{1}{2}\rho_\infty V_\infty^2} \tag{3.3}$$

where $p_{0,2}$ is the total pressure behind a normal shock wave. Because excellent agreement is obtained with the exact results, the Newtonian sine-squared law is useful for hypersonic applications [19]. Knowing the distribution of pressure along the body we can calculate lift and drag coefficients at an angle of attack α. Further, the importance of Newtonian flow theory can be appreciated also considering that the geometry (and/or a part of it) of many common hypersonic vehicles of practical interest such as sphere–cone, blunt biconic, and spherical forebody segments can be also expressed analytically , thus providing vehicle aerodynamic performance in a closed form approach [6]. Moreover, Newtonian theory is a local surface inclination method where C_p depends only on the local surface deflection angle; it does not depend on any aspect of the surrounding flowfield [6].

3.1 Statistical Analysis

The purpose of this thesis is not to compute the aerodynamic database of a re-entry vehicle, but to study the feasibility of an atmospheric re-entry mission for a reusable SSTO vehicle. Please note that this work is part of a project that aims to create a tool in which any user, entering the data of his aircraft, can calculate the main quantities during the re-entry phase. Therefore, it was decided to conduct a statistical analysis of the main reference aircraft for the re-entry phase in order to better understand the trends of the coefficients in function, in this case, of the Mach number M and the angle of attack α.

3.1.1   Space Shuttle Orbiter

The Space Shuttle represents a semi-reusable system for the transportation of payloads and humans into various LEOs. The missions of the Space Shuttle involved carrying large and heavy payloads to various low Earth orbits including elements of the International Space Station (ISS), performing service missions, also to satellites, e.g., upgrading the Hubble Space Telescope, and serving as crew transport system for the ISS [2]. During the ascent the boosters are separated at a height of 50km after 120s. These are recovered in the Atlantic Ocean, refurbished and refilled with solid propellant. The expandable tank is separated at a height of 120 km. The descent phase begins with de-orbiting through the orbital maneuvering system. Afterwards, the re-entry in Earth's atmosphere and finally landing horizontally on the runway. The entire process is executed without the engines on.

When back on Earth's surface the Orbiter is reused after inspection and refurbishment. This space transportation concept was the only operational winged and manned system to reach the orbit and to land horizontally. The fleet has performed 135 flights. The first launch took place on April 12, 1981, followed by the first re-entry flight on April 14, 1981 [2]. Six Orbiter vehicles were built:

- Enterprise (1977)
- Columbia (1981)
- Challenger (1983)
- Discovery (1984)
- Atlantis (1985)
- Endeavour (1992)

Due to the high costs and accidents during its operational life, the Space Shuttle program was shut down in July 2011. The Space Shuttle Orbiter is the largest space transportation vehicle ever
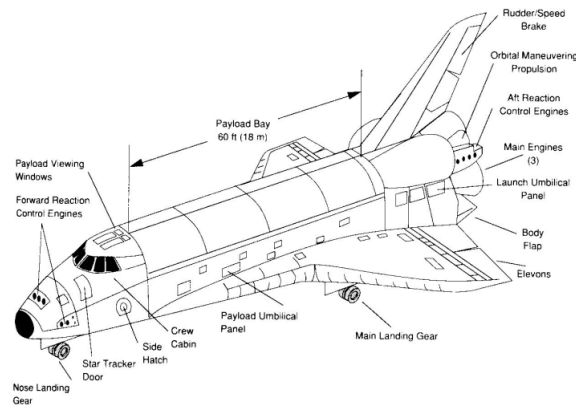
Figure 3.2: SPACE SHUTTLE Orbiter: Design and equipment details [2]

built, with a total length of 37.238 m and a span of 23.842 m. The nominal x-coordinate of the center-of-gravity is located at 21.303 m measured from the nose. The Orbiter has a double delta wing with sweep angles of 45° and 81°. The three main engines are the most powerful rockets ever designed, each with a vacuum thrust of 2100 kN (214 tons) and a specific impulse of 455.2 s. The rockets of the Orbital Maneuvering System (OMS) are contained in the pods on the aft fuselage of the Orbiter and generate a thrust of 27 kN. Further, a Reaction Control System (RCS) is installed, which consists of thrusters of the 500 N class [2]. The aerodynamic coefficients, which we present below, were mainly obtained from wind tunnel tests. The following figures show the trends of aerodynamic coefficients as a function of angle of attack at different Mach numbers for the longitudinal motion.

SPACE SHUTTLE Orbiter reference values	
Total Length	37.238 m
Total Width	23.842 m
Reference Length	32.744 m
Reference Area	249.909 m^2
Empty mass	78000 kg
Gross mass at launch	110000 kg
Reference chord length (M.A.C)	12.060 m

Table 3.1: SPACE SHUTTLE Orbiter reference values [2]
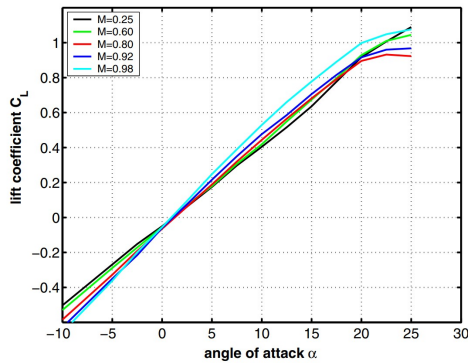
(a) Lift Coefficient C_L - subsonic regime
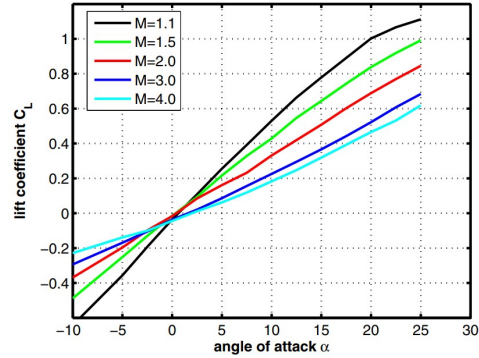
(b) Lift Coefficient C_L - transonic regime
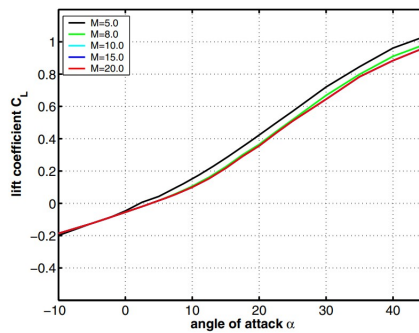
(c) Lift Coefficient C_L - hypersonic regime

Figure 3.3: Lift coefficient C_L as a function of angle of attack for subsonic to hypersonic Mach numbers, Space Shuttle Orbiter [2]

3.1.2 Hermes

Hermes was a proposed spaceplane designed by the French Centre National d'Études Spatiales (CNES) in 1975, and later by the European Space Agency (ESA) in order to guarantee Europe an autonomous and manned access to space. The system was composed by the RV-W space plane HERMES, intended for a gliding re-entry from space to an Earth landing site, and the launch system ARIANE V. HERMES was conceived to have the following features [2]:

- ascent to LEO (up to 800km) on top of the Ariane V rocket.
- 30-90 days mission duration in orbit.
- total launch mass 21000 kg.
- fully reusability.

In 1993 the HERMES project was cancelled due to the new political environment and budget constraints [2]. The HERMES shape 1.0 has a delta wing with a sweep angle of 74°. The total length of the

(a) Drag Coefficient C_D - subsonic regime   (b) Drag Coefficient C_D - transonic regime

(c) Drag Coefficient C_D - hypersonic regime
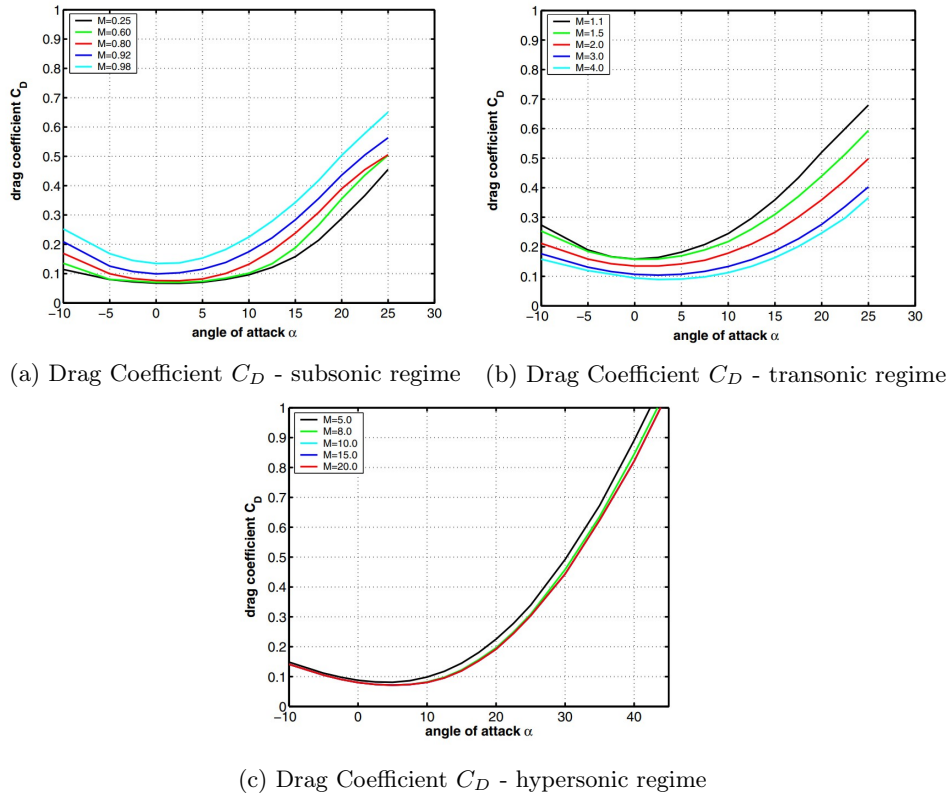
Figure 3.4: Drag coefficient C_D as a function of angle of attack for subsonic to hypersonic Mach numbers, Space Shuttle Orbiter [2]

vehicle was 14.574 m and the total width 9.379 m. Other dimensions and quantities are given in Tab.3.2. The design philosophy of the HERMES configuration differed significantly from that of the

Hermes reference values	
Total Length	14.574 m
Total Width	9.379 m
Reference Length	15500 m
Reference Area	84.67 m^2
Empty mass	15000 kg
Gross mass at launch	21000 kg

Table 3.2: Hermes shape 1.0: dimensions, quantities and reference values [2]

SPACE SHUTTLE Orbiter. It achieved lateral stability through the use of winglets, with control maintained by rudders located at the trailing edge of these winglets. The SPACE SHUTTLE Orbiter uses for this function a central fin. The advantage of the winglet design lies in its ability to become aerodynamically effective earlier during re-entry, at approximately 70 km altitude, compared to the central fin solution, which becomes effective at around 30 km altitude. The consequence for the SPACE SHUTTLE Orbiter is, that the lateral stability has to be controlled by a RCS [2]. The lift coefficient C_L shows a nearly linear behavior over the whole angle of attack range. The drag coefficient C_D around $\alpha \approx 0$ is small for all Mach numbers, rising with increasing angle of attack. The maximum lift-to-drag ratio $L/D_{max} \approx 5$ occurs at $\alpha \approx 10$ in the subsonic flight regime and reduces for the low supersonic Mach numbers [2].
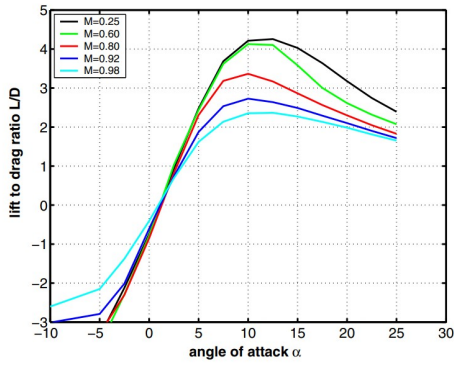
(a) Lift to Drag ratio - subsonic regime
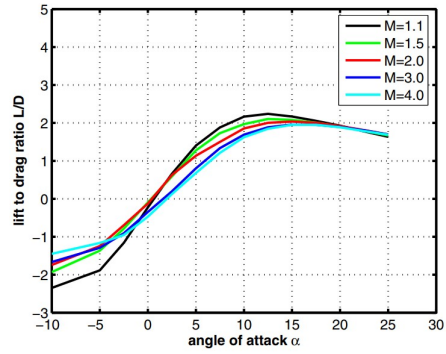
(b) Lift to Drag ratio - transonic regime
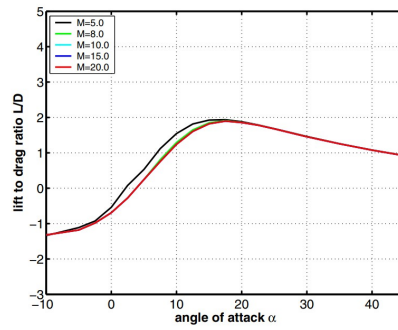
(c) Lift to Drag ratio - hypersonic regime

Figure 3.5: Lift to Drag ratio as a function of angle of attack for subsonic to hypersonic Mach numbers, Space Shuttle Orbiter [2]


Figure 3.6: Hermes spaceplane [2]
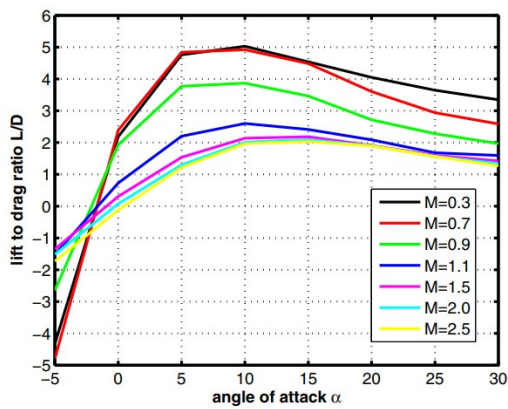
(a) Subsonic regime
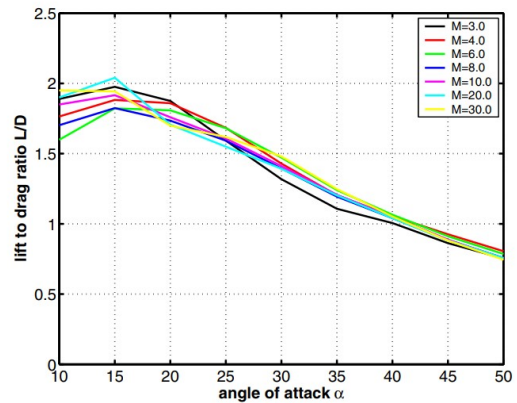
(b) Supersonic to hypersonic regime

Figure 3.9: Lift to Drag ratio L/D as a function of the angle of attack α for subsonic up to hypersonic Mach numbers, Hermes [2]

(a) Subsonic regime

(b) Supersonic to hypersonic regime
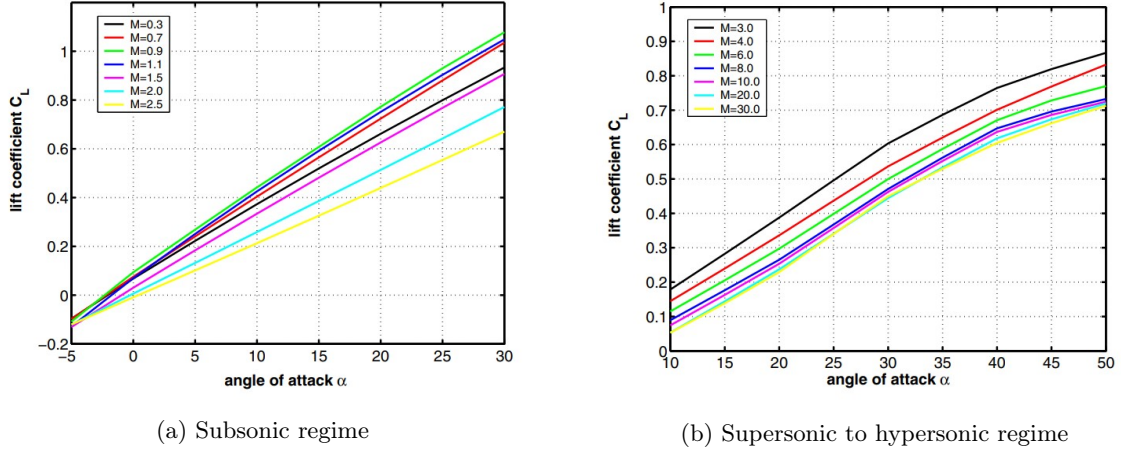
Figure 3.7: Lift coefficient C_L as a function of the angle of attack α for subsonic up to hypersonic Mach numbers, Hermes [2]

(a) Subsonic regime

(b) Supersonic to hypersonic regime
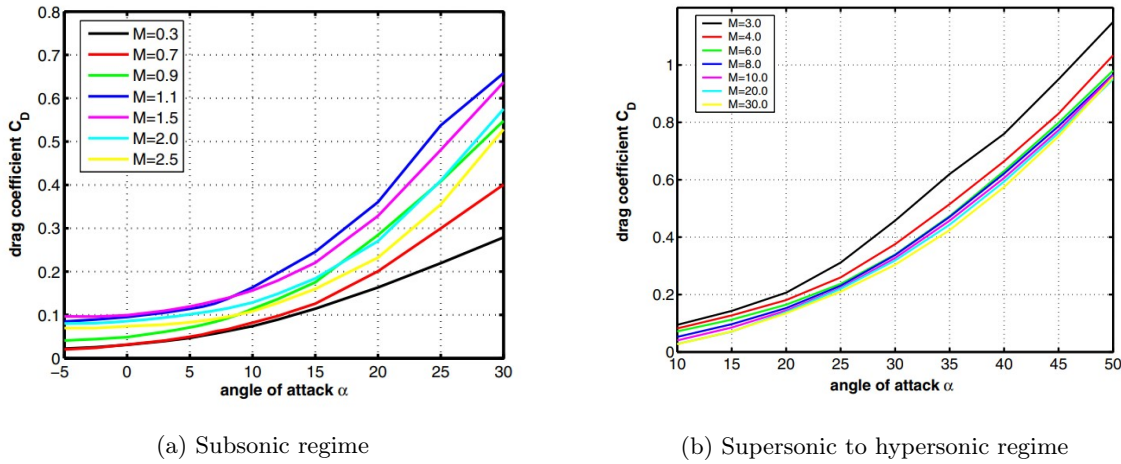
Figure 3.8: Drag coefficient C_D as a function of the angle of attack α for subsonic up to hypersonic Mach numbers, Hermes [2]

3.1.3 X33

With the development and launch of the Space Shuttle, NASA was able for the first time to carry payloads and crews into orbit and return them to Earth in a reusable vehicle. Prior to the Space Shuttle, this had been done in capsules, where the cost per mass of payload to be carried was very high. The Space Shuttle program was designed to reduce these costs by using a reusable aircraft. However, the exorbitant refurbishment costs the Shuttle between flights caused the program to be cancelled. To overcome this problem the NASA had thought about a fully reusable SSTO space vehicle having a combined ram/scram/rocket propulsion system, which is able to start and land horizontally. But it turned out that the technological challenges were so exceptional, that a realization was not possible at that time. So, NASA launched a research program in 1996 in order to develop and then to test key technologies with specific experimental vehicles[2]. One of these vehicles was the X33 .

Figure 3.10: X-33 demonstrator: view from rear (left), vehicle in launch position (middle), front view (right) [2]

The X-33 demonstrator was a single stage to orbits RLV with the capability to launch vertically and to land horizontally on a runway. The propulsion system consist on two linear aerospike engines. Technical and costs concerns led to the cancellation of the project in 2001.
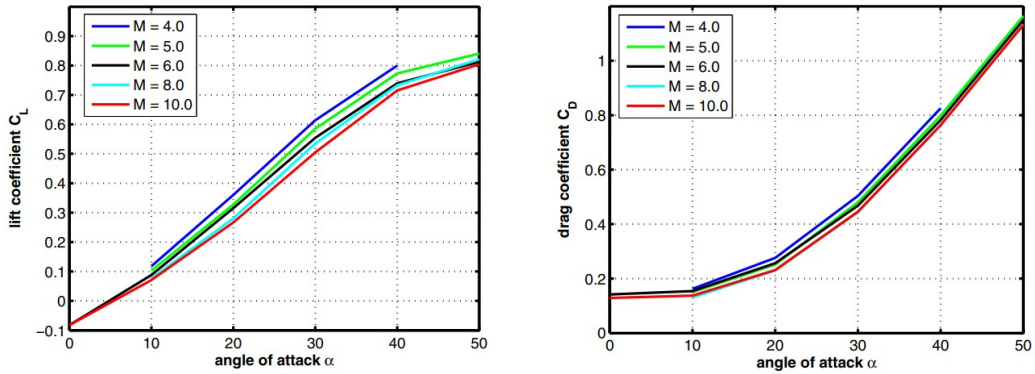
Figure 3.11: Lift and Drag coefficients as function of the angle of attack α for supersonic-hypersonic Mach numbers, X33 [2]
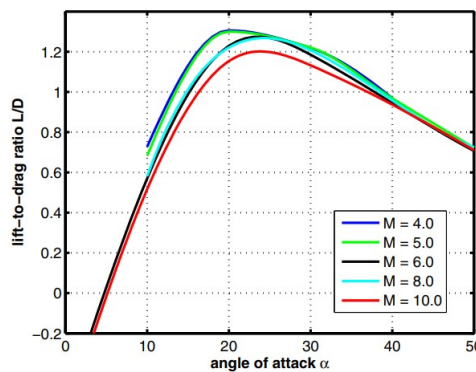
Figure 3.12: Lift to Drag ratio as function of the angle of attack α for supersonic-hypersonic Mach numbers, X33 [2]

3.1.4 X34

In the early 1990s, NASA launched a new program called NASP (National Aerospace Plane Program) to develop and demonstrate hypersonic technologies with the goal of reaching orbit with a single-stage

vehicle [20]. However, that program was canceled in 1993 while, in 1996, he launched a new activity called the Reusable Launch Vehicle Technology Program, a partnership among NASA, the U.S. Air Force and private industry. This program had encompassed three demonstrator vehicles, with the primary goal to develop and investigate key technologies, which should significantly lower the cost of access to space, necessary for the design and operation of a future reusable launch vehicle [2]. One of these demonstrator vehicles was indeed the X34 developed by the Orbital Sciences Corporation to serve as test bed for new technologies and operations. Some of these were:

- Reusable composite propellant tanks.
- Advanced thermal protection system (TPS)
- Rapid turnaround times.
- Autonomous flight including automatic landing

Figure 3.13: The X-34 vehicle underneath of the L-1011 carrier (left), free flight test (right) [2]

The geometric configuration of X34 is roughly similar to that of the Space Shuttle. The aircraft has a delta wing with a sweep angle of 45°. The reference value are listed below:

X-34 reference values	
Reference length	16.43m
Reference width	8.45m
Reference heigth	3.61m
Reference area	33.21m

Table 3.3: Reference dimensions of the X-34 [2]

The aerodynamic database below was developed in the wind tunnel of NASA Langley's Research Center. The Mach number covered the range from 0.25 to 10, and the angle of attack that from $-5°$ to 40°. The drag at given angle of attack α has a maximum for transonic speed ($M = 1.05$). Around zero angle of attack the subsonic drag ($M = 0.4$) and the hypersonic drag ($M = 6$) have similar value. The aerodynamic performance L/D has its maximum value for the subsonic Mach number $M = 0.4$ with $L/D_{max} \approx 7$ at $\alpha_{max} \approx 7°$. With increasing Mach number the maximum value decreases [2].
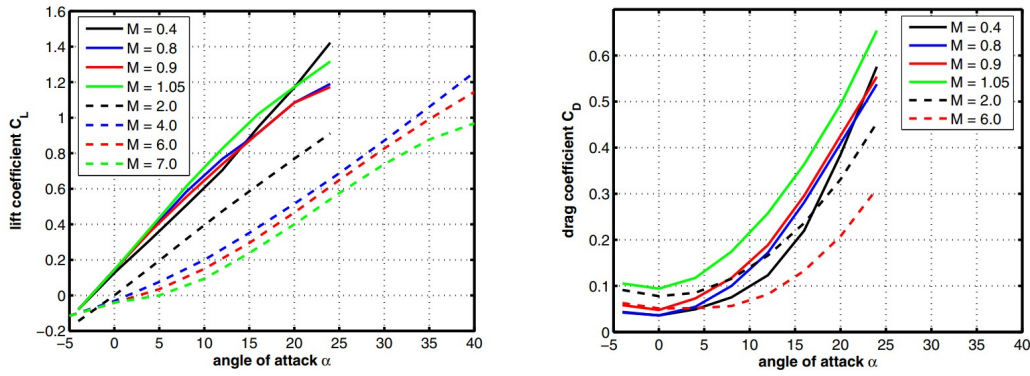
Figure 3.14: Lift and Drag coefficients as function of the angle of attack α for subsonic-supersonic-hypersonic Mach numbers, X34 [2]
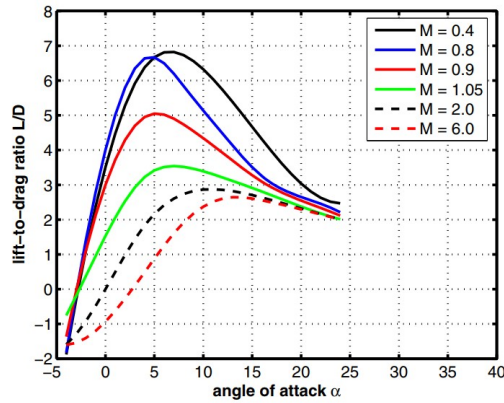

Figure 3.15: Lift to Drag ratio L/D as function of the angle of attack α for subsonic-supersonic-hypersonic Mach numbers, X34 [2]

3.1.5 X38

The X38 was a reentry vehicle developed in 1990. NASA planned to develop a Crew Rescue Vehicle to replace the Russian Soyuz capsule and also, if necessary, the Space Shuttle for those operational missions in connection with the International Space Station (ISS). The vehicle had to have the following features [2]:

- accurate and soft landing to allow for the transportation of injured crew members.
- load factor minimization.
- sufficient cross-range capability for reaching the selected landing site also at adverse weather conditions,

The main goal of the project was to enable the vehicle, and thus the crew, to return via a un-piloted mission so, the aircraft could operate automatically. The X38, after the de-orbit boost, would re-enter the Earth's atmosphere through a un-powered gliding trajectory, behaving as a winged aircraft. The final stage of the descent and landing was accomplished together with a steerable heavy load parafoil system [2]. Initially, X38 was to be carried into orbit by the Space Shuttle and then docked to the ISS. In fact, the spacecraft had a docking port on top. In 2002, however, NASA abandoned this goal and changed the strategy to one in which the X38 would be able to carry crew members to and from the ISS by performing an autonomous ascent. In 2002, NASA cancelled the X38 project.

Figure 3.16: Drop test including parafoil landing of the X-38 vehicle [2]

The X-38 vehicle is a lifting body, which does not strictly belong to the class of winged re-entry vehicles. Classical winged re-entry vehicles are able to conduct the landing by its own shape, which means that their shape produces in the subsonic flight regime at the minimum a L/D value of 4.5 to 5 When we look upon the subsonic aerodynamic performance of the X-38 vehicle, we find a L/D of order 2, which is far below the required value. This is the reason, why the final descent and landing of the X-38 vehicle is carried out with a steerable parafoil system . The data for supersonic and hypersonic regime were obtained mainly from wind tunnel investigations and some Navier-Stokes computations. For supersonic Mach numbers the aerodynamic performance L/D is of order 1.4, which diminishes to 1.3 for hypersonic Mach numbers. Further one can observe that the aerodynamic coefficients become asymptotically independent of the Mach number above $M \approx 5$ [2].
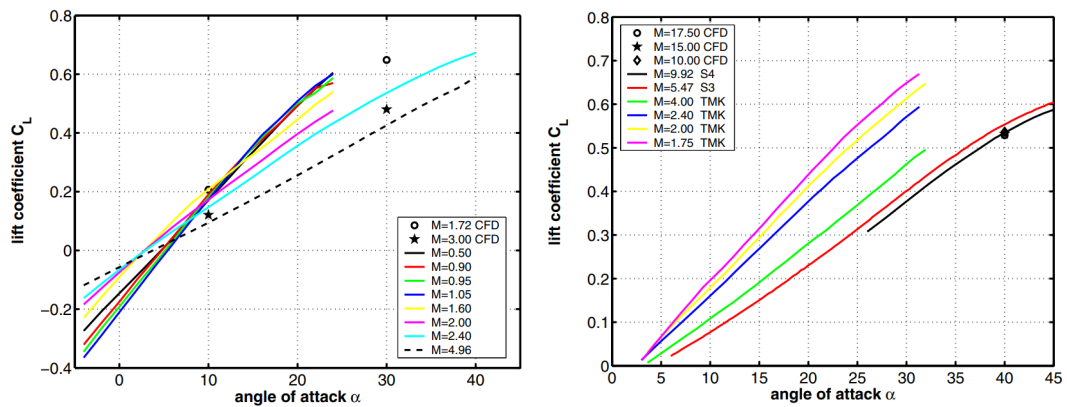

Figure 3.17: Lift coefficient C_L as function of the angle of attack α for subsonic-supersonic-hypersonic Mach numbers, X38 [2]

27
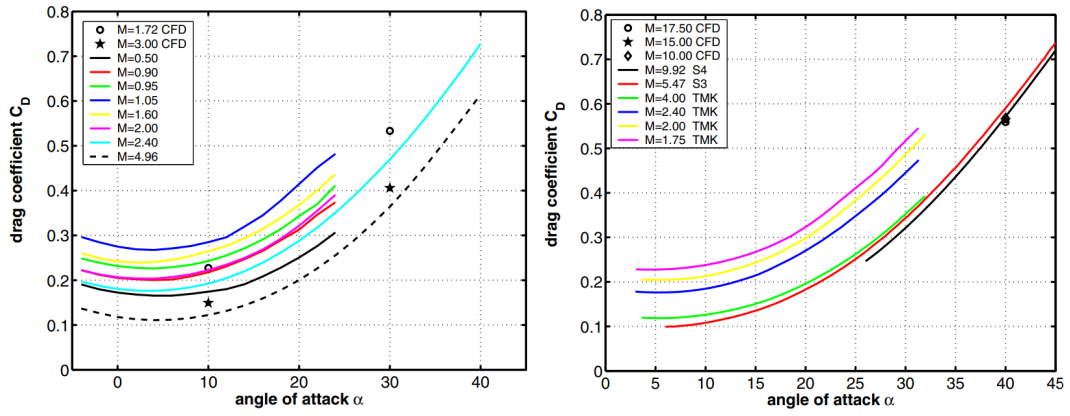
Figure 3.18: Lift coefficient C_D as function of the angle of attack α for subsonic-supersonic-hypersonic Mach numbers. X38 [2]
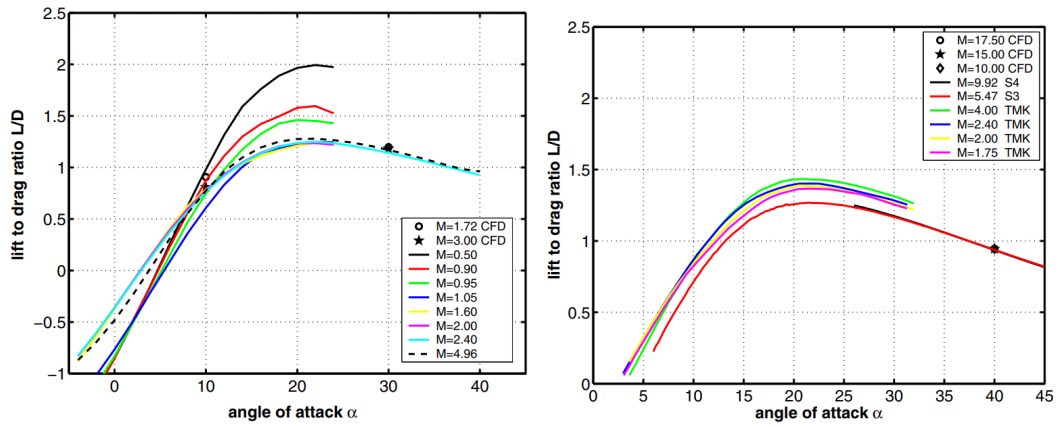

Figure 3.19: Lift to Drag ratio L/D as function of the angle of attack α for subsonic-supersonic-hypersonic Mach numbers, X38 [2]

3.1.6 HopeX

In 1990, Japan launched the HOPE-X project to develop a conceptual re-entry vehicle that would carry payloads to and from the ISS. However, this project reached the same goal as those of other countries, such as HERMES for Europe, and thus the HOPE-X program was terminated in 2003 due to economic constraints. The HOPE-X shape has a double delta type wing, similar to that of the
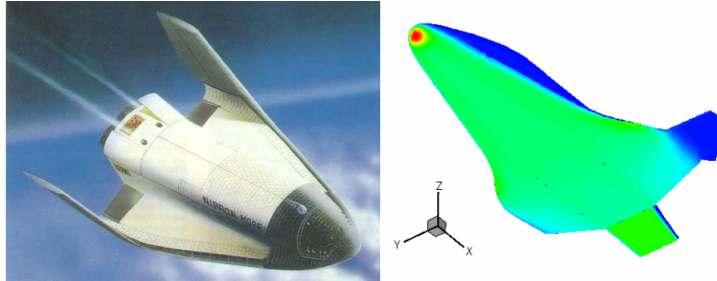
Figure 3.20: HOPE-X shape: (left), surface pressure distribution for $M = 3$ and $\alpha = 35$ (right)

SPACE SHUTTLE Orbiter. For the control of the lateral motion the designers installed winglets at the wing tips comparable to the ones of the HERMES and the X-38 vehicle [2]. The aerodynamic database for the longitudinal motion was given for Mach numbers in the range $0.2 \leq M \leq 3.5$ and angle of attack of $-5° \leq M \leq 30°$. The behavior of the lift coefficient C_L in the subsonic-transonic regime shows only minor variations in slope, but deviates for the Mach numbers M = 0.8 and 0.9 somewhat from linearity. The drag coefficient C_D in the subsonic-transonic regime increases in general with Mach number. Beyond Mach number one, where one expects to have the highest drag, the CD values continuously decrease with growing Mach number [2].
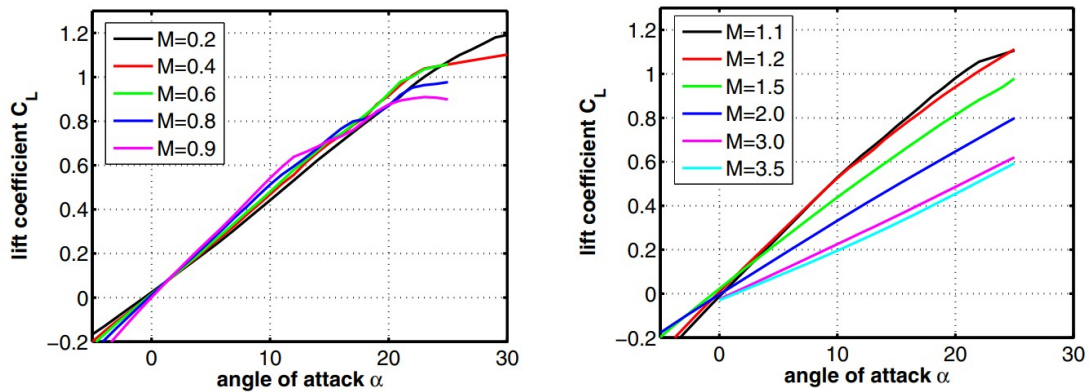

Figure 3.21: Lift coefficient C_L as a function of the angle of attack α for subsonic-supersonic-hypersonic Mach numbers, HOPEX [2]
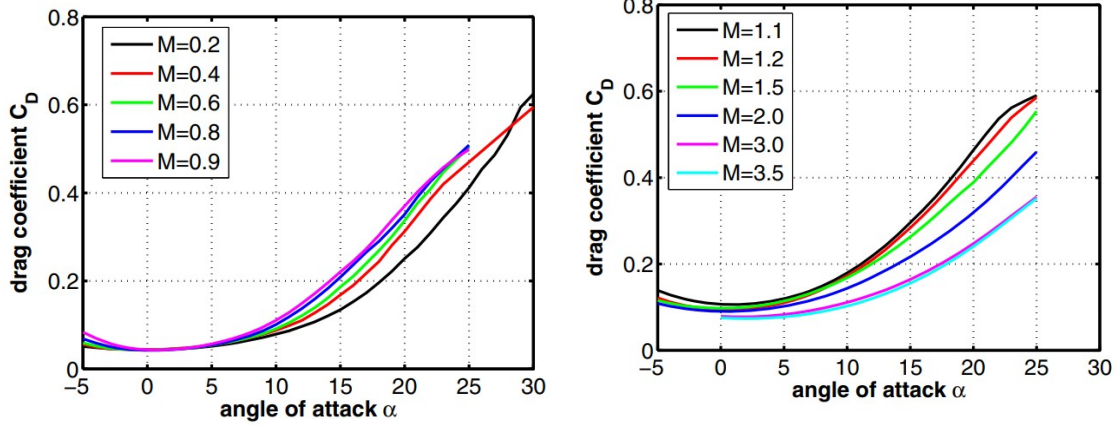
Figure 3.22: Drag coefficient C_D as function of the angle of attack α for subsonic-supersonic-hypersonic Mach numbers, HOPEX [2]
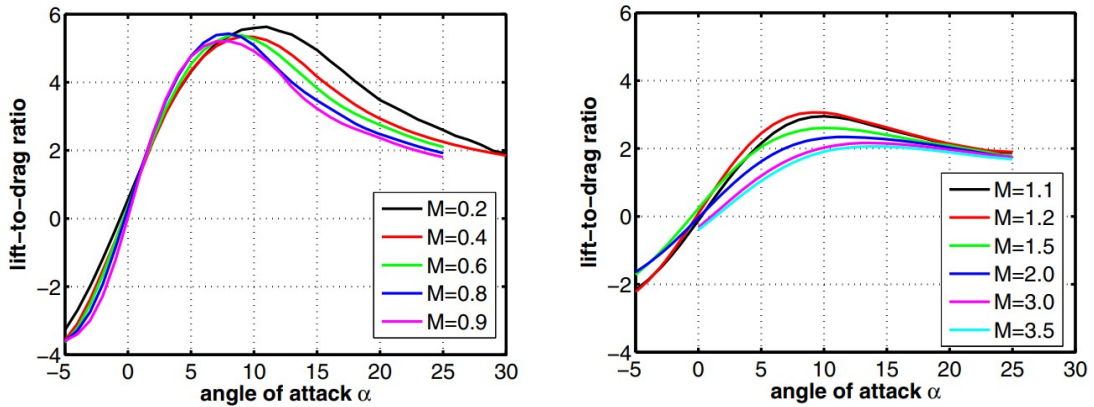

Figure 3.23: Lift to Drag ratio L/D as function of the angle of attack α for subsonic-supersonic-hypersonic Mach numbers, HOPEX [2]

Chapter 4

Re-Entry Vehicle Particle Mechanics

Atmospheric re-entry is quite a complex problem. During descent, the aircraft experiences different conditions. Below an altitude of approximately 60 km, atmospheric contact forces become comparable to the gravitational forces[7]. Therefore, aerodynamic forces must be include in trajectory modeling. At much lower altitude, these aerodynamic forces dominate the motion and, in some case, the gravitational forces can be ignored.

In a more complete discussion, the equations of motion are derived by considering flying in an atmosphere of a rotating planet. In addition, several reference systems must be considered. These are the *inertial geocentric-equatorial system*, *a planet-fixed rotating system*, and a *vehicle-pointing frame*. For the purpose of this thesis and the design phase of this work, we can consider the case of *planar flight*. This allows us to compare the parameters involved in atmospheric reentry. We'll further simplify the problem by assuming planetary rotation is negligible during the entry phase. These assumptions aren't as restrictive as they might seem. Ignoring the rotation of the planet is justified due to the small amount of rotation that occurs during short entry phases[21].

4.1   Atmospheric model

In order to properly study the problem of atmospheric re-entry, we first need to have an appropriate model of the Earth's atmosphere. Along its path, the Re-entry Vehicle (RV) is subject to gravitational forces as well as aerodynamic forces. While the former are present throughout the re-entry phase, aerodynamic forces are present only below 50km, beyond which the dynamic pressure increases.

An atmospheric model must be able to represent the vertical variation of pressure, density, and temperature. We expect atmospheric properties to vary not only with time but also with location; for example, we would expect such properties to vary with latitude and longitude. Nevertheless, we will limit our studies here to representing the atmosphere by a single model. Such a standard atmospheric model may be useful in evaluating the main performance of a re-entry vehicle. Throughout our work, we will use the Standard Atmosphere, defined by the World Meteorological Organization (WMO). The Standard Atmosphere is a unified representation of primary properties (pressure and temperature) and derived properties (density, viscosity, speed of sound propagation, mean free path length, etc.) with respect to altitude.

The U.S. Standard Atmosphere 1976 is an atmospheric model that meets the requirements of the WMO. The model covers the atmosphere from the Earth's surface to an altitude of *1000 km* at a latitude of *45°N*. The defining atmospheric elements are sea-level values of temperature and pressure

and segmented layers over which the molecular temperature has a defined altitude profile. The atmospheric region from sea level to 86 km is divided into seven layers.

Within each strata, the molecular temperature is represented as a linear function of geopotential altitude as:

$$T_M = T_{M_i} + L_{h_i} \cdot (h - h_i)$$

where i identifies the layer and:

$$L_{h_i} = \frac{dT_M}{dt}$$

where L_{h_i} represent the thermal lapse rate. The lapse rate can be positive, negative or zero. Layers having a zero lapse rate are identified as being isothermal.

In our model we use a sort of hybrid atmosphere, the *1976 Standard Atmosphere*, from sea level to a geometric altitude of *86 km*, and the *1962 Standard Atmosphere above 86 km*. This is because in the Standard 1976 Atmosphere, above 86 km altitude, the temperature does not vary linearly [7]. Instead, it follows an exponential trend. Therefore, to avoid these complexities, we use this hybrid model.

Layer index	Altitude [km]	Molecular Temperature $T_M[K]$	Lapse Rate $L_h[K/km]$
1	0	288.15	-6.5
2	11	216.50	0
3	20	216.50	+1
4	32	228.650	+2.8
5	47	270.650	0
6	51	270.650	-2.8
7	71	214.650	-2
8	84.852	186.946	+1.6481
9	100	210.02	5
10	110	257	10
11	120	349.49	20

Table 4.1: Atmospheric Model

With this hybrid model, one can derive altitude-dependent trends for temperature, pressure, and density. Existing formulas in the literature describe the relationship between pressure and density with altitude. For example, pressure variations depend on whether an isothermal layer is considered or not. Formulas are available for both scenarios [7].

For an isothermal case ($\Gamma_i = 0$):

$$P(h) = P_i(h) \cdot \exp\left(-\frac{g_0(h - h_i)}{RT}\right) \tag{4.1}$$

Instead, for a non-isothermal layer ($\Gamma_i \neq 0$)

$$P(h) = P_i(h) \cdot \left[\left(\frac{\Gamma_i}{RT}\right)(h - h_i) + 1\right]^{-\frac{g_0}{R\Gamma_i}} \tag{4.2}$$

The demonstration of these formulas is beyond the scope of this paper. To derive the density trends, knowing those for temperature and pressure, the perfect gas law can be used. Using these formulations it is possible to derive the trends of temperature, pressure and density as the altitude changes. The density, shown in Fig. 4.3 according to the perfect gas law can be calculated as follow:

$$\rho(h) = \frac{M}{R}\frac{P(h)}{T(h)} \tag{4.3}$$

It can be seen from the figure, that the temperature follows the layered pattern studied earlier. In particular, we can visualize the layers within which the temperature remains constant as the altitude changes. For re-entry into the Earth's atmosphere, constants of the model are:

$$M = 28.9644 \cdot 10^{-3} \quad \text{kg} \cdot \text{mole}^{-1}$$

$$g(0) = 9.80655 \quad \text{m} \cdot \text{s}^{-2}$$

$$R_t = 6378000 \quad \text{km}$$

$$P(0) = 101325 \quad \text{Pa}$$
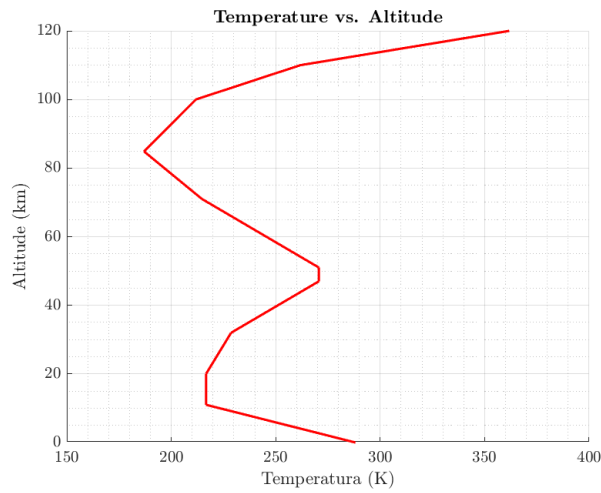
Figure 4.1: Temperature distribution with respect to altitude

To better visualize the pressure trend, the altitude was divided into two ranges.
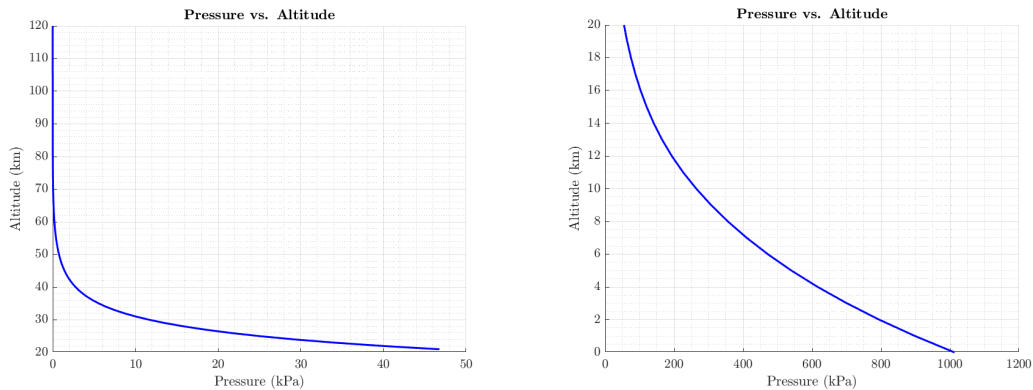
(a) Pressure distribution with respect to altitude up to 20km

(b) Pressure distribution with respect to altitude above 20km

Figure 4.2: Pressure distribution with respect to altitude
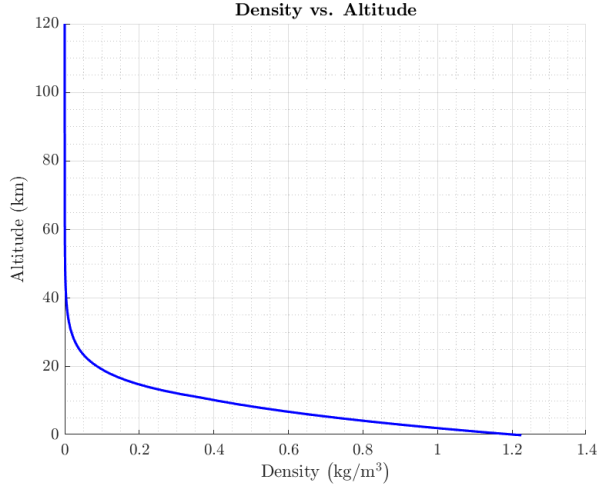
Figure 4.3: Density distribution with respect to altitude

4.2   Equations of Motion of Planar Flight

This section will present the equations of motion for a re-entry aircraft. To write any system of equations of motion, one must first consider a given reference system. In Fig. 4.4 three possible reference systems are described [7].

1. An inertial frame such that the $X^I Z^I$-plane contains the velocity vector V throughout the motion

2. A local frame such that the $X^l Z^l$-plane is that of the local horizontal, i.e., the Z^l-axis is along the local vertical

3. A moving frame attached to the RB such that the $X^m Z^m$-plane is coincident with the trajectory plane and the X^m-axis is along the velocity vector at all times
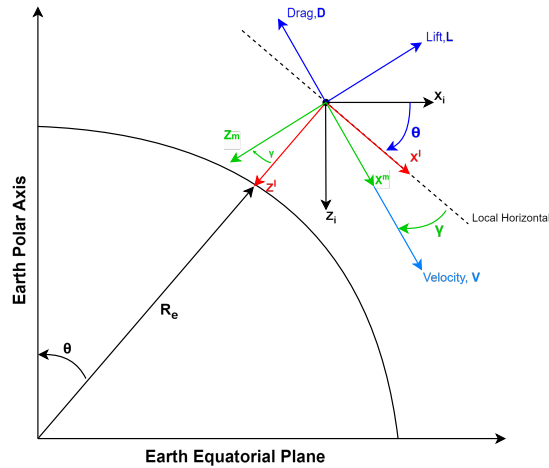
Figure 4.4: Planar entry tracjectory [7]

To obtain the equations of motion, Newton's law is applied. At any instant, the total force, $\vec{F}$, acting on the point mass is given by:

$$\vec{F} = \vec{T} + \vec{A} + m\vec{g} \tag{4.4}$$

where $\vec{T}$ is the thrust force, $\vec{A}$ is the aerodynamic force (lift and drag), m is the mass of the vehicle and $\vec{g}$ is the gravity force. The thrust force can be neglected, since the re-entry is an unpowered flight.

Much of the motion we wish to describe is more conveniently measured relative to the planet-fixed (i.e. rotating) reference frame. The vehicle is considered to be a particle of constant mass which moves in a plane with respect to a spherical, non-rotating Earth. Newton's Second Law of Motion can be applied, so:

$$m\frac{d\vec{V}}{dt} = \vec{F} = \vec{A} + m\vec{g} \tag{4.5}$$

It is subject to the action of three forces: the inverse-square gravitational field of the earth, its lift, and its drag. The variation of air density with respect to altitude is also included. In general, the study of atmospheric re-entry includes both translational and rotational motion. In addition, the aircraft is moving in the atmosphere of a rotating planet. To qualitatively compare the entry trajectories, we will examine the relatively simple case of motion restricted to a single " entry plane."

It was considered a planar re-entry. Planar entry is defined as motion confined to the plane of a great circle. Such a plane contains the vehicle's radius and velocity vectors and the planet's center point[21]. The geometry of atmospheric entry for planar flight over a spherical, non-rotating planet is shown in the Figure 4.5. As already mentioned, to simplify the problem we assume the Earth's rotation negligible during the entry phase. Of course, precise speed or position requirements would invalidate these assumptions, but they are sufficient for an initial study [21].
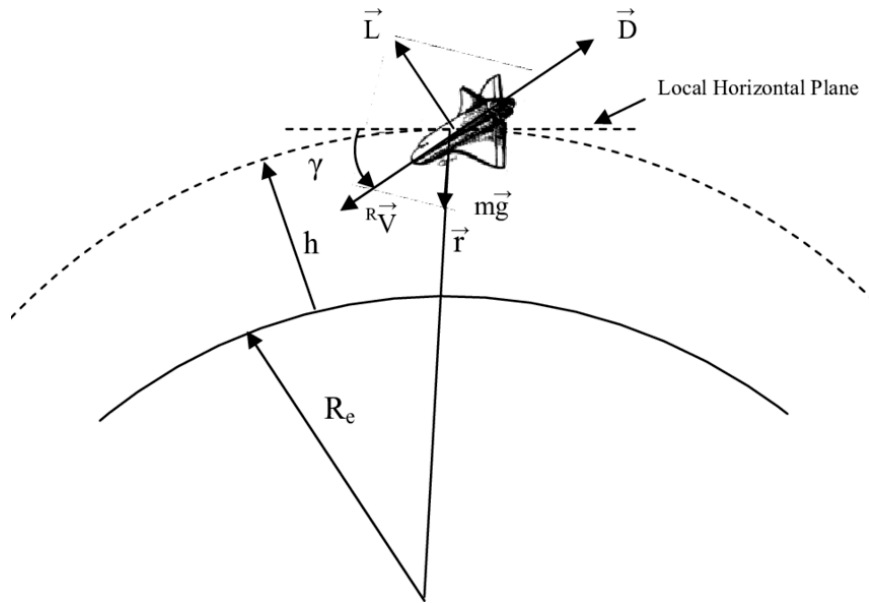
Figure 4.5: Two-Dimensional View of Planar Entry [7]

To maintain planar flight, assume there is no banking of the lift vector and no thrust force. The equations of motion are given below [21].

$$\dot{V} = -\frac{D}{m} - gsin\gamma \tag{4.6}$$

$$V\dot{\gamma} = \frac{L}{m} - gcos\gamma + \frac{V^2}{r}cos\gamma \tag{4.7}$$

$$V\dot{\psi} = -\frac{V^2}{r}cos\gamma \cdot cos\psi \cdot tan\phi \tag{4.8}$$

$$\dot{r} = \frac{dh}{dt} = -Vsin\gamma \tag{4.9}$$

$$\dot{\theta} = \frac{V cos\gamma \cdot cos\psi}{r cos\gamma} \tag{4.10}$$

$$\dot{\phi} = \frac{V cos\gamma \cdot sin\psi}{r} \tag{4.11}$$

where V is the velocity of the vehicle, γ is the flight path angle measured from the local horizontal and r the radial distance from the center of the planet. Moreover, ϕ represent the latitude, θ the longitude and ψ the heading angle. The Eq. (4.9), (4.11), (4.10) represent the kinematic equations. When integrated, they provide the position of the vehicle as seen from the planet. Indeed, Eq. (4.6), (4.7), (4.8), when solved simultaneously with the kinematic equations, describe the velocity of the vehicle and its orientation.

The three kinematic and three force equations together are the equations of motion and their solutions give the six independent parameters $(h, \theta, \phi, V, \gamma, \psi)$ required to define the motion of a point mass at any time. Since we ignored the planet's rotation, the planet's relative velocity and inertial velocity are the same. In other words, the Coriolis and centripetal acceleration have been neglected [6]. This assumption is appropriate since the effects of the rotating atmosphere on the vehicle are small compared with aerodynamic forces due to the vehicle's velocity. These equations must be solved simultaneously to obtain the magnitude of velocity and radius (or, equivalently, altitude) as a function of time, knowing entry interface conditions (r_e, V_e, γ_e), a model for atmospheric density $\rho(h)$, and specified values of the aerodynamic coefficients C_L and C_D. Lift and Drag are written as:

$$L = \frac{1}{2}\rho V^2 S C_L \tag{4.12}$$

$$D = \frac{1}{2}\rho V^2 S C_D \tag{4.13}$$

where ρ is the atmospheric density. C_L and C_D are the coefficients of lift and drag, respectively and S is a reference area used in calculating these coefficients. In general, C_L and C_D are functions of angle of attack α, Mach number M, and Reynolds number Re:

$$C_L = C_L(\alpha, M, Re) \tag{4.14}$$

$$C_D = C_D(\alpha, M, Re) \tag{4.15}$$

The drag coefficient may be written in terms of the ballistic coefficient β defined as:

$$\beta = \frac{W}{C_D S} = \frac{mg}{C_D S} \tag{4.16}$$

and the lift coefficient may be defined in terms of the lift to drag ratio as follows:

$$C_L = \left(\frac{C_L}{C_D}\right) C_D = \left(\frac{C_L}{C_D}\right) \frac{S\beta}{W} \tag{4.17}$$

The gravity is a function of radius and can be written as:

$$g(r) = g_0 \left(\frac{r_0}{r}\right)^2 \tag{4.18}$$

with r_0 the reference radius and g_0 the gravity constant at that radius. With these assumptions the equations Eq. (4.6) (4.7), (4.9) become:

$$\frac{dh}{dt} = -V sin\gamma \tag{4.19}$$

$$\dot{V} = -\left(\frac{\rho g}{2\beta}\right)V^2 + g sin\gamma \qquad (4.20)$$

$$V\dot{\gamma} = -\left(\frac{\rho g}{2\beta}\right)V^2\left(\frac{C_L}{C_D}\right) + cos\gamma\left(g - \frac{V^2}{R_e + h}\right) \qquad (4.21)$$

It can be seen that the amount of deceleration an aircraft experiences is inversely proportional to the ballistic coefficient. In particular, an object with a low β slows down much quicker than an object with a high β. A blunt vehicle (low β) slows down much more rapidly than a heavy, streamlined (high β) one [8]. These equations are integrated over time through the *fourth-order Runge-Kutta method* (RK4), which will be seen in the following chapter, knowing the initial conditions (H_0, V_0,γ_0, ψ_0, ϕ_0, θ_0).

The input data considered in this thesis are those depicted in the Table 4.2 and obtained through the sizing code constructed in the research project, described in Chapter 1 [3]:

Input data	
Re-entry weight	55648 kg
S_{pln}	382 m^2
C_D	0.5
L/D	1.5
β	$2.9 \cdot 10^3$ Pa

Table 4.2: Input data or the Skylon spaceplane [3]

4.3   Runge-Kutta method of 4th order

Runge–Kutta method is an effective and widely used method for solving problems involving differential equations. Runge–Kutta method can be used to construct high order accurate numerical method without needing the high order derivatives of functions. There are several version of the method depending on the desired accuracy. The most popular Runge-Kutta method is of fourth order, which in simpler terms means that the error is of the order of h^4. Consider the problem;

$$\begin{cases} y^{'} = f(t,y) \\ \\ y(t_0) = \alpha \end{cases}$$

Define h to be the step size and $t_i = t_0 + ih$. The Runge-Kutta method is defined as:

$$\begin{cases} y(a) = y_0 \\ \\ y_{n+1} = y_n + h\sum_{n=1}^{N}c_i k_i^n, \quad 0 \leq n \leq N-1 \end{cases}$$

with $k \in \mathbb{N}$ and the coefficient k_i^n are functions defined as:

$$\begin{cases} k_1^n = f(x_n, y_n) \\ \\ k_i^n = f\left(x_n + a_i h, y_n + h\sum_{j=1}^{i-1}b_{ij}k_j^n\right), \quad 2 \leq i \leq k \end{cases}$$

The fourth-order Runge-Kutta algorithm is obtained for $k = 4$ [22]. It can be written:

$$\begin{cases} y(a) = y_0 \\ \\ y_{n+1} = y_n + \frac{h}{6}(k_1^n + 2k_2^n + 2k_3^n + k_4^n), \quad 0 \leq n \leq N-1 \end{cases}$$

with the coefficient k_i^n definend as:

$$
\begin{cases}
k_1^n = f(x_n, y_n) \\[2em]
k_2^n = f(x_n + \frac{h}{2}, y_n + \frac{h}{2}k_1^n) \\[2em]
k_3^n = f(x_n + \frac{h}{2}, y_n + \frac{h}{2}k_2^n) \\[2em]
k_4^n = f(x_n + h, y_n + hk_3^n)
\end{cases}
$$

Intuitively, Runke-Kutta methods discretize the domain defined by the independent variable x in steps defined by h, and for each point x_n of the discretization, the value of y' is calculated at the points of the environment of x_n, i.e. the coefficients k_i^n. From the current value y_n of the function and the coefficients it is calculated the next value of the function, y_{n+1}. Numerical methods are, in general, approximations to the analytical solution of the problem. The accuracy of the approximation depends on h. However, the *RK4 method* is of global order 4, i.e. the error is of order $O(h^4)$. This implies that if h is defined as $h' = h/2$ and apply the *RK4* algorithm again, the error will be reduced 16 times

4.4   Numerical resolution of equations of motion

The system of differential equations for the case of a lifting re-entry can be written as:

$$\frac{dV}{dt} = f_1(t, V, \gamma, \psi, h, r, \phi, \theta) \tag{4.22}$$

$$\frac{d\gamma}{dt} = f_2(t, V, \gamma, \psi, h, r, \phi, \theta) \tag{4.23}$$

$$\frac{d\psi}{dt} = f_3(t, V, \gamma, \psi, h, r, \phi, \theta) \tag{4.24}$$

$$\frac{dh}{dt} = f_4(t, V, \gamma, \psi, h, r, \phi, \theta) \tag{4.25}$$

$$\frac{dr}{dt} = f_5(t, V, \gamma, \psi, h, r, \phi, \theta) \tag{4.26}$$

$$\frac{d\phi}{dt} = f_6(t, V, \gamma, \psi, h, r, \phi, \theta) \tag{4.27}$$

$$\frac{d\theta}{dt} = f_7(t, V, \gamma, \psi, h, r, \phi, \theta) \tag{4.28}$$

To solve this system of differential equations, one must define the initial conditions at the initial time t_0, which are the initial altitude h_0, initial velocity V_0, and flight path angle γ_0 at the entrance of atmospheric re-entry.

Initial Conditions	
Initial Velocity V	7.8 km/s
Initial Altitude h_0	120 km
Flight Path Angle γ_0	0.1°
Latitude ϕ_0	45°
Longitude θ_0	8°
Heading ψ_0	0°

Table 4.3: Initial Conditions

Next,a time-domain discretization is implemented, $I = [t_0, t_f]$, in $N + 1$ temporal instants separated by Δt. For the n-th iteration, with $0 \leq n \leq N$, the coefficients are calculated as:

$$i_1^n = f_1(t_n, V_n, \gamma_n, \psi_n, h_n, r_n, \phi_n, \theta_n) \tag{4.29}$$

$$j_1^n = f_2(t_n, V_n, \gamma_n, \psi_n, h_n, r_n, \phi_n, \theta_n) \tag{4.30}$$

$$k_1^n = f_3(t_n, V_n, \gamma_n, \psi_n, h_n, r_n, \phi_n, \theta_n) \tag{4.31}$$

$$l_1^n = f_4(t_n, V_n, \gamma_n, \psi_n, h_n, r_n, \phi_n, \theta_n) \tag{4.32}$$

$$m_1^n = f_5(t_n, V_n, \gamma_n, \psi_n, h_n, r_n, \phi_n, \theta_n) \tag{4.33}$$

$$n_1^n = f_6(t_n, V_n, \gamma_n, \psi_n, h_n, r_n, \phi_n, \theta_n) \tag{4.34}$$

$$o_1^n = f_7(t_n, V_n, \gamma_n, \psi_n, h_n, r_n, \phi_n, \theta_n) \tag{4.35}$$

To simplify the discussion, only the first of the coefficients listed above is given. The expressions of the other coefficients can be found in App. B.

$$i_2^n = f_1\left(t_n + \frac{\Delta t}{2}, V_n + \frac{\Delta t}{2}i_1^n, \gamma_n + \frac{\Delta t}{2}j_1^n, \psi_n + \frac{\Delta t}{2}k_1^n, h_n + \frac{\Delta t}{2}l_1^n, r_n + \frac{\Delta t}{2}m_1^n, \phi_n + \frac{\Delta t}{2}n_1^n, \theta_n + \frac{\Delta t}{2}o_1^n\right)$$

$$i_3^n = f_1\left(t_n + \frac{\Delta t}{2}, V_n + \frac{\Delta t}{2}i_2^n, \gamma_n + \frac{\Delta t}{2}j_2^n, \psi_n + \frac{\Delta t}{2}_2, h_n + \frac{\Delta t}{2}l_2^n, r_n + \frac{\Delta t}{2}m_2^n, \phi_n + \frac{\Delta t}{2}n_2^n, \theta_n + \frac{\Delta t}{2}o_2^n\right)$$

$$i_4^n = f_1(t_n + \Delta t, V_n + i_3^n\Delta t, \gamma_n + j_3^n\Delta t, \psi_n + k_3^n\Delta t, h_n + l_3^n\Delta t, r_n + m_3^n\Delta t, \phi_n + n_3^n\Delta t, \theta + o_3^n\Delta t,)$$

Finally, the values of the unknown variables at t_{n+1} can be calculated as explained in the section 4.3:

$$V_{n+1} = V_n + \frac{\Delta t}{6}\left(i_1^n + 2i_2^n + 2i_3^n + i_4^n\right) \tag{4.36}$$

$$\gamma_{n+1} = \gamma_n + \frac{\Delta t}{6}\left(j_1^n + 2j_2^n + 2j_3^n + j_4^n\right) \tag{4.37}$$

$$\psi_{n+1} = \psi_n + \frac{\Delta t}{6}\left(k_1^n + 2k_2^n + 2k_3^n + k_4^n\right) \tag{4.38}$$

$$h_{n+1} = h_n + \frac{\Delta t}{6}\left(l_1^n + 2l_2^n + 2l_3^n + l_4^n\right) \tag{4.39}$$

$$r_{n+1} = r_n + \frac{\Delta t}{6}\left(m_1^n + 2m_2^n + 2m_3^n + m_4^n\right) \tag{4.40}$$

$$\phi_{n+1} = \phi_n + \frac{\Delta t}{6}\left(n_1^n + 2n_2^n + 2n_3^n + n_4^n\right) \tag{4.41}$$

$$\theta_{n+1} = \theta_n + \frac{\Delta t}{6}\left(o_1^n + 2o_2^n + 2o_3^n + o_4^n\right) \tag{4.42}$$

Chapter 5

Re-Entry Corridor

During descent, the aircraft is subjected to a very aggressive aerothermodynamic field. The trajectory of the re-entry vehicle must have a certain profile so that the external environmental conditions do not threaten the survival of the vehicle. To ensure a vehicle survives atmospheric entry, it must meet a fairly restrictive set of conditions, trough the definition of the so-called re-entry corridor. The entry flight corridor defines the feasible domain within which a reference trajectory can be designed to achieve a safe flight. For a vehicle returning from orbital conditions, the re-entry corridor is defined by several path constraints [23]. Typically, the entry constraints are the heating rate at the stagnation point, the dynamic pressure, the axial acceleration and the equilibrium glide condition.

The maximum value of heat flux at the stagnation point and acceleration depend on the input conditions, i.e., the initial value of the flight path angle and the initial velocity. If the entry angle is too shallow, then the entry vehicle may not lose enough energy and the vehicle will pass through the atmosphere and escape to orbit or escape completely. This critical angle is called the skipout angle or overshoot boundary [6]. If the entry angle is too steep at its entry, the vehicle will be destroyed by dynamic or thermal loads. This is called the undershoot boundary. Between these two extremes is an entry corridor where the vehicle can be guaranteed to not only to be "captured" by the atmosphere but also to stay within its operational constraints [21].

Any flight that stays within the corridor is acceptable. If the vehicle deviates from this corridor, or if the lift is insufficient or excessive, it will either crash to the surface or deviate from the intended orbit. The performance characteristics of the vehicle depend only by two vehicle-design quantities: the vehicle's Lift to Drag ratio (L/D) and the ballistic coefficient β. Both of these quantities depend on the vehicle's lift and drag coefficient. An increase in the vehicle's L/D ratio improves its controllability and thus increases the corridor width. Increase in allowable g-load and in allowable maximum temperature also lead to increased allowable corridor width. Increased entry speed, increased flight path angle, and uncertainties in atmospheric density, reduce corridor width. The width of the re-entry corridor can be expanded by decreasing V_e or γ. Unfortunately, for most missions, V_e and γ are set by the mission orbit and are difficult to change significantly [8]. The mission itself is perhaps the most important consideration in determining the aerothermal environment.
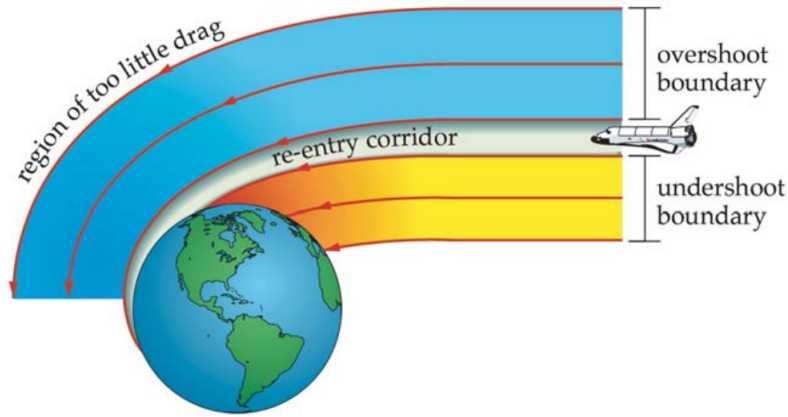
Figure 5.1: Re-entry corridor[8]

5.1   Drag-Velocity Map

From a more practical point of view, the re-entry corridor can be visualized in the Drag-Velocity (D-V) plane, as displayed in Fig. 5.2. This is more useful from a control point of view. Another type of visualization is the Altitude-Velocity (H-V) plane. Like visualized in Fig. 5.2, we can represent a flight corridor for a generic entry trajectory with four flight boundaries. The upper constraint boundaries (Boundaries 2,3,4 in Fig.5.2) are defined by load constraints, such as stagnation point heat rate, peak aerodynamic acceleration, and peak dynamic pressure. The lower constraint boundary (Boundary 1) determines the limit for trajectory control in terms of equilibrium glide flight for vehicles with L/D greater than 0.5 [9]. A vehicle is in equilibrium glide flight when the rate of change of the flight path angle is about zero. This type of drag-acceleration profile enables the vehicle to fly long distances.

In the following, we will present the aerodynamic and thermal constraints that the aircraft must meet, which will lead to the creation of the re-entry corridor. Next, we will represent the nominal flight profile that satisfies the requirements.
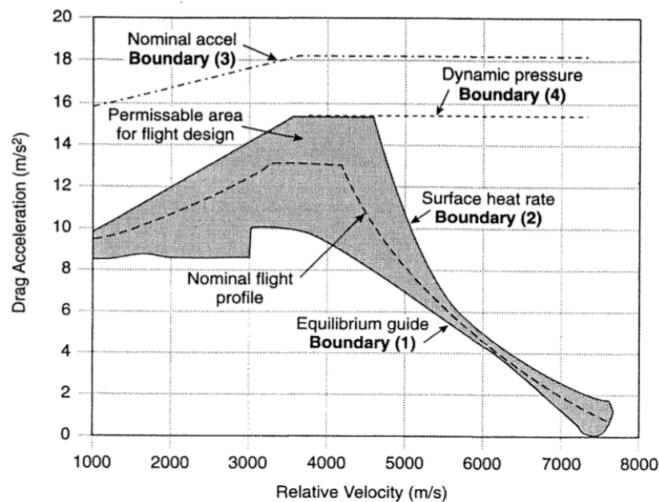

Figure 5.2: Constraints on the Entry Corridor for the X-38 vehicle [9]

5.1.1   Equilibrium Glide

At high speed lower than the satellite's local circular speed, we can define a drag reference that requires a minimum desidered bank angle to maintain. We can't maintain drag less than this value without violating the constraint line for a minimum bank angle. The equilibrium glide constraint can be calculated with Eq.5.1 whenever the entry flight path angle is shallow. We would set the bank angle to the minimum acceptable value. For the Space Shuttle and X38, this value is 37° for speed greater than 3048 m/s and 20° for lower speeds [9]. The lift to drag ratio is at the denominator, so vehicles with higher L/D can fly at lower drag-acceleration levels during the equilibrium glide phase. So having vehicle with higher L/D values means having longer-range trajectories, thus expanding the landing vehicle's footprint [9].

$$D_{glide} = \left[\frac{g_0 \left(1 - \frac{V^2}{V_{sat}^2} \right)}{\frac{L}{D} cos(\phi_{min})} \right] \tag{5.1}$$

where:

- $V_{sat} = 7.726 \, \text{m/s}$ is the orbital velocity;
- $L/D = 1.5$ is the Lift-to-Drag ratio for the Skylon;
- $\phi_{min} = 0°$ is the minimum bank angle. In this case, for the assumptions made, is equale to zero.

5.1.2   Maximum Heat Flux

During the first few seconds of an atmospheric re-entry, aerodynamic loads may be low because of the very rarefied atmosphere, but aerothermodynamic heating can be very high. Heating of aircraft systems depends on the thermal protection system being used. Generally, the heat flux depends on the location of the point where we are evaluating the heating. In this analysis, the stagnation point was considered, where there is the maximum heat transfer. This also depends on the radius of curvature of the profile in question. The smaller the surface's radius of curvature, the more heat flow it will experience. For preliminary comparison a 0.3048 m radius sphere value was considered. The heat rate constraint was computed trough the Detra-Kemp-Riddel heating equation for convective heating at stagnation point [9]:

$$\dot{Q} = C \cdot \left(\frac{1}{R_n} \right)^{0.5} \left(\frac{\rho}{\rho_0} \right)^{0.5} \left(\frac{V}{V_{sat}} \right)^{3.15} \text{W cm}^{-2} \tag{5.2}$$

where V is the vehicle's relative speed, $V_{sat} = 7.726 \, \text{m/s}$ is the orbital velocity; $\rho_0 = 1.225 \, \text{kg/m}^3$ is the sea level density; C is a constant. In the case of entry into the Earth's atmosphere, $C = 11030$ [9]; ρ_0 is the density at sea level. Not exceeding the constraint on heat rate ensures the integrity of the thermal protection system. Because the above equation uses cubic velocity (approximately), its derivative is quadratic. Drag acceleration is also quadratic in velocity [9] thus, we can compute the coefficients for a quadratic curve-fit on drag acceleration. This curve-fit is for constant heat rate. This curve-fit depends on the vehicles ballistic coefficient and on maximum value of heat flux, in this case equal to $100 \, \text{kW/m}^2$. We need three constants to define a quadratic curve-fit. We obtain:

$$D_{heat} = \Gamma_1 + \Gamma_2 V + \Gamma_3 V^2 \tag{5.3}$$

with:

Γ_1	145.7044
Γ_2	-0.0353
Γ_3	2.20e-6

Table 5.1: Coefficients for the quadratic curve-fit

5.1.3   Total Sensed Acceleration

Drag acceleration increases as the vehicles penetrates the planetary atmosphere. At some point the sensed amount of acceleration can violates constraints on the vehicle's structure, crew, dynamic pressure or moment around surface hinges. The following general constraint is posed:

$$n = \frac{Lcos\alpha + Dcos\alpha}{m} < n_{max} \tag{5.4}$$

Boundary 3 of Fig. 5.2 defines the constraint on sensed acceleration. To compute the total sensed acceleration we use the following equation [9]:

$$D_{acc} = \frac{G_{max}}{\sqrt{1 + (\frac{L}{D})^2}} \tag{5.5}$$

where G_{max} is defined as:

$$G_{max} = \frac{V_e^2 sin\gamma_e}{2eg_0 H_s} \tag{5.6}$$

with V_e the atmospheric entry speed, γ_e the flight path angle, and H_s the planet atmosphere density scale. However, a correction is necessary because we are dealing with a winged vehicle, so:

$$\frac{G_L}{G_{max}} = \frac{g_0 e^{\frac{2\gamma_e}{L/D}}}{L/D} \tag{5.7}$$

A chosen maximum value of total sensed acceleration implies a fixed value of reference drag, assuming the vehicle has a fixed angle of attack and, therefore a fixed value of lift to drag ratio. The Fig. 5.3 represents the acceleration in g along the trajectory, showing a maximum of about 0.6g. This is not particularly high, as the acceleration strongly depends on the L/D. Skylon has a very high L/D value of 1.5, which helps reduce acceleration. The results are consistent with those of the Space Shuttle, which had an L/D of 1 and experienced accelerations of about 0.9g [24].

5.1.4   Dynamic Pressure

The increasing dynamic pressure can cause excessive damage to the aircraft structure once the aircraft has passed the less dense layers of the atmosphere and penetrated to low altitudes. In addition, it can cause stability problems and stresses in the aerodynamic control surfaces. A limit is imposed to ensure structural safety, the constraint is given as:

$$q_{dyn} = \frac{1}{2}\rho V^2 \tag{5.8}$$

To calculate the dynamic pressure constraint, we use the Eq.5.9 :

$$D_{dyn} = \frac{Q_{max}}{\beta} \tag{5.9}$$

where $Q_{max} = 5kPa$ is the constraint for the maximum dynamic pressure for the Skylon spaceplane. Note that this equation also depends on the ballistic coefficient β, so modulating tha angle of attack affects the constraint boundary for dynamic pressure throught its correlation with aerodynamic drag.
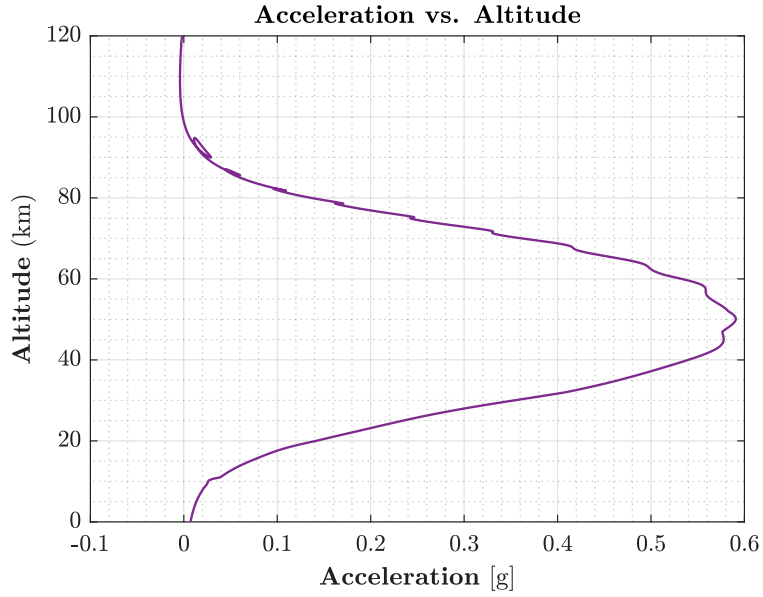
Figure 5.3: Acceleration trough the descent for the Skylon

Solving the equations of motion from Chapter 4, the dynamic pressure evolution along the trajectory is shown in Fig. 5.4. It can be seen that the peak dynamic pressure occurs in the lowest layers of the atmosphere, where the density is greatest.
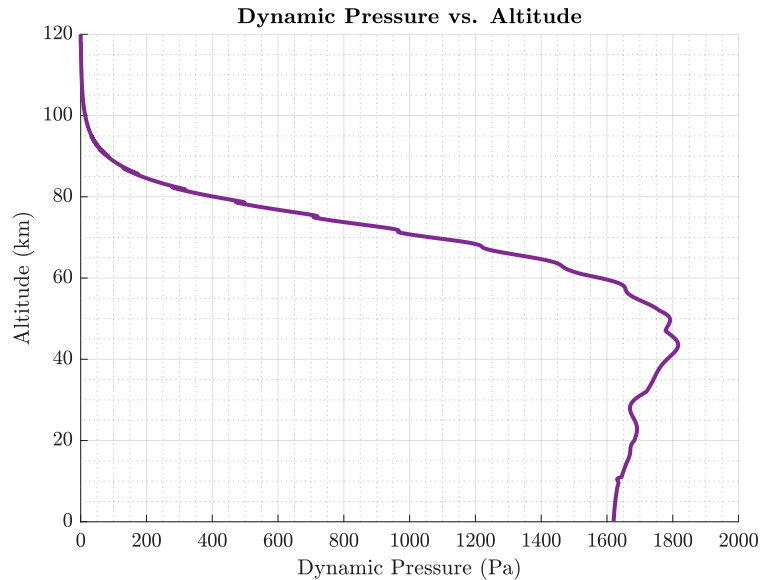

Figure 5.4: Dynamic Pressure for the Skylon

5.1.5 Nominal flight profile

The typical re-entry corridor, by defining the aerothermodynamic constraints within which the vehicle must fly to avoid mission failure, was developed. Now, we can generate the typical flight profile that the vehicle must follow to stay within the defined constraints. The nominal flight profile defines the undispersed trajectory design and the ideal path to follow. It's in the middle of the corridor to ensure that any accidents won't affect the descent. The nominal profile allows us to estimate nominal

environmental parameters such as heat flux, acceleration, and dynamic pressure of the reference aircraft [9]. In the next paragraphs will be explained how to create the reference profile inspired to the Space Shuttle phases.

Constant Heat Rate

During the initial moments of flight, the vehicle travels at high speeds, resulting in significant heat fluxes. If the temperature reaches very high levels, the vehicle cannot be considered reusable, as the structure of the TPS would suffer severe damage. Therefore, it is crucial to keep the vehicle at a safe temperature; this heating limit is identified by the heat flux limit within the re-entry corridor. To define the re-entry trajectory a first strategy is identify a reference profile with constant heat-rate [25]. The drag profile with constant heat-rate is represent by a quadric drag-velocity segment, as defined in Eq. 5.1.2. In our case, a nominal value of $80\,\mathrm{kW/m^2}$ has been chosen for the constant heat flux phase (with the maximum value set at $100\,\mathrm{kW/m^2}$). To define this profile the first step is identify three velocity: $V_1 = 7.8\,\mathrm{km/s}$ is the velocity at entry conditions, V_3 is the final point of the constant heat-rate phase, in this case is chosen equal to $5\,\mathrm{km/s}$, and V_2 is the average between V_1 and V_3. The drag profile with constant heat-rate is represent by a quadric drag-velocity segment, like the Eq. 5.1.2, for a nominal heat rate of $80\,\mathrm{kW/m^2}$:

$$D_{ref} = \Gamma_1 + \Gamma_2 V + \Gamma_3 V^2$$

Constant Drag

During the constant drag phase, the reference profile of the drag velocity is calculated to maintain a constant drag acceleration.

$$D_{ref} = \Gamma_4 \tag{5.10}$$

This phase limits the acceleration load and dynamic pressure experienced by the vehicle. During this phase, the speed decreases rapidly. The first step is identified the initial and final velocity for this phase. The final velocity is set to $2.5\,\mathrm{km/s}$ and the initial velocity is equal to V_3. For each velocity between this range is calculated the difference between the drag value of the lower boundary and the drag value for the upper boundary. The lower boundary is the equilibrium glide profile, while the upper boundary is one between the dynamic pressure constraint and the acceleration constraint. For each velocity, a value of the difference between the drag acceleration is calculated. To compute the profile for the constant drag phase, the velocity with the minimum difference in drag is chosen, and for this value, it's computed the average between the upper limit and the lower limit. Subsequently, it is necessary to create the union between the constant drag phase and the constant heat rate phase. Through an interpolation, the intersection point is found, and thus the velocity at which the drag acceleration values for the two phases are equal [25].

Transition Phase

The last phase is a linear drag-energy reference acceleration. As velocity decreases, the flight angle increases, making the small approximation impractical . To simplify hypersonic equations and avoid integrating the range equation, we can exchange variables from velocity to energy. This allows us to define a linear drag profile based on the given final target energy value, initial and final velocity, and initial and final drag values [9]. Given the final targeted energy value E_f, inital and final drag value (D_f and D_i) and the inital and final velocity (V_f and V_i), the profile of linear drag versus energy

can be calculated. The velocities are known: the initial velocity is the one at the termination of the constant drag phase and the final velocity is the one that we want at the end of hypersonic flight and set equal to 800 km/s. The energy levels can be computed from approximate values of initial and final altitude (Eq. 5.11) and relative velocity.

$$h_{i,f} = h_0 - h_s * ln\left(\frac{2D_{i,f}\beta_{i,f}}{v_{i,f}^2 \rho_0}\right) \tag{5.11}$$

where $D_{i,f}$ is the initial or final drag acceleration. In this case, the initial and final drag values were taken equal to the constant drag value and the equilibrium glide constraint, respectively. So initial and final energy values can be calculated.

$$E_{i,f} = g_{i,f}h_{i,f} + \frac{v_{i,f}^2}{2} \tag{5.12}$$

Knowing the final conditions and the initial conditions, it's possible calculating the parameter Γ_5.

$$\Gamma_5 = \frac{D_i - D_f}{E_i - E_f} \tag{5.13}$$

Thus, the drag profile for the linear drag phase is represented by the following equation:

$$D_{ref} = D_f + \Gamma_5(E - E_f) \tag{5.14}$$

Considering the results obtained from the integration of the equations of motion, the following constraints were chosen:

Re-entry Corridor constraints	
Maximum Heat rate	$100\,\text{kW/m}^2$
Acceleration	$n_{max} = 2$
Max Dynamic Pressure	$5\ kPa$

Table 5.2: Re-entry Corridor constraints

The re-entry corridor in the Drag-Velocity map for the Skylon is shown in Fig. 5.5.
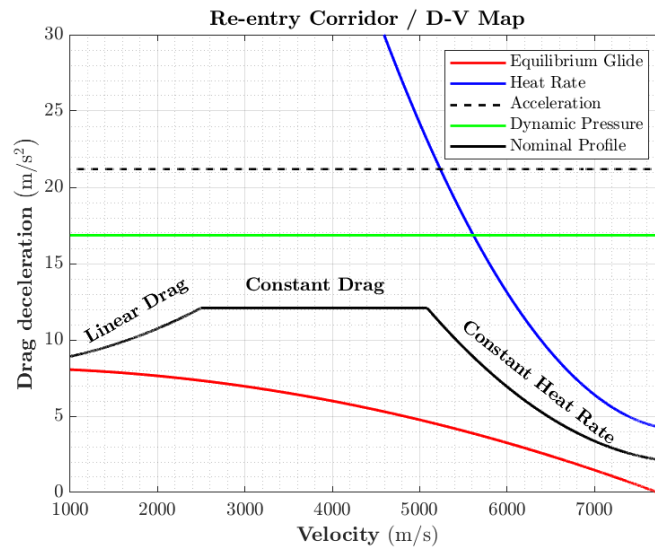

Figure 5.5: Entry corridor for the Skylon spaceplane in the D-V domain

5.2 Altitude-Velocity Map

As mentioned above, another type of graph to visualize the re-entry corridor is an altitude-velocity map. This requires finding a function that relates the change in altitude to velocity. The two quantities can be related by the density, which varies with altitude. This is done by the following relationship:

$$\rho = \rho_0 \cdot e^{-\frac{h}{H_s}} \tag{5.15}$$

For initial re-entry trajectory design, usually three conditions are taken into account:

- The equilibrium-flight condition:

$$\rho_{eq} = 2\frac{W/S}{C_L}\left(\frac{1}{\frac{1}{V^2} - \frac{1}{V_c^2}}\right) \tag{5.16}$$

- the maximum allowable heat flux in the stagnation point. Rewrite the heat flux equation for the density to obtain the h-V curve:

$$\rho_{qc} = \rho_0\left[R_n^{0.5}\frac{Q_{max}}{c}\left(\frac{V_c}{V}\right)\right]^2 \tag{5.17}$$

- the maximum total deceleration, or g-load. Use the following equation and the definition of the lift and drag to get a C_L and C_D and rewrite for the density:

$$n_g = \frac{\sqrt{D^2 + L^2}}{mg_0} \tag{5.18}$$

$$\rho_g = 2 \cdot n_{g,max}\frac{mg_0}{V^2S\sqrt{C_D^2 + C_L^2}} \tag{5.19}$$

The density can be related with the height by the following equation:

$$h = -H_s ln\left(\frac{\rho}{\rho_0}\right) \tag{5.20}$$

with $H_s = 8000m$ represent the atmospheric density scale. The equilibrium-glide condition should be seen as the theoretical upper limit below which no flight jump will occur. The re-entry corridor in the Altitude-Velocity map for the Skylon is shown in Fig. 5.6.
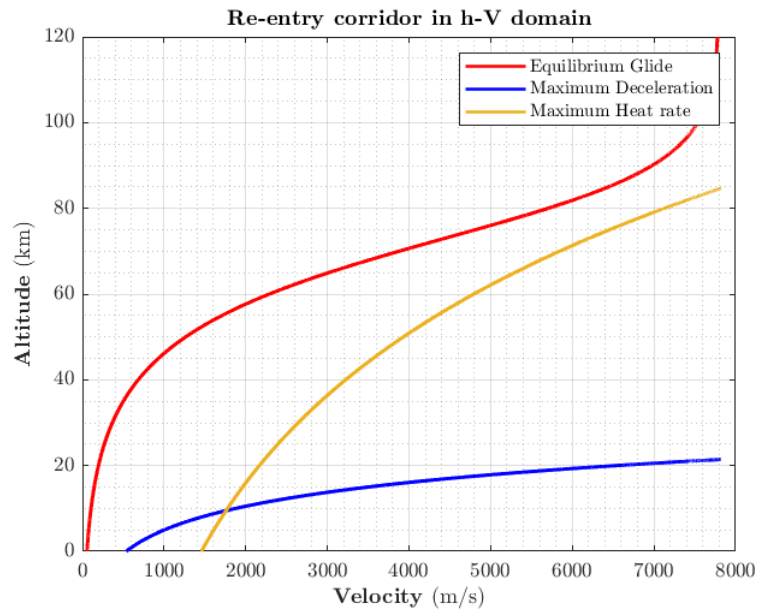
Figure 5.6: Entry corridor for the Skylon spaceplane in the h-V domain

Chapter 6

Thermal Protection Systems (TPS)

Reusable Thermal Protection System (TPS) is one of the main aspects to be concentrated as it is one of the most expensive systems of RLV. TPS should be lightweight, durable, operable and cost effective. In general, at high speeds, the temperature of the flow around the aircraft can reach thousands of Kelvins. During re-entry, these speeds are even higher and temperatures become extreme. Under these conditions, the molecules that make up the surrounding air can undergo chemical reactions. Even if only a small fraction of the initial total energy reaches the vehicle as heat, there can be a significant amount of energy to be dealt with.

It remains clear that without a thermal protection system, the aircraft cannot travel under these conditions. The TPS is developed to go to absorb or throw away the energy absorbed during reentry, and both methods can be used simultaneously. There are basically three types of TPS: heat sinks, ablation, radiative cooling.

With heat sinks, a large mass is used to "soak up" heat energy during the entry. Heat sinks are best suited to brief, high-drag entry. Ablative techniques absorb the energy and the dissipate it through the vaporizing of an expendable material. Ablative techniques are generally less massive and more practical than heat sink techniques [21]. Since the purpose of this thesis work is the design of a reusable vehicle, these types of TPS cannot be adopted since they are not reusable.

Radiative techniques have been used on the Space Shuttle Orbiter. The skin of the vehicle is allowed to absorb heat. As it heats, energy is lost through radiation. Once an equilibrium is reached, equal amounts of energy are absorbed and rejected with the surface maintaining relatively "safe" temperatures. Radiative cooling techniques are better for long, "gliding" entries where the heating rates are smaller and there is sufficient time for the surface to reach equilibrium. However, since the mission times are very long, the heat load turns out to be very important. Ablative cooling offers more flexibility in the entry profile than either of these, but sacrifices some reusability [21]. Future commercial vehicles require a TPS that is reusable, robust, and requires minimal maintenance. Ceramic tiles, such as those used in the Space Shuttle are therefore not suitable since they require about 40000 hours of work for them to be ready for a new flight. Future reusable launch vehicles will necessitate significantly enhanced thermal protection systems to attain the ambitious objective of reducing the payload delivery cost to orbit by an order of magnitude [26].

A reusable TPS must therefore withstand aerodynamic, aeroacoustic, and aerothermodynamic loads, as well as high-speed impacts such as space debris. In this thesis, we will focus only on the study of passive TPSs. An active TPS might be more efficient, but it would complicate the discussion. In addition, it would be less reliable.

6.1 TPS concepts

In this section we will briefly describe the types of TPS considered in this thesis work. Three categories of Thermal Protection Systems (TPS) are examined, based on "*Parametric Weight Comparison of Advanced Metallic, Ceramic Tile, and Ceramic Blanket Thermal Protection Systems*" by David E. Myers, Carl J. Martin, and Max L. Blosser. These are: metallic panels, rigid ceramic tiles, and flexible ceramic blankets.

Flexible ceramic blankets

Flexible ceramic blanktes are constructed with fibrous insulation between outer layers of woven ceramic fabric. The outer fabric layer is coated for stiffness and strength, and the blankets are bonded to the structure with a layer of room temperature vulcanizing (RTV) adhesive. Blankets are very inexpensive and easy to apply. Examples of this type of TPS is the Advanced Flexible Reusable Surface Insulation (AFRSI) and Tailorable Advanced Blanket Insulation (TABI) [10].

Advanced Flexible Reusable Surface Insulation

The AFRSI was used on the Space Shuttle Orbiter. However, this type of thermal protection requires waterproofing after each flight which results in increased cost and maintenance. Blankets are flexible, but when exposed to high temperatures, the outer fabric becomes easy to damage. A very important issue is the AFRSI roughness that promotes turbulence and thus increases aerodynamic heating and drag. It possesses a maximum operational temperature of 922 K. The AFRSI concept is composed of an outer fabric with C-9 coating, Q-fiber felt insulation, and an inner fabric layer, and it is attached to the structure with RTV adhesive (Fig. 6.1)
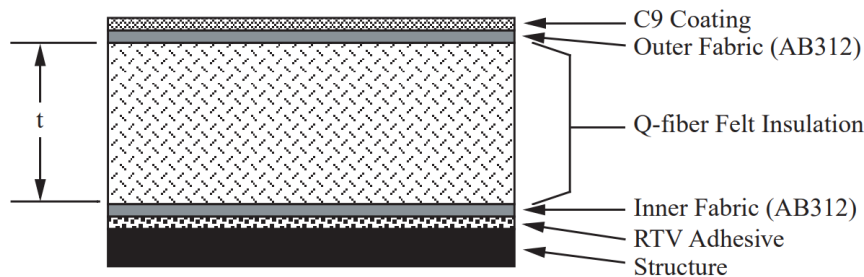
Figure 6.1: AFRSI thermal protection system [10]

Tailorable Advanced Blanket Insulation

Tailorable Advanced Blanket Insulation was developed by the NASA Ames Research Center as an improvement to the AFRSI currently certified on the Space Shuttle orbiter. In comparison to AFRSI, TABI's surface is smoother and it has a higher temperature resistance than AFRSI, with a maximum temperature of approximately 1500 K. The application of the TABI has been proposed to be applied in the windward zone of the vehicle. However, tests are underway to assess the durability of the TABI in this area of the aircraft. The TABI considered here is composed of an outer ceramic fabric with C-9 coating, Q-fiber felt insulation, ceramic fabric corrugations, and a fabric inner layer. It is attached to the structure with RTV adhesive (Fig. 6.2)
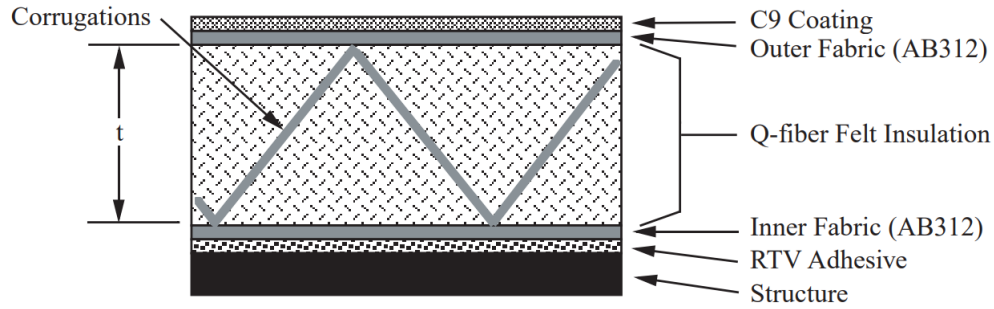
Figure 6.2: TABI thermal protection system [10]

Rigid Ceramic Tiles

Rigid ceramic insulation tiles have the ability to withstand high temperatures, which is why they were used on the Space Shuttle Orbiter in surface areas with temperatures ranging from 950 to 1800 K. Ceramic tile and blanket concepts require materials that act as a thermal insulator and also perform the structural functions of maintaining the TPS shape and resisting inertial and aerodynamic loads [26]. The usual structure of this TPS consists of a ceramic tile, a Nomex (nylon) felt strain isolation mounting pad, and RTV adhesive. The LI-900 and LI-2200 tiles are coated to improve the surface emissivity and toughness. The nature of ceramic tiles is brittle and low strength, so they should not be affected by the thermal and mechanical stresses of the underlying structure and should be insulated with a felt stress insulation pad (SIP). This limits the size of the orbiter tiles to about 25cm by 25cm. Tiles have little resistance to impact damage and require, after each flight, to be waterproofed. In addition, inspections and repairs are expensive. This was one of the reasons for the closure of the Space Shuttle program. Improved tile systems are under development which offer increased temperature capabilities and improved strength and durability.

LI-900 Tiles

The LI-900 tiles are a fibrous insulation system entirely in silica with a maximum operating temperature about 1500 K and are widely used on the Space Shuttle Orbiter. The rigid tile has a protective, emittance enhancing, and catalycity reducing coating applied to the exposed surfaces, a densified region at the attachment to improve strength, and a SIP. It is attached to the structure with RTV adhesive.
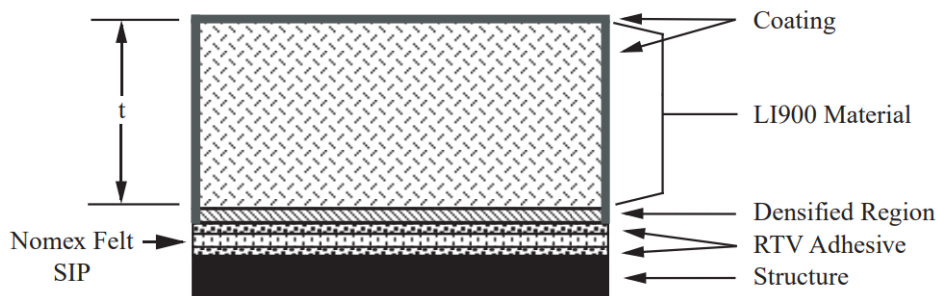
Figure 6.3: LI-900 thermal protection system[10]

Alumina Enhanced Thermal Barrier Tiles with TUFI Coating

The AETB ceramic tile with TUFI coating was developed at the NASA Ames Research Center as an improvement to the LI-900 tile. The AETB tiles demonstrate higher strength, added durability, and have a maximum operational temperature about 1650 K. The system is composed of AETB ceramic tile that is coated with TUFI and mounted on a SIP.
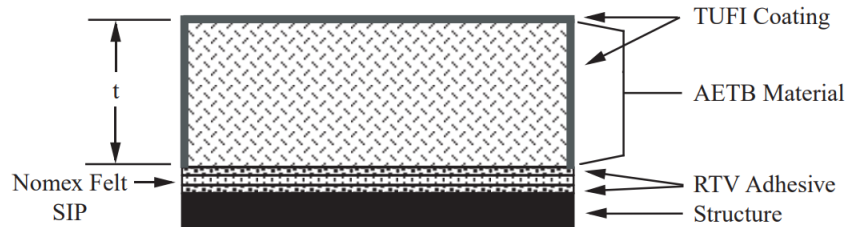

Figure 6.4: AETB thermal protection system [10]

Metallic panels

The Metallic Thermal Protection System (TPS) concept is under development at NASA Langley Research Center as an alternative to ceramic TPS. Metal TPS concepts attempt to decouple the thermal and structural functions by providing a metal shell to encapsulate the internal insulation, maintain the panel shape, and support the mechanical loads [26]. In this study, the design of the metallic TPS concept features a thin metallic box enclosing lightweight fibrous ceramic insulation. The use of low-density, efficient fibrous insulation helps reduce the weight of the metallic box. This box is supported by an edge support system made of RTV and Nomex felt to prevent any flow from beneath the panels and is attached to the structure using mechanical fasteners. The outer face of the box is constructed of a honeycomb sandwich to enhance load carrying capability and durability. High temperature superalloys are used in the hottest regions, and titanium alloys are used in lower temperature applications to reduce weight. Metallic materials are ductile, potentially allowing for a more robust TPS and making the design easier to modify. Moreover, maintenance of these types of TPS is much easier and waterproofing is not necessary because of its encapsulated nature. However, metallic TPS panels do not have the long flying history of tiles and ceilings, and the initial cost is likely to be high because of the equipment needed. Special design features may also be required to accommodate mechanical fasteners in the spacecraft structure. The following are some examples of metallic TPS [10].

Titanium Multiwall Thermal Protection System
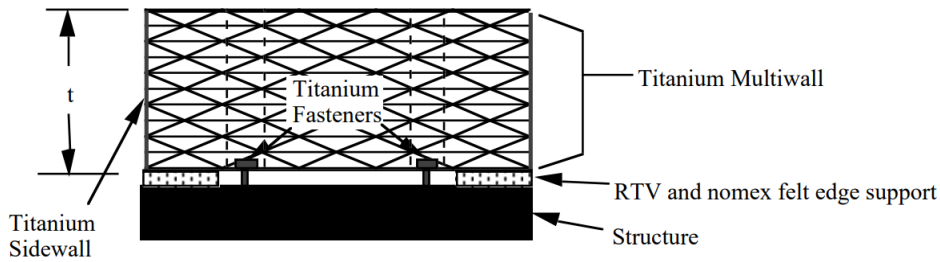
Figure 6.5: TIMW thermal protection system

Superalloy Honeycomb Metallic TPS

The SA/HC metal TPS incorporates lightweight insulation between two metal honeycomb panels. The inner sandwich panel is made of titanium, and the system has a maximum operating temperature of about 1400 K.
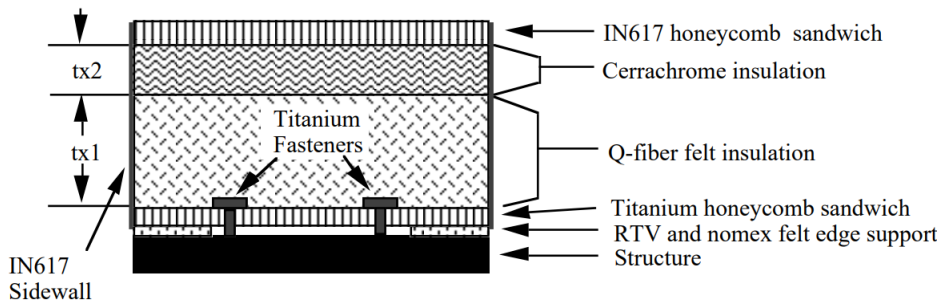

Figure 6.6: SA/HC thermal protection system

Second Generation Superalloy Honeycomb Metallic TPS

As an improvement to the Superalloy Honeycomb system, the second generation Superalloy Honeycomb Metal TPS (SA/HC2) was developed. The design of the SA/HC2 system is similar to the SA/HC, but incorporates a lighter, higher temperature insulator (Saffil). The structural weight has been reduced by replacing the 22.8 cm x 22.8 cm center section of the lower titanium sandwich with a thin aluminum foil. This TPS have a predicted maximum operational temperature of 1400K.
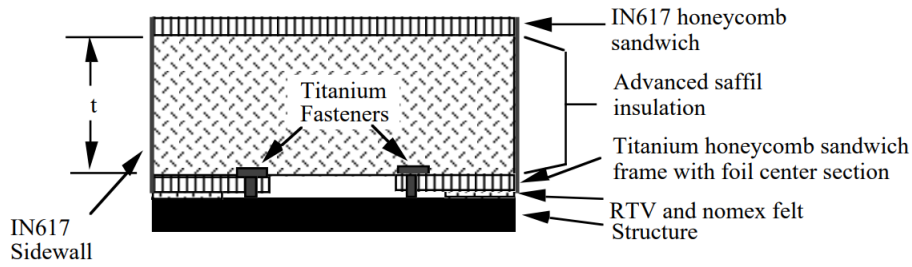
Figure 6.7: SA/HC2 thermal protection system

Titanium Honeycomb Metallic TPS

This type of TPS was developed to achieve weight savings and to be applied in those cases where operating temperatures are lower. Indeed, the system has a maximum operational temperature about 1000K.
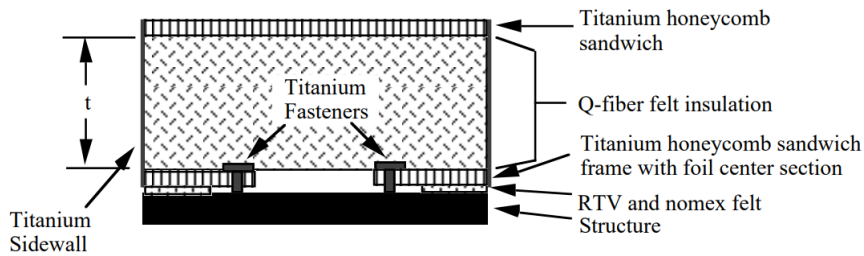
Figure 6.8: TI/HC thermal protection system

Advanced Metallic Honeycomb TPS

As an improvement to the metallic honeycomb superalloy system, the Advanced Metallic Honeycomb (AMHC) thermal protection system has been proposed to NASA's LaRC. Between an outer honeycomb sandwich and a thin sheet of titanium on the underside, there is an advanced, low-conductivity, multilayer internal insulation (MLI). A boxed frame running along the outer edges is attached to the bottom front plate. The frame and bottom front configuration replaces the honeycomb sandwich to reduce structural weight. This TPS has the potential to increase the maximum operational temperature to 1500K and has a lower density.
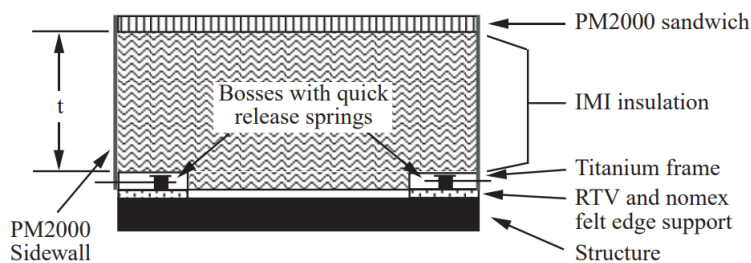
Figure 6.9: SA/HC thermal protection system

6.2 Aerothermodynamic and TPS design

In this section, wall temperatures, thermal fluxes, and thermal loads to which an SSTO vehicle is subjected during the glide re-entry phase are calculated. Aerothermodynamic is an important aspect in the design of a TPS. During atmospheric descent, the vehicle, traveling at very high speeds, is decelerated by aerodynamic drag so, this leads to high values of kinetic energy.

$$E_K = \frac{1}{2}mV^2 \tag{6.1}$$

Due to aerodynamic drag and friction between the vehicle skin and the atmosphere, the vehicle decelerates and the kinetic energy is converted to heat. This leads to intense heating and pressurizing of the atmospheric gases passing in front of the spacecraft. With temperatures around the vehicle in the thousands of Kelvin, convective and radiative heat transfer to the spacecraft is significant [6]. In this work, it is assumed that the temperature increase occurs solely due to aerodynamic heating and it is considered only the convective component of heat transfer, since the radiative component is very small. For TPS sizing, the heat flux and the heat load must first be known. The former is used to calculate the wall temperature reached by the TPS, while the latter is used to obtain the thickness. For a lifting re-entry, where the trajectory can be controlled by aerodynamic surfaces, the heat flux is much lower than for a ballistic re-entry. However, the heat load (obtained by integrating the heat flux over time) is very high due to the longer flight time and range.

For the calculation of convective heat rate, simple correlations can be developed based on simplifications of the stagnation flow analysis. In the literature, there are engineering formulations that correlate heat flux with velocity and altitude. In this case, the empirical Detra-Kemp-Riddel formula was used [9].

$$\dot{Q}_{max} = K \cdot \sqrt{\frac{1}{R_N}} \cdot \left(\frac{\rho}{\rho_0}\right)^{0.5} \cdot \left(\frac{V}{V_{sat}}\right)^{3.15} [\text{W/cm}^2] \tag{6.2}$$

with $K = 11'030$. This formula evaluates only the convective heat flux, since the radiative term can be neglected since it becomes significant at velocities above 9 km/s which are higher than the entry velocities considered in this thesis. Knowing the value of the heat flux, the heat load can be calculated as follow:

$$Q = \int_0^t \dot{Q}_{max} dt \tag{6.3}$$

with $Q\,[\text{J/m}^2]$ the total heat load and t the time mission. It is worth noting that the heat transfer rate depends only on the free flow parameter and the radius of the stagnation point, R_N. This is a very interesting result considering that once the re-entry trajectory is known in the altitude-velocity map, one can directly find the expected heat flux at the vehicle stagnation point during re-entry [6]. For preliminary evaluations, a radius sphere value of 0.3048 m was considered. Knowing the trends of atmospheric density ρ and velocity V along the trajectory, the trends for the heat flux at the stagnation point and the respective heat load are shown in Fig. 6.10.

(a) Heat transfer as a function of altitude


(b) Heat load as a function of altitude
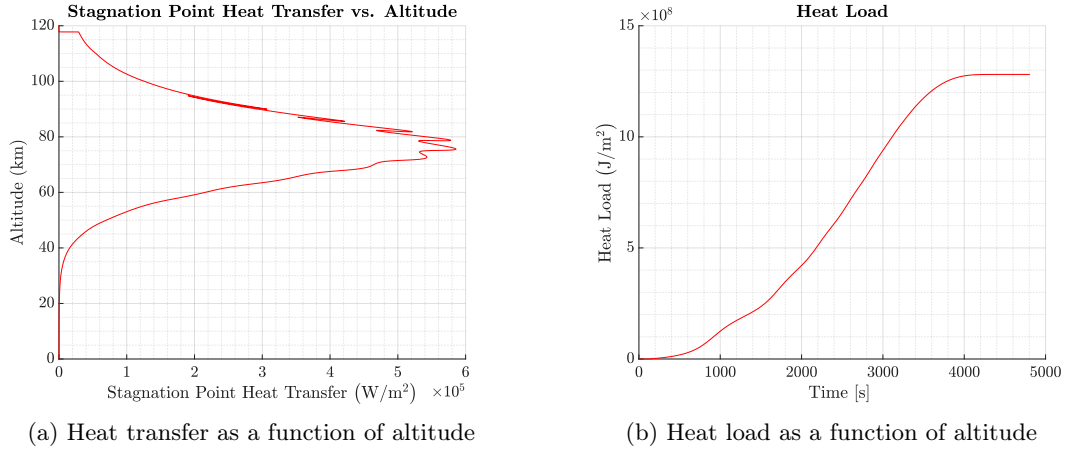
Figure 6.10: Heat transfer and heat load of Skylon

6.2.1 Temperature at wall

For the calculation of the Skylon wall temperature, the Finite Differences Method (FDM) method was used. Specifically, a 1D model has been considered (Fig. 6.11a) in which we have the wall insulated from the external environment with a certain material thickness t.

Some assumptions have been made:

- No internal heat generation.
- No variations along y direction. Temperature varies only in x direcction.
- Adiabatic inner surface: temperature at the backend of the TPS is same as that of the base material.
- Thermal properties are constant as temperature changes.
- Only the convective component of the incident flux is considered.
- Heat due to possible chemical reactions in the flow around the vehicle is not considered

We use finite difference discretization by discretizing the thickness t of the TPS into N_x nodes (Fig. 6.11b), where N_x is the number of nodes along the spatial coordinate x. Denote by i the coordinate representing the nodes along the thickness t, with $1 \leq i \leq N_x$. Consider the node at the external surface with $i = 1$ (corresponding to x=0). For the temperature calculation, the balance between the convective heat flux from the outside and the radiative flux was considered. The governing equation is:

$$\rho c_p \frac{\partial T}{\partial t} = k \frac{\partial^2 T}{\partial x^2} \tag{6.4}$$

with ρ the density of material of the TPS, c_p J/kgK the specific heat, and k W/mK the thermal conductivity.

To generate a finite difference method we use the centered difference formula for the second derivative in space [27]:

$$\frac{\partial^2 T}{\partial x^2} = \frac{T_{i+1} - 2T_i + T_{i-1}}{dx^2} \tag{6.5}$$

with i being an index ranging from 2 to $N_x - 1$. An explicit finite difference method was used for the derivative over time. The partial derivative of temperature with respect to time is approximated using forward finite differences. Suppose T_i^n represents the temperature at spatial point i and time n, so:

$$\frac{\partial T}{\partial t} = \frac{T_i^{n+1} - T_i^n}{dt} \tag{6.6}$$

58

(a) Simplified thermal model of TPS sizing [10]

(b) FD thermal model of TPS
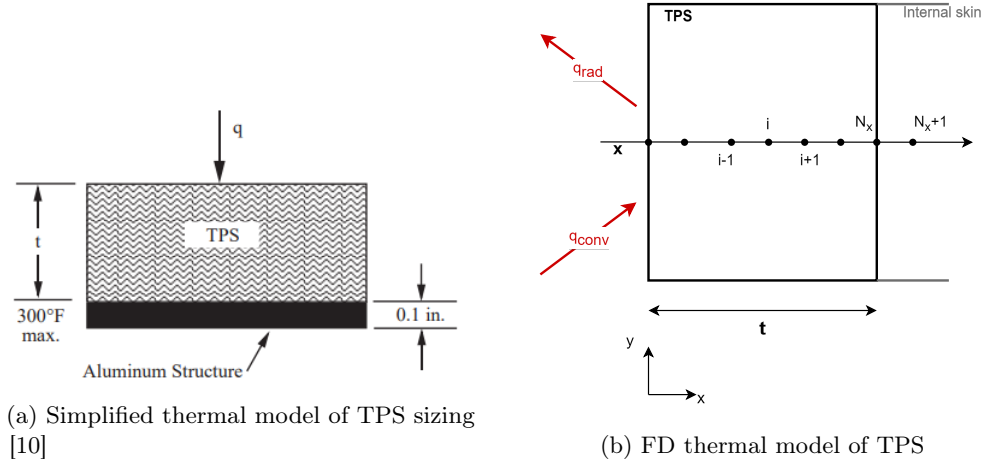
Figure 6.11: Simplified thermal model for the case study

By substituting the expressions of the derivatives in space and time in Eq. 6.4, we obtain the following equation:

$$\frac{\partial T}{\partial t} = \frac{T_i^{n+1} - T_i^n}{dt} = \alpha \frac{\partial^2 T}{\partial x^2} = \alpha \frac{T_{i+1} - 2T_i + T_{i-1}}{dx^2} \tag{6.7}$$

Solving for T_i^{n+1}:

$$T_i^{n+1} = T_i^n + \alpha \frac{dt}{dx^2}(T_{i+1} - 2T_i + T_{i-1}) \tag{6.8}$$

with $\alpha = k/\rho c_p$ the thermal diffusion coefficient (m^2/s). This equation is valid for internal nodes. To solve the problem, appropriate boundary conditions must first be chosen.

Boundary Condition - Outer Surface (x=0)

The boundary condition on the outer surface includes an incoming convective heat flux and an outgoing radiative flux and the conductive heat exchanged between adjacent cells:

$$k\frac{T(2,n) - T(1,n)}{\Delta x} - \epsilon\sigma T(1,n)^4 + q_{conv} = \rho c_p \frac{\Delta x}{2}\frac{T(1,n+1) - T(1,n)}{\Delta t} \tag{6.9}$$

Solving for the temperature $T(1, n+1)$, the boundary condition for the external surface is:

$$T(1,n+1) = T(1,n) + \frac{2\Delta t}{\rho c_p \Delta x}\left(q_{conv} + k\frac{T(2,n) - T(1,n)}{\Delta x} - \epsilon\sigma T(1,n)^4\right) \tag{6.10}$$

Boundary Condition - Inner Surface (x=t)

The boundary condition at the inner surface can be obtained by substituing $i = N_x$.

$$T(N_x, n+1) = \frac{\alpha dt}{dx^2}\left[T(N_x - 1, n) - 2T(N_x, n) + T(N_x + 1, n)\right] + T(N_x, n) \tag{6.11}$$

The temperature T_{n+1} is the temperature at the node of the internal skin of the vehicle, considered as an adiabatic wall, so:

$$T(N_x, n) = T(N_x + 1, n)$$

So, the boundary condition at the inner surface is:

$$T(N_x, n+1) = \frac{\alpha dt}{dx^2}\left[T(N_x - 1, n) - T(N_x, n)\right] + T(N_x, n) \tag{6.12}$$

The TPS material considered in this case was the AETB with TUFI coating, whose values are grouped

59

Properties of AETB/TUFI	
Density	$8.01 \cdot 10^2 \, \text{kg/m}^3$
Specific Heat	$7.95 \cdot 10^2 \, \text{J/kgK}$
Emissivity	0.873
Thermal Conductivity	$6.84 \cdot 10^{-2} \, \text{W/mK}$
Temperature Limit	1870 K

Table 6.1: Properties at standard conditions for AETB/TUFI coating [4]
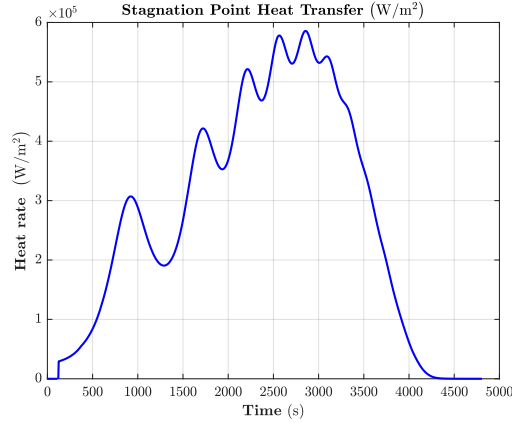
Figure 6.12: Convective stagnation point heat transfer over time for the Skylon spaceplane

in Tab. 6.1, used as input. Considering the convective heat rate in Fig. 6.12 and running a simulation using the MATLAB script in App.A, with an initial temperature of 300 K, the graphs in Fig.6.13 are obtained.
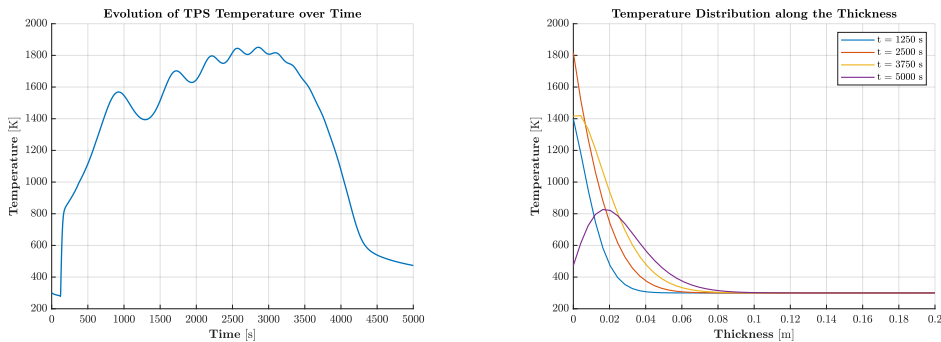
(a) Temperature distribution of external surface over time

(b) Temperature distribution along the thickness at different times

Figure 6.13: Temperature distributions for the Skylon spaceplane

It can be seen that the temperature remains below the maximum temperature limit of 1870 K. In addition, the temperature variation along the thickness at different times can be observed, Fig. 6.13. It can be seen that the temperature of the inner wall of the TPS remains at about 300 K, assuming an adiabatic wall. Considering the density of the material considered for the calculation and a thickness of 20 cm, a weight of $25.60 \, \text{kg/m}^2$ was obtained. However, this is a very approximate calculation, since in reality the vehicle is made up of a selection of different materials along its surface, as each part of it is characterized by different heat flows. However, at this level of design, the result obtained is acceptable for understanding the amount of heat the aircraft is subjected to.

Chapter 7

Mission Analysis

This chapter presents the mission simulation carried out on the commercial software ASTOS[1]. ASTOS software is a simulation and optimization environment to compute optimal trajectories for a variety of complex multi-phase optimal control problems. It has been developed for the last 20 years and is a reference tool for space trajectory optimisation at ESA/ESTEC. It consists of fast and powerful optimization programs that handle large and highly discretised problems, a user interface with multiple plot capability [28]. In ASTOS, the trajectory is divided into several phases, allowing the definition of intermediate boundary conditions.

The mission analysis presented aim to verify the consistency of data obtained from the developed design methodology. Specifically, the methodology is applied to the case study, and for the mission analysis using ASTOS, the masses (empty mass) obtained from the sizing code [3] developed were incorporated. The results are then verified and compared for the case study. As stated in Chapter 2, the applied case study is the SKYLON spaceplane, currently under development by the British company Reaction Engines Limited. In the scheme of Fig. 7.1 is presented the mission analysis procedure through ASTOS.
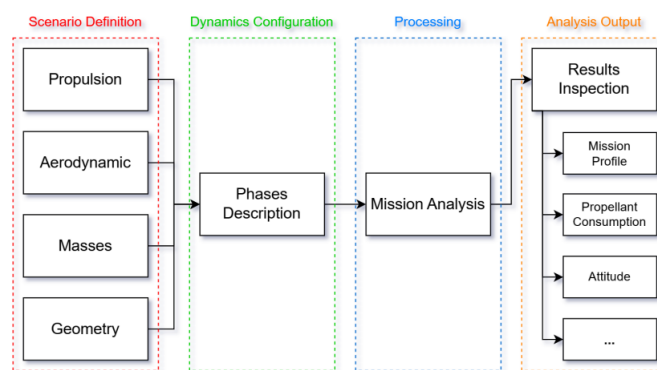
Figure 7.1: Scheme of mission analysis procedure in ASTOS [11]

---

[1]ASTOS: Aerospace Trajectory Optimization Software

7.1 Work Validation

The following section reports results for the Space Shuttle Orbiter and the X38 aircraft as a references to validate the work done in this thesis, which will be used for the mission analysis of the Skylon spaceplane.

7.1.1 Space Shuttle Orbiter

The Space Shuttle represents a semi-reusable system for the transportation of payloads and humans into various LEOs. he descent phase begins with de-orbiting through the orbital maneuvering system. Afterwards, the re-entry in Earth's atmosphere and finally landing horizontally on the runway. More information regarding the Orbiter can be found in Chapter 3. The results will be reported in the American system to compare the results with those from the literature [24].

Figure 7.2: Space Shuttle Orbiter Endeavour

Initial conditions	
Altitude	76.2 km
Velocity	7.01 km/s
Flight path angle	0.1°
Latitude	45°
Longitude	8°
Heading	0°

Figure 7.3: Initial conditions at re-entry interface for the Orbiter
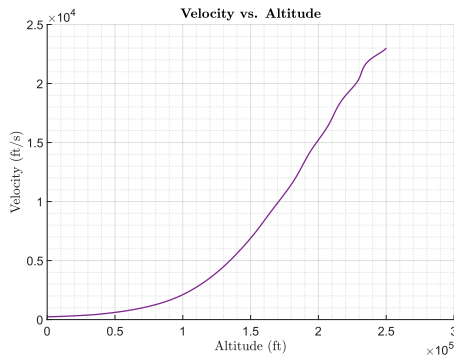
(a) Thesis results
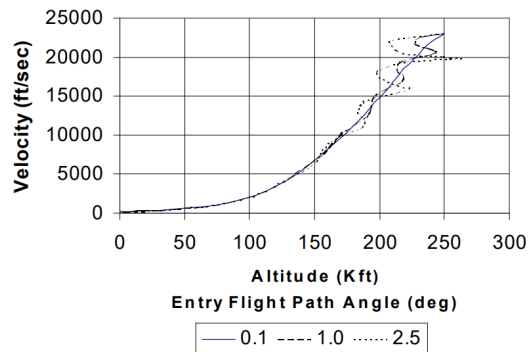
(b) Data from literature [24]

Figure 7.4: Velocity as a function of altitude for the Orbiter

(a) Thesis results

(b) Data from literature [24]
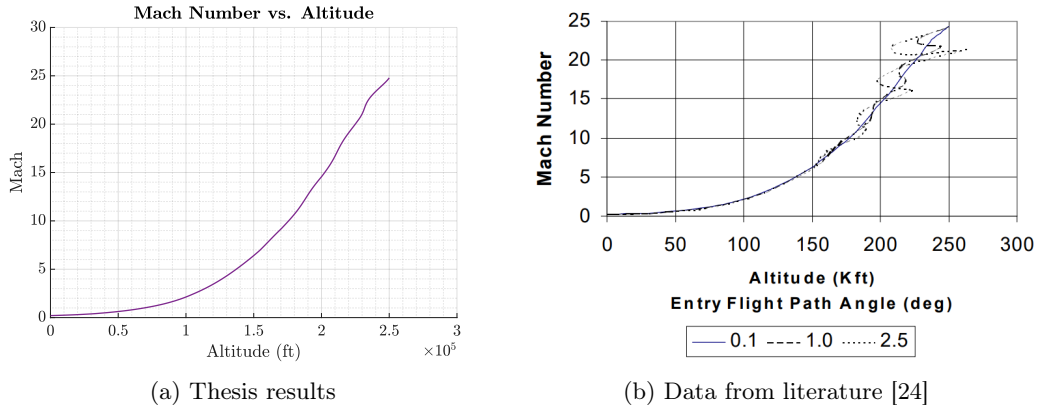
Figure 7.5: Mach as a function of altitude for the Orbiter

(a) Thesis results

(b) Data from literature [24]
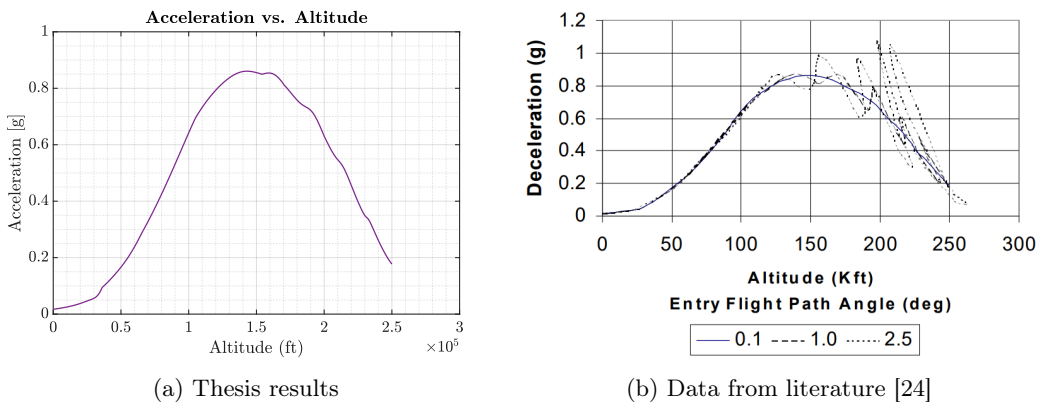
Figure 7.6: Deceleration as a function of altitude for the Orbiter

(a) Altitude as a function of velocity

(b) Altitude as a function of flight time
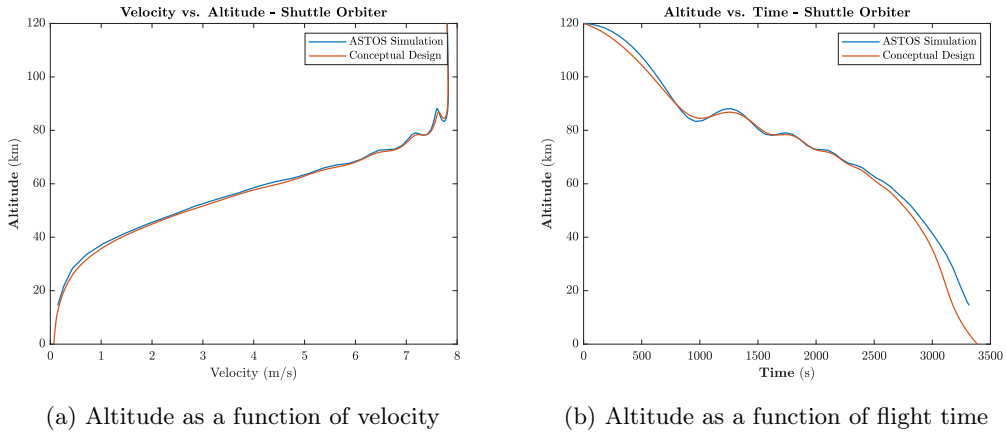
Figure 7.7: Space Shuttle Orbiter Mission Analysis trough ASTOS
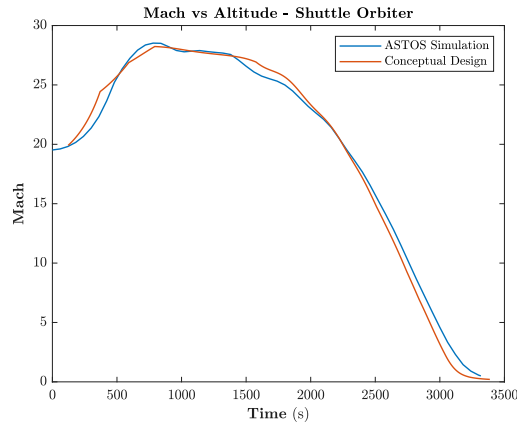
Figure 7.8: Mach as a function of flight time for the Orbiter

7.1.2 X38

The X38 was a re- entry vehicle developed in 1990. The X38, after the de-orbit boost, would re-enter the Earth's atmosphere through a un-powered gliding trajectory, behaving as a winged aircraft. More information regarding the X38 vehicle can be found in Chapter 3.

Figure 7.9: X38 vehicle

Initial conditions	
Altitude	120 km
Velocity	7.8 km/s
Flight path angle	0.1°
Latitude	45°
Longitude	8°
Heading	0°

Figure 7.10: Initial conditions at re-entry interface for the X38
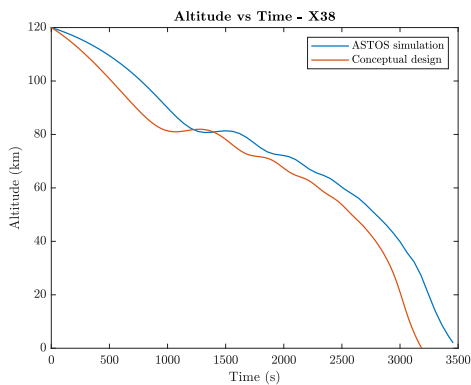
(a) Altitude as a function of flight time
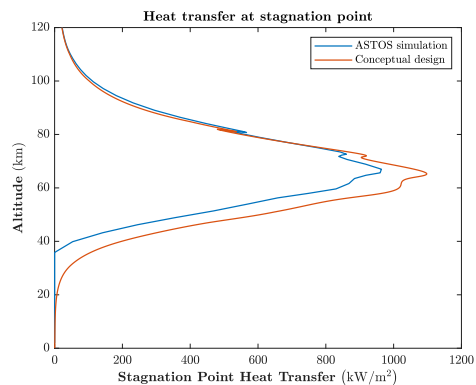
(b) Convective stagnation point heat transfer

Figure 7.14: Mission analysis for the X38 trough ASTOS

It is seen that the results obtained for both aircraft, Space Shuttle Orbiter and X38, are faithful to those found in the literature. However, for X38, the only difference lies in the mission time, which, in
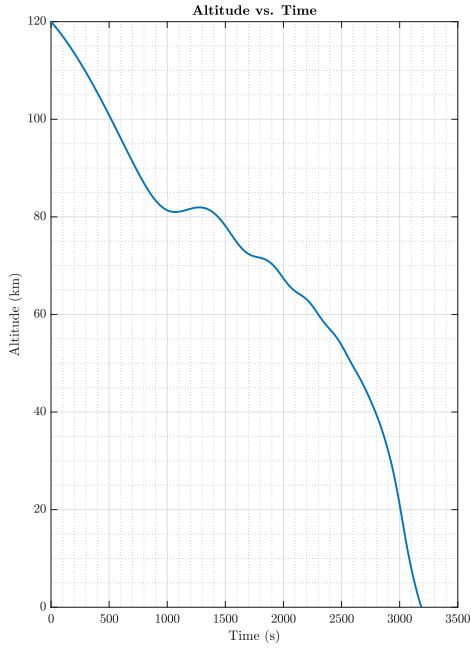
(a) Thesis results
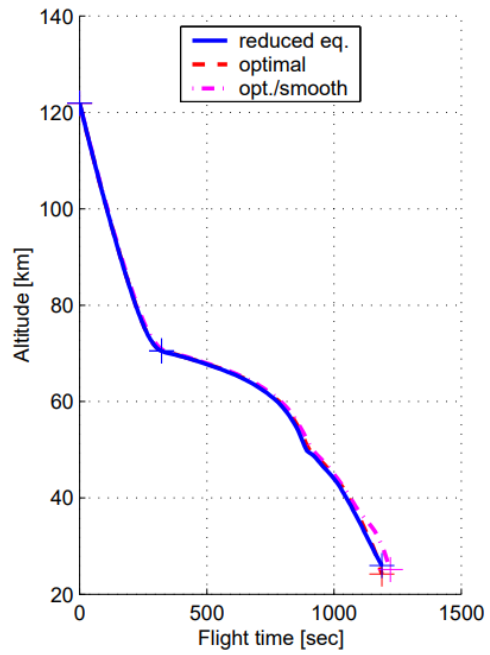
(b) Data from literature [29]

Figure 7.11: Altitude as a function of time for the X38
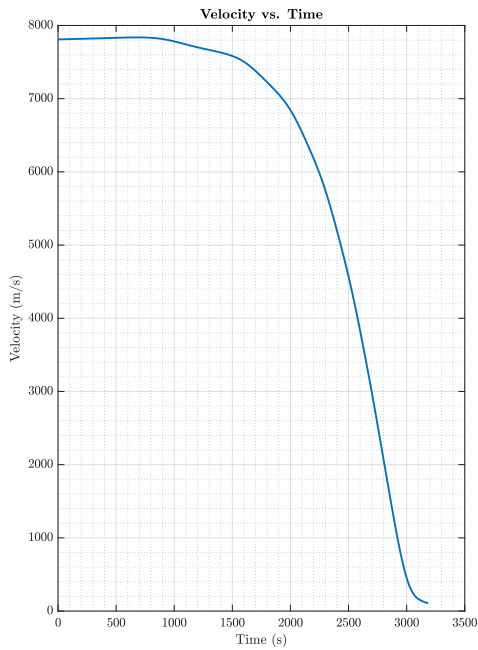
(a) Thesis results
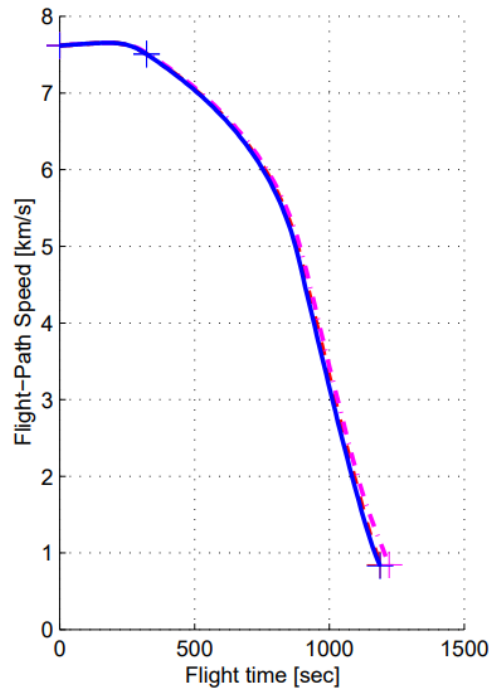
(b) Data from literature [29]

Figure 7.12: Velocity as a function of time for the X38

the case of the MATLAB code created in this thesis, turns out to be dilated. This may be due to the fact that the literature data found for X38 and reported in this thesis, are results obtained by optimization methods and for choose of the initial conditions. However, the results are faithful to

65

(a) Altitude as a function of velocity   (b) Mach as a function of flight time
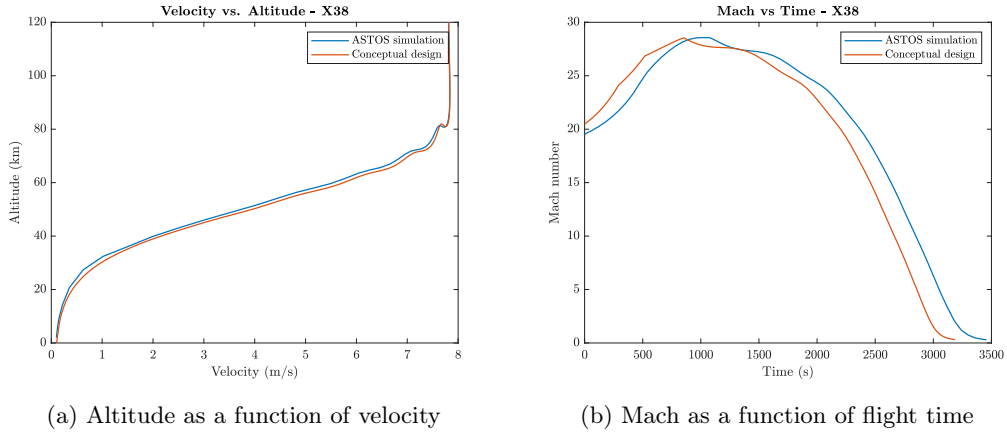
Figure 7.13: Mission analysis for the X38 trough ASTOS

(a) Thesis results   (b) Data from literature [29]
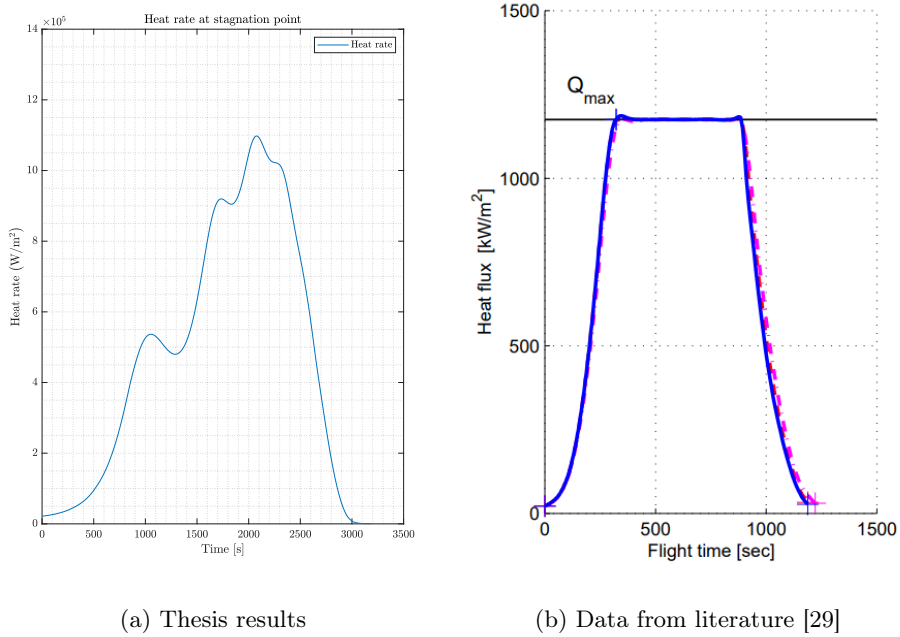
Figure 7.15: Stagnation point heat transfer for the X38

what was found in the literature.

7.2   Skylon: Mission Analysis

A typical mission profile for the Skylon aircraft in ASTOS will be defined in this section. According to the diagram in Fig. 7.1 , the scenario will be created by going to the characterization of the different disciplines. In particular, since it is a unpowered re-entry, no propulsion database will be loaded. After defining the environment and selecting US Standard 76 as the atmosphere, the aerodynamics were characterized. The data are derived from Computational Fluid Dynamics (CFD) analyses conducted on a scale model of a vehicle similar to the SKYLON at the Politecnico di Torino under the MORE&LESS project. The aerodynamic data entered in ASTOS define the lift and drag coefficients of SKYLON as a function of flight Mach number and angle of attack α. For the calculation of the aerodynamics coefficients, a reference area of $382\,\mathrm{m}^2$ and a length of 83.1 m were used. Moreover, a winged-body configuration was used for the Skylon geometry through ASTOS. SKYLON is modeled with a parallelepiped-shaped components, representing the structure of the spaceplane.

Mission phase definition in ASTOS is a task of considerable importance because it defines the dynamic configuration of the mission. Through the phase definition, ASTOS is able to find out which aerodynamic database is to be used for a flight phase. In addition, the control of the aircraft can be defined. In our case a fixed angle of attack of 30° and a zero bank angle was selected. In reality this is certainly not true. Angle of attack and bank change along the re-entry trajectory. However, at this stage of the design, this is not very binding, since it is a phase in which the purpose is to study the feasibility of a mission re-entry with an SSTO vehicle.

The re-entry phase was modeled considering the following input data (Tab. 7.2). An altitude of 120 km was considered, which is a typical literature value for atmospheric entry. For the flight path angle, having made the assumption of a gliding reentry and therefore very small angles, a very low value was chosen and equal to 0.1°. To stop the simulation, a suitable end condition must be chosen. Specifically, the end condition was chosen when the aircraft reaches a speed of Mach 0.8, which corresponds to an altitude of 24 km.

Initial conditions	
Altitude	$120\,\mathrm{km}$
Velocity	$7.8\,\mathrm{km/s}$
Flight path angle	$0.1°$
Latitude	$45°$
Longitude	$8°$
Heading	$0°$

Table 7.1: Initial conditions at re-entry interface

Input data	
Re-entry weight	55648 kg
S_{pln}	$382\ m^2$
C_D	0.5
L/D	1.5
β	$2.9 \cdot 10^3$ Pa

Table 7.2: Input data [3]

Table 7.3: Initial conditions at re-entry interface for the Skylon spaceplane

7.3   Skylon Results

Once the scenario is created, the mission simulation can begin and, if it is correct, the mission results can be displayed on ASTOS. In order to validate the methodology developed in this thesis, the results obtained on ASTOS are compared with those obtained in this work, through integration of the equations of motion by the fourth-order method of Runge Kutta, as explained in Chapter 4. This comparative analysis aims to validate the accuracy and reliability of the conceptual design approach.
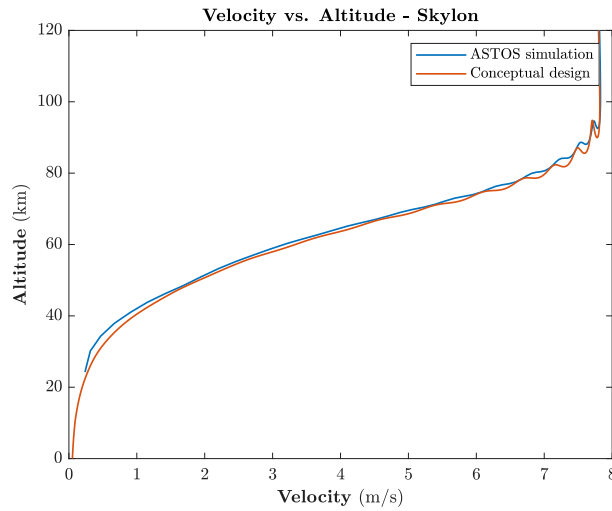
Figure 7.16: Mission profile for the Skylon spaceplane
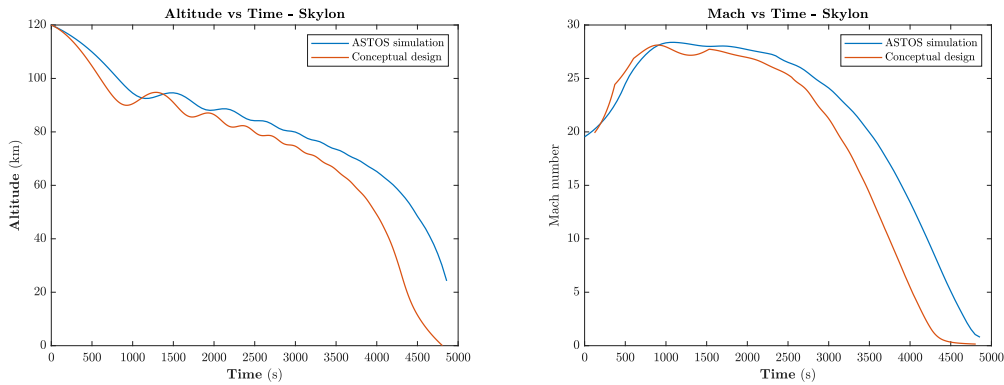
Figure 7.17: Altitude and Mach as a function of mission time for the Skylon spaceplane

In the graph of altitude as a function of velocity, in Fig. 7.16, it can be concluded that the results of the methodology present in this thesis work is faithful to the results from ASTOS. The same statement does not apply to the results in Fig. 7.17 In fact, it can be seen that the values of Mach and altitude during the mission time diverge quite a bit at low altitudes. However, the trends and values are very similar and the error, considering that we are in a conceptual design phase, seems to be small and acceptable. In addition, the trajectories obtained from the MATLAB code in Fig. 7.17 turn out to be very faithful to those in the Skylon user manual [1], given in Chapter 2.

(a) Convective Heat rate at stagnation point

(b) Velocity during mission time
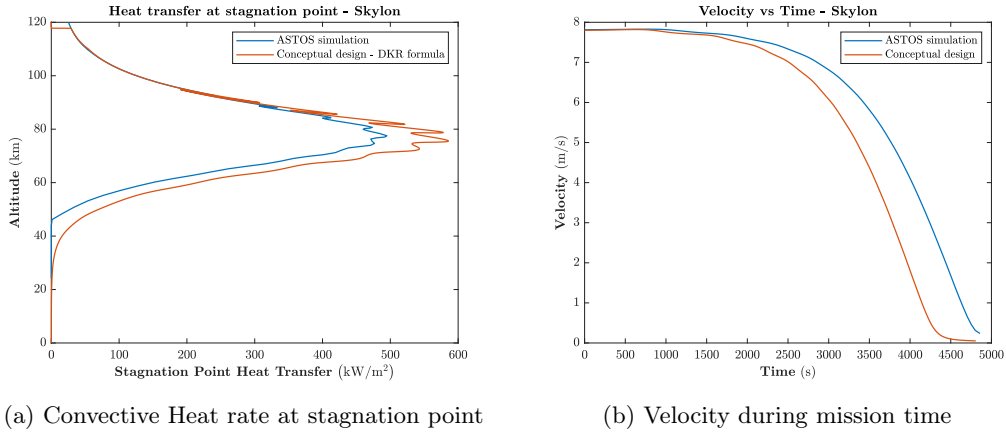
Figure 7.18: Heat rate at stagnation point and velocity for the Skylon spaceplane
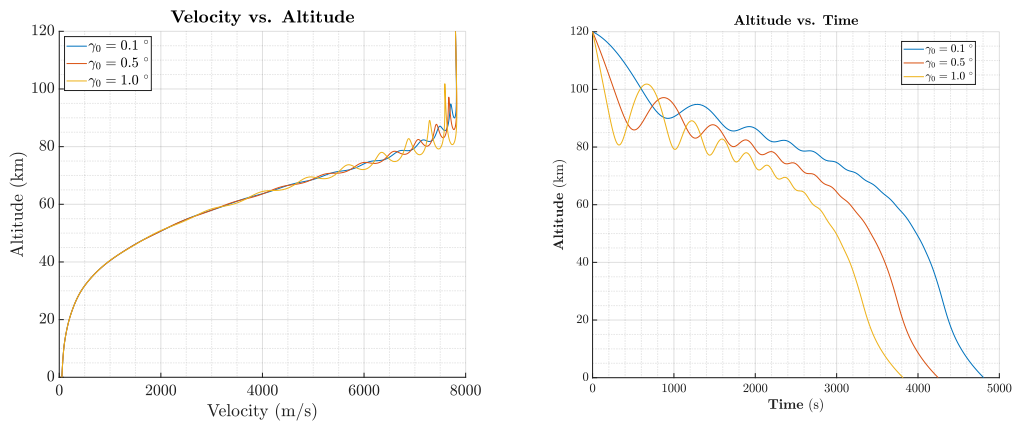
Figure 7.19: Altitude as a function of time and velocity for various values of γ_0

Other quantities are depicted in Fig. 7.18. In particular, it is seen that the convective heat flux at the stagnation point is very similar in both cases. However, they differ slightly since, for heat flux calculation, ASTOS uses the Fay-Riddel formula while the Detra-Kemp-Riddel formula was used in this thesis work. Recall that for feasibility study calculations, there are several engineering formulas for heat rate in the literature. The flux values for each formula differ slightly in the choice of constants and the use of assumptions made upstream of them. However, these formulas are very useful for first-approximation calculations. If more accurate and deeper analysis is desired, CFD analysis must be relied upon.

However, some fluctuations can be observed in the graphs. These oscillations arise from assuming a small flight path angle. Atmospheric re-entry, especially at high L/D values, is highly sensitive to variations in the flight path angle. Entering with higher flight path angle values can lead to larger oscillations at high altitudes along the entry trajectory, as can be seen in Fig. 7.19. In extreme cases, these oscillations could cause the vehicle to rebound and return to space [24].

As mentioned in Chapter 5, the value of the input flight path angle also affects the heat flux and dynamic pressure, as depicted in Fig. 7.20. However, as already mentioned in Chapter 4, a glide re-entry was assumed in this work, in which the fligh path angle is small. As can be seen in the figures, for an angle of 0.1°, the oscillations are low and acceptable at this level of analysis, since the goal was to obtain the trends of the main variables involved.
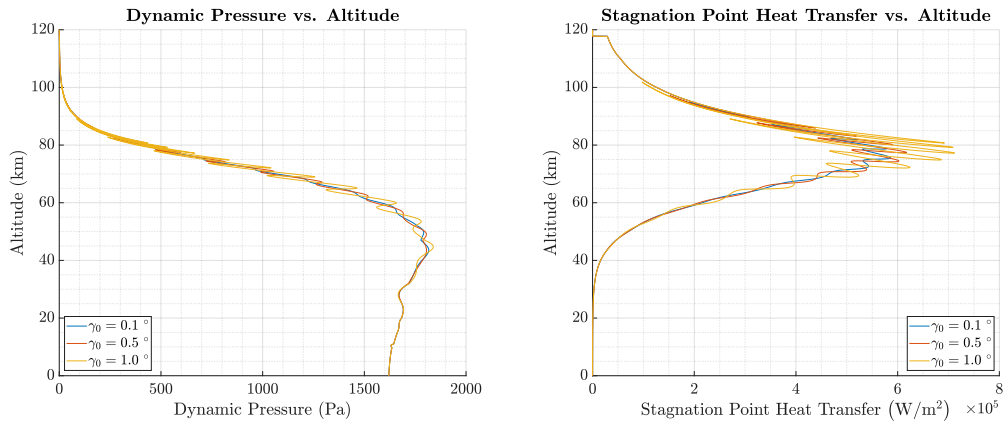
Figure 7.20: Dynamic pressure and convective heat rate as a function of altitude for various values of γ_0
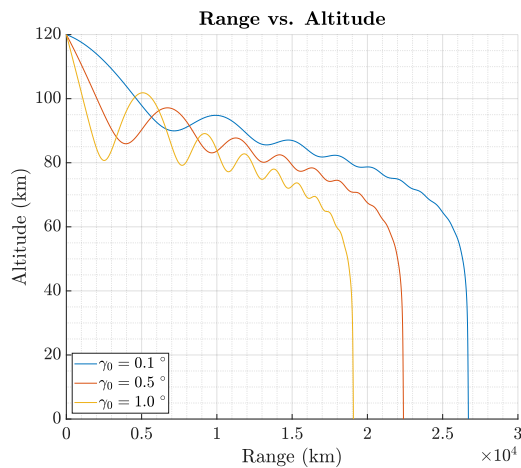
Figure 7.21: Downrange for various values of γ_0

It can be seen, from Fig. 7.21, that the value of the flight path angle also affects the downrange achieved by the Skylon. Specifically, as the flight path angle increases, the range decreases. This is plausible, since by increasing the value of the angle, the aircraft will have a steeper trajectory similar to a ballistic re-entry, penetrating the layers of the atmosphere more. In addition, the high downrange values are due to having a vehicle with a high Lift to Drag ratio (L/D). Finally, Fig.7.22 shows the evolution of the flight path angle as a function of altitude. As can be seen, the hypothesis of a small flight path angle is valid in the first moments of re-entry. However, at low altitudes, the value of the flight path angle turns out to be higher, since when the vehicle travels at low speeds, the value of the angle tends to increase and thus the assumption of small values will no longer valid.
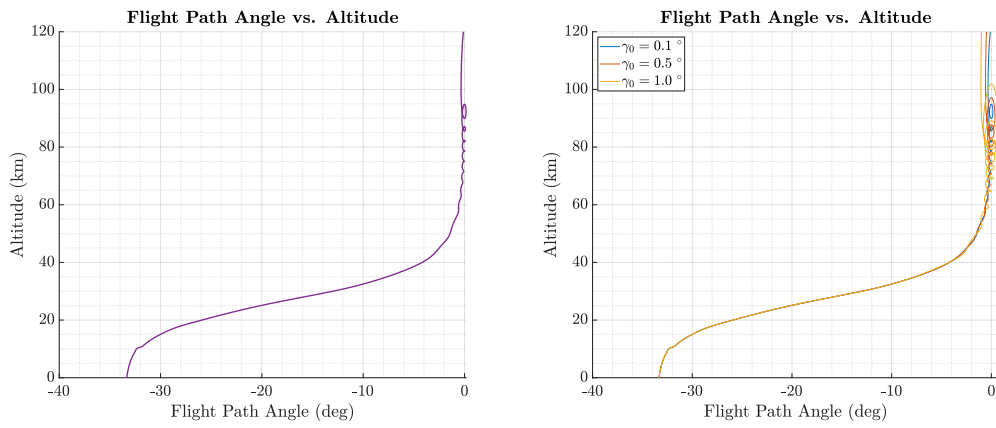
Figure 7.22: Trend of the flight path angle as a function of altitude for the Skylon spaceplane

Chapter 8

Conclusions

The purpose of this thesis was to characterize and study the atmospheric re-entry phase of a reusable SSTO vehicle during its conceptual design phase, which could allow for a very high flight frequency without the need for dedicated launch sites or integration with other stages. In particular, this methodology was applied to the case study of the Skylon, a spaceplane under developement by Reaction Engine, a British company. To achieve this, MATLAB software was used to integrate the equations of motion with some simplifying assumptions, employing the fourth-order Runge-Kutta method.

Specifically, the equations of planar motion were utilized, neglecting the Earth's rotational velocity, and a zero bank angle was chosen. Finally, the methodology implemented in this thesis was validated by performing a mission analysis on the commercial software ASTOS. After introducing the re-entry problem and conducting an overview of the main concepts developed throughout history, a literature review was performed on the aerodynamic databases developed for the most important re-entry vehicles, including the Space Shuttle Orbiter. Aerodynamic databases were reported as a function of Mach and angle of attack. Next, the equations of planar motion were reported and a model for the atmosphere was developed. In particular, the trends of temperature, pressure and density as a function of altitude were depicted.

A typical re-entry corridor for the Skylon was then developed, choosing the temperature and acceleration constraints of the vehicle during descent. In the absence of literature data for the Skylon, the values of the constraints were chosen on the basis of the trajectories obtained from the equations of motion. In addition, the corridor was developed in both a Drag-Velocity plot and an Altitude-Velocity plot. In the drag-velocity diagram, a nominal re-entry trajectory was developed for the aircraft to follow during descent, ensuring compliance with aerothermodynamic constraints.

Chapter 7 then analyzed the thermal protection system. First, a description of typical reusable TPS concepts was given. Next, a wall temperature calculation was performed knowing the convective heat flux value at the stagnation point trough a 1D finite difference model and the calculation of the temperature over time and along the thickness of the TPS was performed after selecting boundary conditions. Finally, the thesis work was validated by performing a mission analysis on ASTOS, by taking as references the X38 and Space Shuttle Orbiter. The trajectories, obtained from the code in MATLAB, were then compared with the results obtained from the simulation in ASTOS and it was found that the trajectories are very close and the validity of the methodology was confirmed.

The work developed in this thesis appears to be reliable and sufficient for the preliminary study of the re-entry phase. It can be seen from the plots that, although the entry altitude is 120 km, the effects

of the atmosphere are negligible up to heights of about 90-80 km, up to which the vehicle follows a ballistic entry.

It should be noted, however, that this code has limitations due to the simplifications made. Specifically, a bank angle of zero and an angle of attack of 30° were chosen. In addition, no control law was implemented. However, this is never going to happen, since the angle of bank is modulated in such a way that the re-entry can be controlled so that the aircraft reaches the desired runway, which is characterized by a certain latitude and longitude. In addition, MATLAB used fixed values for the lift and drag coefficients as input. In possible future work, an aerodynamic database that depends on the angle of attack and the Mach number, as seen in Chapter 3, could be used. In particular, an aerodynamic model could be constructed for basic shapes representing common re-entry vehicle configurations, for which analytical formulas are available to calculate aerodynamic coefficients based on Newton's theory.

Finally, for the re-entry dynamics discussed in Chapter 4, a more comprehensive atmospheric model could be implemented, incorporating factors such as Earth's rotation or wind contributions. Additionally, a trajectory optimization method could be employed. Instead, other critical locations than the nose of the vehicle, such as the leading edge of the wing, could be considered in the calculation of the heat exposure. For future studies, it is also possible to explore how different initial conditions, based on various deorbit trajectories, affect the re-entry paths.

However, this work proves to be very flexible and computationally fast. Indeed, by simply changing the input parameters, it can be applied to aircraft other than the Skylon like, for example, Space Shuttle Orbiter or X38. Considering that this work is part of an ambitious research project to develop a conceptual design tool for reusable spacecraft, it can be concluded that a solid foundation has been established upon which the instrument can be completed and made available to researchers, students, and engineers. However, while this analysis could be used as an effective baseline, the fidelity of the simulation could be improved.

Appendix A

MATLAB Code

```matlab
%% DIFFERENCE FINITE METHOD - SKYLON


% AETB-TUFI
rho = 8.01e2;                % Density [kg/m^3]
cp = 7.95e2;                 % Specific Heat [J/kgK]
k = 6.84e-2;                 % Thermal Conductivity [W/mK]
epsilon = 0.873;             % Emissivity  [-]


sigma = 5.67e-8;             % Stefan-Boltzmann costant [W/m^2 K^4]
T_w_initial = 422;           % Initial Temperature [K]
t_final = 5000;              % Final Time [s]
thickness = 0.2;             % Thickness   [m]

% Discretization
Nx = 50;                     % Number of spatial nodes
Nt = 5000;                   % Number of time steps
dx = thickness / (Nx-1);     % Space step
dt = t_final / (Nt-1);       % Time step

% Diffusion coefficient
alpha = k / (rho * cp);

% Initial condition
T = T_w_initial * ones(Nx, Nt);

% Interpolation of the Heat transfer
t_q_conv = t_i;
q_conv_values = HT_stagnation;

t_fine = linspace(min(t_q_conv), max(t_q_conv), 1000);
q_conv_spline = spline(t_q_conv, q_conv_values, t_fine);

q_conv = @(t) interp1(t_fine, q_conv_spline, t, 'linear', 'extrap');

% Time interval
t_interpolated = linspace(0, t_final, Nt);

% Time loop with temperature update
```

```matlab
41  for n = 1:Nt-1
42      for i = 2:Nx-1
43          T(i, n+1) = T(i, n) + alpha * dt / dx^2 * (T(i+1, n) - 2*T(i, n) + T(i-1, n));
44      end
45
46      % Updating the temperature to the external surface (x = 0)
47       q_conv_n = q_conv(t_interpolated(n));
48       rad_term = epsilon * sigma * (T(1, n)^4);
49       cond_term = k * (T(2, n) - T(1, n)) / dx;
50       T(1, n+1) = T(1, n) + (2* dt / (rho * cp * dx)) * (-rad_term + cond_term +
             q_conv_n);
51
52
53      % Temperature update at the inner surface (x = thickness) with adiabatic condition
54      T(Nx, n+1) = T(Nx, n) + alpha * dt / dx^2 * (T(Nx-1, n) - T(Nx, n));
55  end
56
57  % Display of results: Temperature as a function of thickness at different times
58  figure;
59  hold on;
60  set(groot,'defaultAxesTickLabelInterpreter','latex');
61  set(groot,'defaulttextinterpreter','latex');
62  set(groot,'defaultLegendInterpreter','latex');
63  plot(linspace(0, thickness, Nx), T(:, round(Nt*0.25)), 'DisplayName', 't = 1250 s', '
        LineWidth',1);
64  plot(linspace(0, thickness, Nx), T(:, round(Nt*0.5)), 'DisplayName', 't = 2500 s', '
        LineWidth',1);
65  plot(linspace(0, thickness, Nx), T(:, round(Nt*0.75)), 'DisplayName', 't = 3750 s', '
        LineWidth',1);
66  plot(linspace(0, thickness, Nx), T(:, end), 'DisplayName', 't = 5000 s', 'LineWidth'
        ,1);
67  xlabel('\textbf{Time} [m]', 'Interpreter', 'latex');
68  ylabel('\textbf{Temperature} [K]', 'Interpreter', 'latex');
69  title('\textbf{Temperature Distribution along the Thickness}', 'Interpreter', 'latex')
        ;
70  legend show;
71  grid on;
72
73  % Display of results: Temperature as a function of time at different thicknesses
74  figure;
75  hold on;
76  set(groot,'defaultAxesTickLabelInterpreter','latex');
77  set(groot,'defaulttextinterpreter','latex');
78  set(groot,'defaultLegendInterpreter','latex');
79  plot(t_interpolated, T(1, :), 'DisplayName', 'x = 0 m (superficie esterna)', '
        LineWidth',1.2);
80  xlabel('\textbf{Time} [s]', 'Interpreter', 'latex');
81  ylabel('\textbf{Temperature} [K]', 'Interpreter', 'latex');
82  title('\textbf{Evolution of TPS Temperature over Time}', 'Interpreter', 'latex');
83  grid on;
84
85  fprintf('Thickness :%6.2f cm\n', 100 * thickness);
86  fprintf('Weight :%6.2f kg/m^2\n', rho * thickness);
```

Listing A.1: Difference finite method for the calculation of wall temperature

Appendix B

Runge-Kutta coefficients

In this part are the coefficients of the fourth-order Runge Kutta method:

$$i_1^n = f_1(t_n, V_n, \gamma_n, \psi_n, h_n, r_n, \phi_n, \theta_n) \tag{B.1}$$

$$j_1^n = f_2(t_n, V_n, \gamma_n, \psi_n, h_n, r_n, \phi_n, \theta_n) \tag{B.2}$$

$$k_1^n = f_3(t_n, V_n, \gamma_n, \psi_n, h_n, r_n, \phi_n, \theta_n) \tag{B.3}$$

$$l_1^n = f_4(t_n, V_n, \gamma_n, \psi_n, h_n, r_n, \phi_n, \theta_n) \tag{B.4}$$

$$m_1^n = f_5(t_n, V_n, \gamma_n, \psi_n, h_n, r_n, \phi_n, \theta_n) \tag{B.5}$$

$$n_1^n = f_6(t_n, V_n, \gamma_n, \psi_n, h_n, r_n, \phi_n, \theta_n) \tag{B.6}$$

$$o_1^n = f_7(t_n, V_n, \gamma_n, \psi_n, h_n, r_n, \phi_n, \theta_n) \tag{B.7}$$

For the second step:

$$i_2^n = f_1\left(t_n + \frac{\Delta t}{2}, V_n + \frac{\Delta t}{2}i_1^n, \gamma_n + \frac{\Delta t}{2}j_1^n, \psi_n + \frac{\Delta t}{2}k_1^n, h_n + \frac{\Delta t}{2}l_1^n, r_n + \frac{\Delta t}{2}m_1^n, \phi_n + \frac{\Delta t}{2}n_1^n, \theta_n + \frac{\Delta t}{2}o_1^n\right)$$

$$j_2^n = f_2\left(t_n + \frac{\Delta t}{2}, V_n + \frac{\Delta t}{2}i_1^n, \gamma_n + \frac{\Delta t}{2}j_1^n, \psi_n + \frac{\Delta t}{2}k_1^n, h_n + \frac{\Delta t}{2}l_1^n, r_n + \frac{\Delta t}{2}m_1^n, \phi_n + \frac{\Delta t}{2}n_1^n, \theta_n + \frac{\Delta t}{2}o_1^n\right)$$

$$k_2^n = f_3\left(t_n + \frac{\Delta t}{2}, V_n + \frac{\Delta t}{2}i_1^n, \gamma_n + \frac{\Delta t}{2}j_1^n, \psi_n + \frac{\Delta t}{2}k_1^n, h_n + \frac{\Delta t}{2}l_1^n, r_n + \frac{\Delta t}{2}m_1^n, \phi_n + \frac{\Delta t}{2}n_1^n, \theta_n + \frac{\Delta t}{2}o_1^n\right)$$

$$l_2^n = f_4\left(t_n + \frac{\Delta t}{2}, V_n + \frac{\Delta t}{2}i_1^n, \gamma_n + \frac{\Delta t}{2}j_1^n, \psi_n + \frac{\Delta t}{2}k_1^n, h_n + \frac{\Delta t}{2}l_1^n, r_n + \frac{\Delta t}{2}m_1^n, \phi_n + \frac{\Delta t}{2}n_1^n, \theta_n + \frac{\Delta t}{2}o_1^n\right)$$

$$m_2^n = f_5\left(t_n + \frac{\Delta t}{2}, V_n + \frac{\Delta t}{2}i_1^n, \gamma_n + \frac{\Delta t}{2}j_1^n, \psi_n + \frac{\Delta t}{2}k_1^n, h_n + \frac{\Delta t}{2}l_1^n, r_n + \frac{\Delta t}{2}m_1^n, \phi_n + \frac{\Delta t}{2}n_1^n, \theta_n + \frac{\Delta t}{2}o_1^n\right)$$

$$n_2^n = f_6\left(t_n + \frac{\Delta t}{2}, V_n + \frac{\Delta t}{2}i_1^n, \gamma_n + \frac{\Delta t}{2}j_1^n, \psi_n + \frac{\Delta t}{2}k_1^n, h_n + \frac{\Delta t}{2}l_1^n, r_n + \frac{\Delta t}{2}m_1^n, \phi_n + \frac{\Delta t}{2}n_1^n, \theta_n + \frac{\Delta t}{2}o_1^n\right)$$

$$o_2^n = f_7\left(t_n + \frac{\Delta t}{2}, V_n + \frac{\Delta t}{2}i_1^n, \gamma_n + \frac{\Delta t}{2}j_1^n, \psi_n + \frac{\Delta t}{2}k_1^n, h_n + \frac{\Delta t}{2}l_1^n, r_n + \frac{\Delta t}{2}m_1^n, \phi_n + \frac{\Delta t}{2}n_1^n, \theta_n + \frac{\Delta t}{2}o_1^n\right)$$

For the third step:

$$i_3^n = f_1\left(t_n + \frac{\Delta t}{2}, V_n + \frac{\Delta t}{2}i_2^n, \gamma_n + \frac{\Delta t}{2}j_2^n, \psi_n + \frac{\Delta t}{2}\frac{n}{2}, h_n + \frac{\Delta t}{2}l_2^n, r_n + \frac{\Delta t}{2}m_2^n, \phi_n + \frac{\Delta t}{2}n_2^n, \theta_n + \frac{\Delta t}{2}o_2^n\right)$$

$$j_3^n = f_2\left(t_n + \frac{\Delta t}{2}, V_n + \frac{\Delta t}{2}i_2^n, \gamma_n + \frac{\Delta t}{2}j_2^n, \psi_n + \frac{\Delta t}{2}\frac{n}{2}, h_n + \frac{\Delta t}{2}l_2^n, r_n + \frac{\Delta t}{2}m_2^n, \phi_n + \frac{\Delta t}{2}n_2^n, \theta_n + \frac{\Delta t}{2}o_2^n\right)$$

$$k_3^n = f_3\left(t_n + \frac{\Delta t}{2}, V_n + \frac{\Delta t}{2}i_2^n, \gamma_n + \frac{\Delta t}{2}j_2^n, \psi_n + \frac{\Delta t}{2}\frac{{}^n}{2}, h_n + \frac{\Delta t}{2}l_2^n, r_n + \frac{\Delta t}{2}m_2^n, \phi_n + \frac{\Delta t}{2}n_2^n, \theta_n + \frac{\Delta t}{2}o_2^n\right)$$

$$l_3^n = f_4\left(t_n + \frac{\Delta t}{2}, V_n + \frac{\Delta t}{2}i_2^n, \gamma_n + \frac{\Delta t}{2}j_2^n, \psi_n + \frac{\Delta t}{2}\frac{{}^n}{2}, h_n + \frac{\Delta t}{2}l_2^n, r_n + \frac{\Delta t}{2}m_2^n, \phi_n + \frac{\Delta t}{2}n_2^n, \theta_n + \frac{\Delta t}{2}o_2^n\right)$$

$$m_3^n = f_5\left(t_n + \frac{\Delta t}{2}, V_n + \frac{\Delta t}{2}i_2^n, \gamma_n + \frac{\Delta t}{2}j_2^n, \psi_n + \frac{\Delta t}{2}\frac{{}^n}{2}, h_n + \frac{\Delta t}{2}l_2^n, r_n + \frac{\Delta t}{2}m_2^n, \phi_n + \frac{\Delta t}{2}n_2^n, \theta_n + \frac{\Delta t}{2}o_2^n\right)$$

$$n_3^n = f_6\left(t_n + \frac{\Delta t}{2}, V_n + \frac{\Delta t}{2}i_2^n, \gamma_n + \frac{\Delta t}{2}j_2^n, \psi_n + \frac{\Delta t}{2}\frac{{}^n}{2}, h_n + \frac{\Delta t}{2}l_2^n, r_n + \frac{\Delta t}{2}m_2^n, \phi_n + \frac{\Delta t}{2}n_2^n, \theta_n + \frac{\Delta t}{2}o_2^n\right)$$

$$o_3^n = f_7\left(t_n + \frac{\Delta t}{2}, V_n + \frac{\Delta t}{2}i_2^n, \gamma_n + \frac{\Delta t}{2}j_2^n, \psi_n + \frac{\Delta t}{2}\frac{{}^n}{2}, h_n + \frac{\Delta t}{2}l_2^n, r_n + \frac{\Delta t}{2}m_2^n, \phi_n + \frac{\Delta t}{2}n_2^n, \theta_n + \frac{\Delta t}{2}o_2^n\right)$$

Finally, for the fourth step:

$$i_4^n = f_1(t_n + \Delta t, V_n + i_3^n\Delta t, \gamma_n + j_3^n\Delta t, \psi_n + k_3^n\Delta t, h_n + l_3^n\Delta t, r_n + m_3^n\Delta t, \phi_n + n_3^n\Delta t, \theta + o_3^n\Delta t)$$

$$j_4^n = f_2(t_n + \Delta t, V_n + i_3^n\Delta t, \gamma_n + j_3^n\Delta t, \psi_n + k_3^n\Delta t, h_n + l_3^n\Delta t, r_n + m_3^n\Delta t, \phi_n + n_3^n\Delta t, \theta + o_3^n\Delta t)$$

$$k_4^n = f_3(t_n + \Delta t, V_n + i_3^n\Delta t, \gamma_n + j_3^n\Delta t, \psi_n + k_3^n\Delta t, h_n + l_3^n\Delta t, r_n + m_3^n\Delta t, \phi_n + n_3^n\Delta t, \theta + o_3^n\Delta t)$$

$$l_4^n = f_4(t_n + \Delta t, V_n + i_3^n\Delta t, \gamma_n + j_3^n\Delta t, \psi_n + k_3^n\Delta t, h_n + l_3^n\Delta t, r_n + m_3^n\Delta t, \phi_n + n_3^n\Delta t, \theta + o_3^n\Delta t)$$

$$m_4^n = f_5(t_n + \Delta t, V_n + i_3^n\Delta t, \gamma_n + j_3^n\Delta t, \psi_n + k_3^n\Delta t, h_n + l_3^n\Delta t, r_n + m_3^n\Delta t, \phi_n + n_3^n\Delta t, \theta + o_3^n\Delta t)$$

$$n_4^n = f_6(t_n + \Delta t, V_n + i_3^n\Delta t, \gamma_n + j_3^n\Delta t, \psi_n + k_3^n\Delta t, h_n + l_3^n\Delta t, r_n + m_3^n\Delta t, \phi_n + n_3^n\Delta t, \theta + o_3^n\Delta t)$$

$$o_4^n = f_7(t_n + \Delta t, V_n + i_3^n\Delta t, \gamma_n + j_3^n\Delta t, \psi_n + k_3^n\Delta t, h_n + l_3^n\Delta t, r_n + m_3^n\Delta t, \phi_n + n_3^n\Delta t, \theta + o_3^n\Delta t)$$

Knowing the values of these coefficients over time, the values of the variables of interest for the study of reentry can be calculated through equations in Section 4.4

Bibliography

[1] Reaction Engines. Skylon user's manual. 2014.

[2] Claus Weiland. *Aerodynamic Data of Space Vehicles.* Springer, 2014.

[3] Tommaso Molinari. *Conceptual design methodology and tool for reusable single-stage-to-orbit vehicles with horizontal take-off and landing.* PhD thesis, Politecnico di Torino, 2024.

[4] NASA Ames Research Center. TPSX: Thermal Protection System Experience. `https://tpsx.arc.nasa.gov/`, Accesso continuo. Accessed: 2024-06-27.

[5] Zita Papp. Mission planner for heating-optimal re-entry trajectories with extended range capability. Master's thesis, TU Delft University, 2014.

[6] Antonio Viviani and Giuseppe Pezzella. *Aerodynamic and aerothermodynamic analysis of space mission vehicles*, volume 898. Springer, 2015.

[7] Frank J Regan. *Dynamics of atmospheric re-entry.* Aiaa, 1993.

[8] Re-entry Motion. Returning from space: Re-entry, 2016.

[9] L.K. Pranke W.J. Larson. *Human Space Flight: Mission Analysis and Design.* McGraw-Hill College, 1999.

[10] David E. Myers, Carl J. Martin, and Max L. Blosser. Parametric weight comparison of advanced metallic, ceramic tile, and ceramic blanket thermal protection systems. *National Aeronautics Space Administration*, 2000.

[11] Roberto Cau. *Characterisation and Simulation of Reusable Single-Stage-To-Orbit Vehicles Ascent Phase during Conceptual Design.* PhD thesis, Politecnico di Torino, 2024.

[12] Y Bhavana, N Mani Shankar, and BK Prarthana. Reusable launch vehicles: Evolution redefined. *J Aeronaut Aerospace Eng*, 2(107):2, 2013.

[13] Michael A Rampino. *Concepts of operations for a reusable launch vehicle.* Air University Press, 1997.

[14] Frederick S. Billig. Design and development of single stage to orbit. *Johns Hopkins Apl Technical Digest*, 1990.

[15] Ernst Heinrich Hirschel et al. Basics of aerothermodynamics. 2005.

[16] Andrew J Butrica. Reusable launch vehicles or expendable launch vehicles? a perennial debate. *Critical Issues in the History of Spaceflight, edited by Dick S. and Launius R., NASA SP-4702*, 2006.

[17] NASA. Rockwell x-30, 2024. Accessed: 2024-07-04.

[18] Radian Aerospace. Radian One Spaceplane. `https://www.radianaerospace.com/radian-one`, Accesso continuo. Accessed: 2024-06-27.

[19] John David Anderson and Mary L Bowden. *Introduction to flight*, volume 582. McGraw-Hill Higher Education New York, NY, USA, 2005.

[20] Robert R. Barthelemy. The national aerospace plane program: A revolutionary concept. *fohns Hopkins APL Technical Digest*, 1990.

[21] Kerry D Hicks. *Introduction to astrodynamic reentry*. Air Force Institute of Technology, 2009.

[22] Geeta Arora, Varun Joshi, and Isa Sani Garki. Developments in runge–kutta method to solve ordinary differential equations. In *Recent Advances in Mathematics for Engineering*, pages 193–202. CRC Press, 2020.

[23] J Guadagnini, D Bonetti, G De Zaiacomo, et al. Entry corridor analysis for vertical landing reusable launch vehicles. In *26th Conference of the Italian Association of Aeronautics and Astronautics (AIDAA 2021)*, pages 1–5, 2021.

[24] John C Adams. Atmospheric re-entry. *Exoaviation, nd Web. http://exoaviation. webs. com/pdf_ files/AtmosphericRe-Entry. pdf*, 2003.

[25] Veronica Borriero. *Synthesis of reference guidance strategy based on re-entry corridor*. PhD thesis, Politecnico di Torino, 2018.

[26] Max L Blosser, Carl J Martin, Kamran Daryabeigi, and Carl C Poteet. Reusable metallic thermal protection systems development. 1998.

[27] Yunus A. Çengel. *Heat and mass transfer: Fundamentals and applications*. McGraw-Hill, 2002.

[28] Irene Huertas and Christian Möllmann. Re-entry vehicle design by multidisciplinary optimisation in astos. *4th International Conference on Astrodynamics Tools and Techniques*, 2010.

[29] Albert Walter Markl. An initial guess generator for launch and reentry vehicle trajectory optimization. Master's thesis, Institute of Flight Mechanics and Flight Control of the University of Stuttgart, 2001.

Acknowledgements

Un grazie particolare a Ciccio, che mi ha fatto comprendere il vero significato di "amicizia" e l'unico forse in grado di capirmi in assoluto. Anche se ci vediamo meno frequentemente sappiamo entrambi di poter contare l'uno sull'altro.

Grazie a tutti.

<div align="right">

Santi D.
Just Keep Living

</div>